Algorithm Theoretical Basis Document (ATBD) for the Conical-Scanning Microwave Imager/Sounder (CMIS) Environmental Data Records (EDRs)

Volume 14: Ocean EDR Algorithm Suite

Covering: Sea Surface Temperature EDR
Sea Surface Wind Speed/Direction EDR
Surface Wind Stress EDR

Version 2.0 – 15 March 2001

Solicitation No. F04701-01-R-0500

Written by:
Craig Smith
Frank Wentz
Thomas Meissner

Prepared for:
Boeing Satellite Systems
919 Imperial Highway
El Segundo, CA 90245

Submitted by:

Remote Sensing Systems

438 First Street, Suite 200, Santa Rosa, CA 95401   (707) 545-2904

ATBD for CMIS
Ocean EDR Algorithm Suite
Sea Surface Temperature EDR
Sea Surface Wind Speed/Direction EDR
Surface Wind Stress EDR

14-1

This page intentionally left blank.

ATBD for CMIS
Ocean EDR Algorithm Suite
Sea Surface Temperature EDR
Sea Surface Wind Speed/Direction EDR
Surface Wind Stress EDR

14-2

REVISION HISTORY

Version	Release Date	POC	Comments	Changes
1.0	01/10/2001	C. Smith T. Meissner F. Wentz	1st Partial Draft	
2.0	02/08/2001	C. Smith T. Meissner F. Wentz	2nd Partial Draft	• Added section 6.6: Concerns With Regards to Wind Vector Retrieval • Revised section 6.5: Performance of the Median Filter Algorithm • Included section 2.5.2: Historical and Background Perspective for Proposed CMIS Algorithms • Minor changes of Figures + Equations
3.0	02/21/2001	C. Smith T. Meissner F. Wentz	3rd Partial Draft	• Figures 5 + 6: curves for Yueh et al. 1999 corrected

RELATED CMIS DOCUMENTATION

Government Documents

Title	Version	Authorship	Date
CMIS SRD for NPOESS Spacecraft and Sensors	3.0	Associate Directorate for Acquisition, NPOESS IPO	2 March 2001

Boeing Satellite Systems Documents

Title		Covering
ATBD for the CMIS TDR/SDR Algorithms		
ATBD for the CMIS EDRs	Volume 1: Overview	Part 1: Integration
		Part 2: Spatial Data Processing • Footprint Matching and Interpolation • Gridding • Imagery EDR
	Volume 2: Core Physical Inversion Module	
	Volume 3: Water Vapor EDRs	Atmospheric Vertical Moisture Profile EDR Precipitable Water EDR
	Volume 4: Atmospheric Vertical Temperature Profile EDR	
	Volume 5: Precipitation Type and Rate EDR	
	Volume 6: Pressure Profile EDR	
	Volume 7: Cloud EDRs	Part 1: Cloud Ice Water Path EDR
		Part 2: Cloud Liquid Water EDR
		Part 3: Cloud Base Height EDR

ATBD for CMIS
Ocean EDR Algorithm Suite
Sea Surface Temperature EDR
Sea Surface Wind Speed/Direction EDR
Surface Wind Stress EDR

14-3

Title		Covering
	Volume 8: Total Water Content EDR	
	Volume 9: Soil Moisture EDR	
	Volume 10: Snow Cover/Depth EDR	
	Volume 11: Vegetation/Surface Type EDR	
	Volume 12: Ice EDRs	Sea Ice Age and Sea Ice Edge Motion EDR Fresh Water Ice EDR
	Volume 13: Surface Temperature EDRs	Land Surface Temperature EDR Ice Surface Temperature EDR
	Volume 14: Ocean EDR Algorithm Suite	Sea Surface Temperature EDR Sea Surface Wind Speed/Direction EDR Surface Wind Stress EDR
	Volume 15: Test and Validation	All EDRs

Bold = this document

ATBD for CMIS   14-4
Ocean EDR Algorithm Suite
Sea Surface Temperature EDR
Sea Surface Wind Speed/Direction EDR
Surface Wind Stress EDR

This document is intended for non-commercial use only. All other use is strictly forbidden without prior approval of the U.S. Government.

TABLE OF CONTENTS FOR VOLUME 14

ATBD for CMIS   14-5   This document is intended for non-commercial
Ocean EDR Algorithm Suite   use only. All other use is strictly forbidden without
Sea Surface Temperature EDR   prior approval of the U.S. Government.
Sea Surface Wind Speed/Direction EDR
Surface Wind Stress EDR

LIST OF FIGURES

ATBD for CMIS
Ocean EDR Algorithm Suite
Sea Surface Temperature EDR
Sea Surface Wind Speed/Direction EDR
Surface Wind Stress EDR

14-9

This document is intended for non-commercial use only. All other use is strictly forbidden without prior approval of the U.S. Government.

ATBD for CMIS   14-10   This document is intended for non-commercial
Ocean EDR Algorithm Suite   use only. All other use is strictly forbidden without
Sea Surface Temperature EDR   prior approval of the U.S. Government.
Sea Surface Wind Speed/Direction EDR
Surface Wind Stress EDR

LIST OF TABLES

ATBD for CMIS   14-11   This document is intended for non-commercial
Ocean EDR Algorithm Suite   use only. All other use is strictly forbidden without
Sea Surface Temperature EDR   prior approval of the U.S. Government.
Sea Surface Wind Speed/Direction EDR
Surface Wind Stress EDR

This page intentionally left blank.

ATBD for CMIS
14-12
Ocean EDR Algorithm Suite
Sea Surface Temperature EDR
Sea Surface Wind Speed/Direction EDR
Surface Wind Stress EDR

1. Abstract

The CMIS Ocean Algorithm Suite is used to retrieve sea surface temperature (SST), sea surface wind speed (W) and direction (WD) and wind stress (WS) environmental data records (EDRs). The SST and W EDR algorithms are pure statistical algorithms, while the wind vector algorithm is a hybrid statistical/physical algorithm. The latter finds wind direction solutions that best fit the CMIS measurements, using the reported SST EDR (for a circumscribing retrieval cell) and regressions for wind speed and atmospheric parameters to fill in all needed parameters in a model function for the brightness temperatures (TBs). The wind stress algorithm uses a bulk formulation for wind stress and the W EDR regression result.

The SST algorithm uses SDR derived TBs from all 6-36 GHz channels, averaged to a common 86 x 52 km resolution, to derive the SST within the skin depth for microwave measurements, which is approximately 1mm. The wind direction algorithm utilizes TBs from all 10-36 GHz channels, averaged to a 56 x 35 km resolution, to produce a set of wind vector ambiguities for each retrieval; in post processing, a median filter is used to select the ambiguity to be reported as the EDR. A byproduct of the wind vector retrieval is a wind speed at the same resolution ('low resolution' wind speed). This wind speed is reported with the wind direction solution to enable vector interpolation of the wind field to other grid systems by the user, if so desired.

The wind speed EDR algorithm utilizes TBs from all 18-36 GHz channels, averaged to a resolution of 25 x 20 km to retrieve a higher resolution wind speed. Both the low resolution wind speed and the wind speed EDR are neutral stability wind speeds and all wind parameters are reported at 10m height. The wind stress algorithm simply uses the reported wind speed EDR to interpolate the neutral stability coefficient of drag for 10m height from a lookup table and then applies a bulk formula to obtain wind stress.

In this ATBD we describe for each algorithm the physical basis, development, mathematical structure, required data, performance, and sensitivity to environmental effects and sensor control and knowledge errors. From the sensitivity analyses and EDR requirements, we derive requirements for the knowledge of the environmental parameters and sensor errors, and give example of how these are flowed to hardware requirements. Along the way, we also show performance for analogous algorithms we have developed for SSM/I and TMI.

When all sensor errors are at or within the derived requirements, all EDRs are expected to meet or exceed all EDR accuracy, precision and uncertainty SRD requirements in rain-free conditions, given the following:

1. (SST) The 6 GHz SST signature ($\partial T_B / \partial SST$) is approximately what we have derived from SMMR measurements—i.e. no significant slope decrease at low SST analogous to 10 GHz (see Figure 9).
2. (Wind direction) The wind direction signal is approximately what we have assumed (or larger) at low wind speeds.

ATBD for CMIS
Ocean EDR Algorithm Suite
Sea Surface Temperature EDR
Sea Surface Wind Speed/Direction EDR
Surface Wind Stress EDR

14-13

This document is intended for non-commercial use only. All other use is strictly forbidden without prior approval of the U.S. Government.

3. Angle between the look direction and the specular reflection of the sun from the observation area is more than 25 degrees for SST, and 15 degrees for the wind speed EDR and wind stress, and 25 degrees for the wind vector.
4. RFI is no larger than 0.1K over background in any of the TBs produced in the footprint compositing.

However, owing to the resolution of the 10 GHz channels for a 2m reflector (Table 2) the wind direction EDR may not meet the horizontal reporting cell size requirements. That is, the EDRs will meet the error requirements when compared to a larger reporting cell than specified in the Sensor Requirements Document (SRD). No such problem exists for the wind speed and wind stress EDRs.

All regression training, performance and sensitivity estimates are based on testing with high quality simulated brightness temperature data. Therefore, we include an extensive discussion of the development and mathematical form of the radiative transfer model (RTM) used to simulate the TB training and test data. The RTM discussion also supports the discussion of the physical basis of the algorithms, the retrieval model used in the wind direction algorithm, and the calibration and validation of the algorithms on-orbit.

A discussion of the TB datasets used to train the regression algorithms and test performance for all EDR algorithms is included, and is important for understanding the procedures for further algorithm development; the distributions of geophysical parameters are wide, flat, and uncorrelated for the training datasets, so that algorithms which perform well under diverse conditions can be derived, while the distributions for the test datasets follow the distributions found in nature to the extent possible, to give an accurate assessment of performance.

2. Overview and Background Information

2.1. Purpose

This Algorithm Theoretical Basis Document (ATBD) describes the information necessary to understand, operate, continue development of, and use the products of the CMIS retrieval algorithms for sea surface temperature, wind speed and direction, and wind stress. The CMIS Sensor Requirements Document (IPO 2000) specifies the operational and performance characteristics of the algorithms, including definitions, spatial resolution, measurement range and error metrics for the EDRs. The ocean algorithm suite is designed to meet these specific requirements in deriving the EDRs from CMIS measurements of the earth scene brightness temperatures. For wind direction only, where the EDR precision error requirement cannot be met at the required resolution, the satisfaction of the error metrics takes precedence over the resolution of the EDR product.

This section gives a short overview of the algorithm and radiative transfer model (RTM) development plan, and a historical perspective on ocean remote sensing, the heritage of our algorithms, and the performance of the analogous algorithms for SSM/I and TMI. We also describe the characteristics of the CMIS instrument that are important for specifying the performance of our algorithms.

In section 3, we present in detail the theoretical and empirical background of the CMIS RTM, which is used to generate simulated brightness temperature data to train and test algorithms, and which is used directly in the wind vector algorithm. This discussion includes the radiative transfer of microwave radiation through the Earth's atmosphere as well as the emission and reflection of polarized microwave radiation from the ocean surface.

Section 4 gives a discussion as well as a precise mathematical definition of each algorithm, and enumerates the data required for successful algorithm operation. It also includes algorithm and processing flow diagrams, the latter to elucidate the interdependencies among the algorithms.

Section 5 discusses the simulated data generated with the CMIS RTM, used for training the regressions algorithms and for testing all algorithms. The need for different distributions of the geophysical parameters for the training and test data is shown, and examples are given as to how the distributions affect the projected performance of the algorithms.

Section 6 details the performance for each algorithm found using the test data. When possible, the performances of analogous algorithms for TMI are included for comparison. Here we describe the end-to-end sensor model used in determining performance; we enumerate the sensor errors and their (derived requirements) values, describe the sensor error model, the SDR algorithm simulation, and the model for subtraction of TB biases found during the Calibration Validation (Cal/Val) period.

Section 7 contains with an outline for algorithm calibration and validation, including methodology, calibration of the CMIS observations to the RTM, and subsequent calibration of the RTM, as well as potential sources of ground truth data.

ATBD for CMIS
Ocean EDR Algorithm Suite
Sea Surface Temperature EDR
Sea Surface Wind Speed/Direction EDR
Surface Wind Stress EDR

2.2. Document Scope

The ocean algorithm suite ATBD covers algorithm operation beginning with the ingestion of 6-36 GHz earth scene TBs derived from the SDR algorithm. The TBs are assumed to have been composited to the appropriate resolution for each algorithm, and have had any overall bias with respect to the RTM (found during Cal/Val) subtracted from them. The SDR algorithm and the introductory discussion of the sensor error model and overall bias subtraction is contained in the ATBD for SDR processing. The remainder of the discussion regarding the end-to-end sensor model is discussed in section 6 of this ATBD.

This ATBD also provides plans, based on our previous SSM/I and TMI experience, for continued algorithm/RTM development and calibration/validation efforts both pre and post launch. These plans are intended to be revised, refined, and expanded in detail as the physics of the RTM is refined and new calibration sources become available. An outline and chronology of the plan is given in section 2.4, whereas the details of the methodology are left to section 7

2.3. Objectives of Algorithm Development

The objective of our CMIS work has been to develop SST, W, WD, and WS retrieval algorithms that meet or exceed the EDR requirements contained in the Systems Requirement Document (SRD), using the 6-36 GHz TBs measured by CMIS.

The RTM provides the relationship between the geophysical parameters SST, W, WD and WS and the Earth scene TBs to be measured by CMIS. (The surface wind stress is directly related to the surface wind speed and is not an independent parameter in the RTM.) The EDR algorithms address the inversion problem of finding SST, W, WD, WS given the CMIS TBs.

The CMIS RTM is a central component in this inversion process. All ocean EDR algorithms are developed using this RTM. That is, all regression training is performed using TB data simulated using the RTM, and the wind vector algorithm also uses the RTM explicitly. Improving the accuracy of the RTM, therefore, will improve the on-orbit performance of the retrieval algorithms. As a result, RTM development is an integral part of our algorithm development plan.

The importance of the RTM is underscored by the fact that the CMIS frequencies, polarizations, and earth incidence angles (EIAs) are not identical to those of preceding radiometers. Table 1 lists the channel selection and earth incidence angles for CMIS and other radiometers. Although some of the differences are small, they are significant enough to preclude the development of CMIS EDR algorithms using the existing radiometer measurements. However, the physics of the RTM should be reliable enough to interpolate the RTM to the EIAs and frequencies of CMIS. Also, while no radiometers on orbit have polarimetric channels in the 6-36 GHz range, the recent wind direction signal data from aircraft flights have been incorporated in the RTM allowing us to simulate TBs for the polarimetric channels.

Estimates of EDR performance and sensitivity to sensor errors contained in this document are also based on TB data simulated using the RTM. Here the same RTM is used to develop and test the algorithms, so small departures from realism here are not as crucial to the accuracy of the results. However, the desire to optimize the on-orbit EDR retrieval performance drives our effort to continually refine the RTM.

2.4. RTM and Algorithm Development Plan

Historically, our approach to RTM development has used existing radiometer measurements to calibrate various components of the RTM. The CMIS RTM has its origins in a physics based RTM that was calibrated using SSM/I and SMMR observations. This prototype RTM was able to reproduce the SSM/I TBs to an RMS accuracy of 0.6K (Table 3, in (Wentz 1997)). The next phase of development began when observations from the TRMM radiometer (TMI) became available. We are currently in the process of updating the surface wind and SST components of the RTM at 10.7 GHz using this data.

The radiative transfer model consists of two components: the first describes the transfer of microwave radiation through the Earth's atmosphere (atmospheric model), and the second describes the microwave emission and reflection from the ocean surface (surface model).

We have already developed a highly accurate atmospheric model for the frequency range between 1 and 100 GHz and earth incidence angles (EIA) between 50 and 60 deg. This theory is largely based on principles of atmospheric physics and electromagnetic radiation.

For the emission and reflection of polarized microwave radiation from the wind roughened ocean surface, only *phenomenological* models are available. By this we mean theoretical models with free parameters that must be supplied by experimental input. This input is obtained from collocated *in situ* measurements of the geophysical parameters (for instance by buoys) and radiometer measurements from aircraft or satellites. For the SSM/I and TMI frequencies below 37 GHz , it has been possible to obtain a very accurate relation between the measured TBs and T_S as well as W (Wentz and Meissner 1999).

We will continue our RTM development plan using measurements from radiometers to be launched in the near future. As soon as data from the two Advanced Microwave Scanning Radiometer (AMSR) become available, we will be able to perform a calibration of the RTM at 6.9 GHz. In particular the AMSR data will allow a precise determination of the dependence of the sea surface emissivity on SST, W, and WD for the non-polarimetric channels. Of particular importance is the WD dependence at 6 and 10 GHz, which governs how large a source of error wind direction variability will be in the SST retrievals.

To date, there has been a large uncertainty in the WD dependence for all polarizations and frequencies. This directional dependence originates from a wind-induced anisotropy in the sea surface roughness. Current models of the wind direction signal are based directly on measurements from satellites or aircraft radiometers, or on model calculations calibrated with radiometer data. Unfortunately, the models differ widely, especially at low and intermediate wind speeds (see Figure 5 through Figure 7). At the time the wind direction dependence was

ATBD for CMIS
Ocean EDR Algorithm Suite
Sea Surface Temperature EDR
Sea Surface Wind Speed/Direction EDR
Surface Wind Stress EDR

14-17

This document is intended for non-commercial use only. All other use is strictly forbidden without prior approval of the U.S. Government.

inserted into our CMIS RTM, only two models were available: (Wentz, 1992) for non-polarimetric channels and (Yueh, 1996) for polarimetric and non-polarimetric channels. Both models covered only 18 and 36 GHz, so scaling factors for the wind direction signal at 10 and 6 GHz had to be assumed. Initial results from our ongoing investigation using TMI data suggest that the wind direction signal the vertical and horizontal polarizations is smaller at low wind speeds than the previous models. However, the wind direction signal in the polarimetric channels remains very uncertain. Therefore, in addition to continuing our wind direction signal investigations using TMI and the two AMSRs, we intend to vigorously calibrate the surface component of the RTM for the polarimetric channels using WindSat observations.

As shown in Table 1, there are differences between the earth incidence angles for CMIS and the radiometers used or to be used in the calibration of the RTM. We do expect some degradation in the model accuracy as the earth incidence angles are changed. However, we expect the physics of the RTM to be reliable enough so that this degradation is minimal when we interpolate/extrapolate the RTM to the CMIS sensor configuration.

Given an accurate and reliable RTM, geophysical retrieval algorithms can be developed. Our approach to algorithm development is based on using the RTM to simulate TB data for a wide variety of ocean atmosphere scenes. These simulated data are used for training and testing the algorithms. We have tested this simulation methodology by using the prototype RTM to develop algorithms for SSM/I. When these algorithms were tested using actual SSM/I TB data, we found that they had essentially the same performance as algorithms developed directly from the SSM/I measurements. As the prototype RTM was calibrated to reproduce the SSM/I TBs, this exercise was a closure verification of the simulation methodology for developing retrieval algorithms.
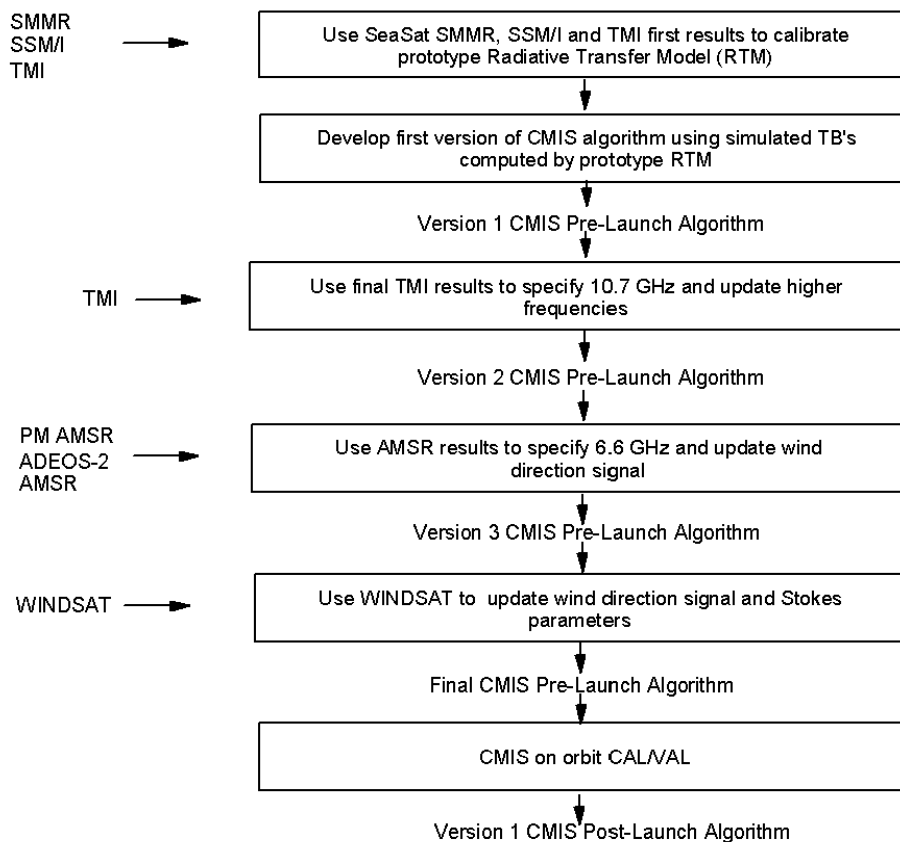
Figure 1: CMIS Algorithm/RTM Development Plan

Figure 1 summarizes our plan for algorithm and RTM development. We are entering the second phase of algorithm development, i.e. modifying the RTM to include final TMI results. The next step in this phase will be to retrain the regression algorithms and check the performance of all algorithms using TB data simulated with the revised RTM. These steps will be repeated for both AMSR radiometers and for WindSat to yield the pre-launch CMIS RTM and retrieval algorithms.

Once the CMIS instrument is launched, a final in flight calibration and validation (*CalVal*) will be performed. During Cal/Val, CMIS observations will be collocated with *in situ* (buoy, radiosonde) observations or measurements from other satellites (e.g. SSM/I, TMI, AMSR or the NASA scatterometer QUIKSCAT). One part of the collocated set will be used for calibrating the CMIS RTM and determining residual offsets between the measured TB's and those that are predicted by the RTM. (An outline of the calibration method is given in section 7.) The rest of the collocated data set will be used for validating the algorithm by comparing the observed with the retrieved geophysical parameters.

ATBD for CMIS
Ocean EDR Algorithm Suite
Sea Surface Temperature EDR
Sea Surface Wind Speed/Direction EDR
Surface Wind Stress EDR

14-19

Table 1: Channel configurations and nominal earth incidence angles (EIA) of current and future radiometer that are used for retrieving the geophysical parameters described in this document. Polarizations: V = vertical, H = horizontal, L/R = left/right handed circular, P/M = ±45 deg linear.

Radiometer	Frequencies/Polarization					Earth Incidence Angle (EIA)
SeaSat SMMR	6.6VH	10.7VH	18.0VH	21.0VH	37.0VH	49 deg
Nimbus-7 SMMR	6.6VH	10.7VH	18.0VH	21.0VH	37.0VH	51 deg
SSM/I			19.3VH	22.2V	37.0VH	53 deg
TRMM TMI		10.7VH	19.3VH	21.0VH	37.0VH	53 deg
PM AMSR	6.9VH	10.7VH	18.7VH	23.8VH	36.5VH	55 deg
ADEOS-2 AMSR	6.9VH	10.7VH	18.7VH	23.8VH	36.5VH	55 deg
WindSat	6.8VH	10.7VHPMLR	18.7 VHPMLR	23.8VH	37.0 VHPMLR	50 - 56 deg
CMIS	6.6VH	10.7VHLR	18.7VHLRPM	23.8VH	36.5VHPM	53 – 58 deg

2.5. Historical Perspective

2.5.1. Microwave Remote Sensing

In the 1960's, it was first recognized that microwave radiometers had the ability to measure atmospheric water vapor V and cloud liquid water L (Barrett and Chung 1962; Staelin 1966). In 1972, Nimbus-5 satellite was launched. Aboard Nimbus-5 was the Nimbus-E Microwave Spectrometer (NEMS), which had channels at 22.235 and 31.4 GHz. (Grody 1976; Staelin, Kunzi et al. 1976) demonstrated that water vapor and cloud water could indeed be retrieved from the NEMS T_B's. In these retrievals they ignored the effect of wind at the ocean surface; at these frequencies the effect of T_S is minimal.

In the years preceding the launch of Nimbus-5, there were several developments concerning the effect of wind at the ocean's surface. (Stogryn 1967) developed a theory to account for the wind-induced roughness, and (Hollinger 1971) made some radiometric measurements from a fixed tower to test the theory. He removed the most obvious foam effects from the data and found that the roughness effect was somewhat less than the Stogryn theory would predict by a frequency dependent factor. Using airborne data, (Nordberg, Conaway et al. 1971) characterized the combined foam and roughness effect at 19.35 GHz. At their measurement angle the observed effect was dominated by foam. Stogryn's geometric optics theory was extended to included diffraction effects, multiple scattering, and two-scale partitioning by (Wu and Fung 1972) and (Wentz 1975).

The first simultaneous retrieval of W, V, and L was based on airborne data from the 1973 joint US-USSR Bering Sea Experiment (BESEX) (Wilheit and Fowler 1977). Later (Chang and Wilheit 1979) combined two NIMBUS-5 instruments, the ESMR and the NEMS for a W, V, and L retrieval. (Wilheit 1979) used the 37-GHz dual polarized data from the Electrically Scanned Microwave Radiometer (ESMR) to explore the wind-induced roughness of the ocean surface. This was later combined with other data to generate a semi-empirical model for the ocean surface emissivity (Wilheit 1979) in preparation for the 1978 launch of the Scanning Multichannel Microwave Radiometer (SMMR) on the Nimbus-7 and SeaSat satellites. A theory for the retrieval of all four ocean parameters was published by (Wilheit and Chang 1980).

ATBD for CMIS
Ocean EDR Algorithm Suite
Sea Surface Temperature EDR
Sea Surface Wind Speed/Direction EDR
Surface Wind Stress EDR

14-20

The launch of the SeaSat and Nimbus-7 SMMRs spurred many investigations on SMMR retrieval algorithms and model functions (Alishouse 1983; Njoku and Swanson 1983; Wentz 1983; Chang, Hwang et al. 1984; Gloersen, Cavalieri et al. 1984), and the state-of-the-art in oceanic microwave radiometry quickly advanced. It became clear that the water vapor retrievals were highly accurate. A major improvement in the wind retrieval was made when (Wentz, Mattox et al. 1986) combined the SeaSat SMMR T_B's and the SeaSat scatterometer (SASS) wind retrievals to develop an accurate, semi-empirical relationship for the wind-induced emissivity.

Sea-surface temperature retrievals have been less successful. The measurement of T_S requires relatively low microwave frequencies (4-10 GHz). The SMMRs were the first satellite sensors with the appropriate frequencies to retrieve T_S. However, the SMMR's suffered from a poor calibration design, and the reported T_S retrievals (Njoku and Swanson 1983; Milman and Wilheit 1985) were useful for little more than a demonstration of the possibility of T_S retrievals for future, better calibrated radiometers.

The next major milestone was the launch of the Special Sensor Microwave Imager (SSM/I) in 1987. In contrast to SMMR, SSM/I has an external calibration system that provides stable observations. Unfortunately, the lowest SSM/I frequency is 19.3 GHz, and hence T_S retrievals are not possible. Shortly after the launch, there was a flurry of new SSM/I algorithms. Most of these algorithms, such as the (Goodberlet, Swift et al. 1989) wind algorithm and the (Alishouse, S. Synder et al. 1990) vapor algorithm, were simply statistical regressions to *in situ* data . These algorithms performed reasonably well but provided no information on the relevant physics. A more physical approach to algorithm development for SSM/I was taken by (Schluessel and Luthardt 1991) and (Wentz 1992; Wentz 1997). This physical approach to algorithm development is the basis for the CMIS ocean algorithm development, as described in the last section.

In November 1997, the first microwave radiometer capable of accurately measuring SST through clouds was launched on the Tropical Rainfall Measuring Mission (TRMM) spacecraft. The TRMM Microwave Imager (TMI) is providing an unprecedented view of the oceans. Its lowest frequency channel (10.7 GHz) penetrates non-raining clouds with little attenuation, giving a clear view of the sea surface under all weather conditions except rain. Furthermore at this frequency, atmospheric aerosols have no effect, making it possible to produce a very reliable SST time series for climate studies. The one disadvantage of the microwave SST is spatial resolution. The radiation wavelength at 10.7 GHz is about 3 cm, and at these long wavelengths the spatial resolution on the Earth surface for a single TMI observation is about 50 km. Also, the TRMM orbit was selected for continuous monitoring of the tropics. To achieve this, a low inclination angle was chosen, confining the TRMM observations between 40°S and 40°N. Previous microwave radiometers were either too poorly calibrated or operated at too high of a frequency to provide a reliable estimate of SST. The early results for our TMI SST retrievals are quite impressive, and are already leading to improved analyses in a number of important scientific areas, including tropical instability waves and tropical storms (Wentz, Gentemann et al. 2000).

2.5.2. Historical and Background Perspective for Proposed CMIS Algorithms

ATBD for CMIS   14-21   This document is intended for non-commercial
Ocean EDR Algorithm Suite   use only. All other use is strictly forbidden without
Sea Surface Temperature EDR   prior approval of the U.S. Government.
Sea Surface Wind Speed/Direction EDR
Surface Wind Stress EDR

Our SSM/I and TMI ocean algorithms have already demonstrated that the wind speed can be retrieved with high accuracy and precision. For SSM/I the overall wind speed accuracy and precision are 0.3 m/s and 1.0 m/s, respectively. For TMI the overall accuracy error is 0.05 m/s. The standard deviation is approximately 0.8 m/s for low resolution wind speeds, which are retrieved using the 10.7-37 GHz channels, and approximately 1.0 m/s for high resolution wind speeds, which are retrieved using the only 18.7-37 GHz channels. The addition of the polarimetric channels on CMIS is expected to reduce the precision errors further, due to the increase in signal/noise that results from using more observations. Figure 2 shows bias and standard deviation of TMI 10.7-37 GHz – BUOY wind speeds as a function of wind speed.
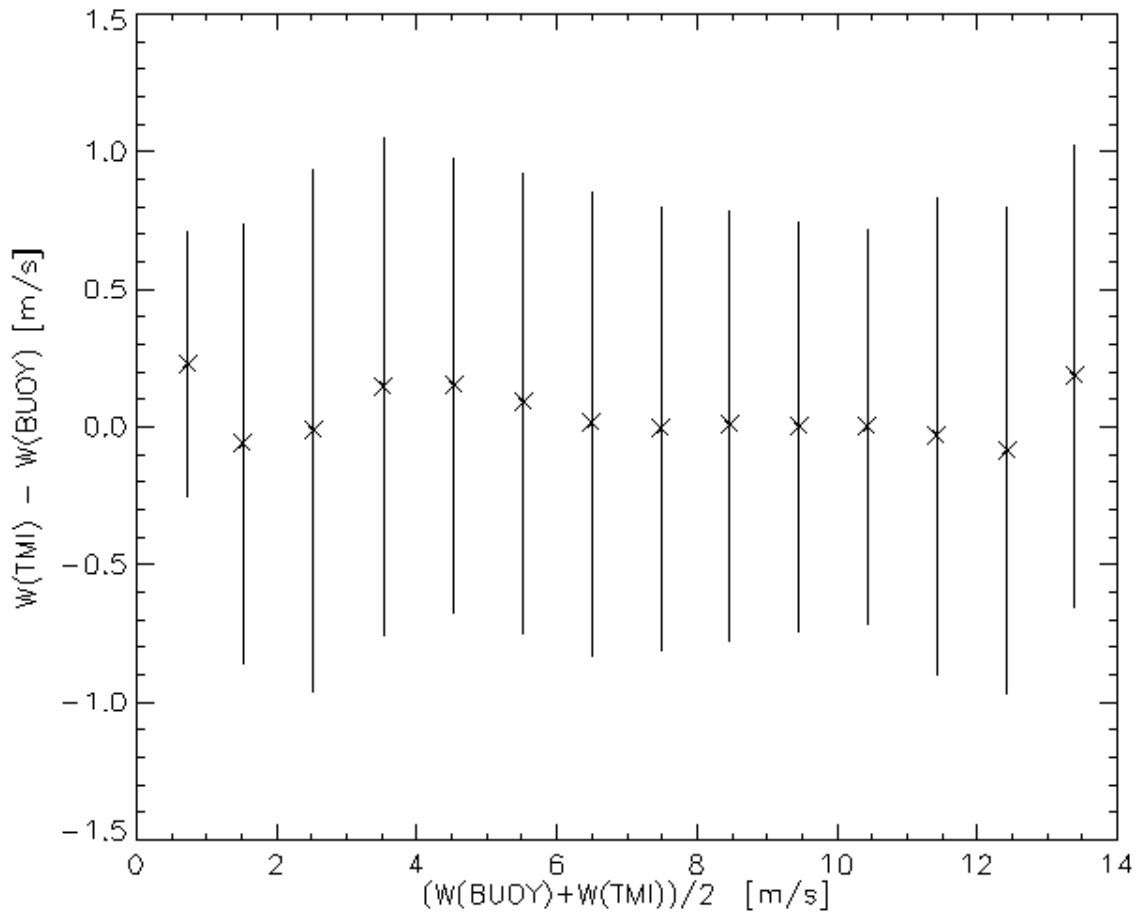
Figure 2: Bias and standard deviation of TMI 10.7-37 GHz wind speeds compared with buoys. Mean plus and minus one standard deviation for each 1 m/s wind speed bin.

Well-calibrated 10.7 GHz ocean observations from TMI show that T_S can be accurately retrieved in warm water above 15°C with an RMS error of 0.62 K. We expect better performance for AMSR and CMIS, because of the additional 7 GHz channel, which provides T_S sensitivity in both cold and warm water.

Accuracy and precision of the retrieved wind direction depend of course strongly on the strength of the wind direction signal in T_B and a final answer has to deferred until we are able to determine this signal more accurately from AMSR and WindSat observations.

ATBD for CMIS
Ocean EDR Algorithm Suite
Sea Surface Temperature EDR
Sea Surface Wind Speed/Direction EDR
Surface Wind Stress EDR

14-22

This document is intended for non-commercial use only. All other use is strictly forbidden without prior approval of the U.S. Government.

The SSM/I wind speed retrieval algorithm is a physical non-linear algorithm. The basic principle is to solve the equation

$$T_B = F(W,\ldots) \qquad (2.1)$$

where T_B is the brightness temperature measured by the satellite and F(…) is the physical model function of the RTM. The equation is solved iteratively for the EDR W using a Newton type method. In addition to W, also water vapor V and liquid cloud water L are retrieved in this way. In the context of the development of the CMIS ocean EDR algorithms, the SSM/I retrieval algorithms have been used for the development of the RTM. As mentioned in section 2.4, the CMIS Ocean EDR algorithms for SST and the 20 km W are a linear regression type algorithm. The regression coefficients are derived from Monte Carlo simulations based on a physical RTM with random instrument noise added. In general, regression algorithms are simpler and work faster than non-linear algorithm. Moreover, non-linear algorithms are not necessarily more exact than linear regression algorithms. In both cases, errors occur and the choosing one type algorithm over the other comes down to budgeting the tolerated error versus speed. The errors in the linear regression algorithms arise due to the error in linearizing the dependence between TBs and EDRs. In case of the non-linear algorithm, it is necessary to solve (2.1), which requires to make certain simplifications of the model function F(…). For example, the brightness temperature depends on the atmospheric density profiles for water vapor and liquid cloud water, whereas the F in (2.1) depends only on the columnar integrals V and L. These simplifications will, of course, lead to errors in the retrieved EDRs.
The TMI algorithms for retrieving SST and W both at high and low resolution are linear regressions. In view of their success also its successor, the AMSR algorithms will be linear regressions and we have decided that we will use linear regressions for SST and the 20 km wind speed at CMIS.

Much different is the situation for the wind vector retrieval. The dependence of the TB on the relative wind direction φ_r is a harmonic function over the interval [0, 360] deg, which cannot be linearized. Therefore, no linear regression algorithm can be used in this case. We have decided to apply a maximum likelihood estimate (MLE) that is based on minimizing the sum of squares (SOS)

$$\chi^2 = \sum_i \left[T_{B_i} - F_i(W, \varphi_r, A, T_S) \right]^2 \quad (2.2)$$

Here the sum $\sum_i$ runs over all channels between 10 and 36 GHz. We perform a 2 dimensional minimization with respect to W and φ_r , retrieving a wind vector at 56 x 35 km resolution. Those MLEs have been used in scatterometry for retrieving wind vectors for a long time: the SeaSat scatterometer (SASS) (Jones, Black et al. 1979; Wentz, Mattox et al. 1986), the NASA scatterometer NSCAT (Chi and Li 1988; Naderi, Freilich et al. 1991; Wentz 1997), the European Remote Sensing Satellites ERS (Stoffelen and Anderson 1995; Stoffelen 1998) and very recently also for the NASA scatterometer QUIKSCAT. In scatterometry, the MLE minimizes the SOS between the radar cross section that is backscattered from the ocean surface and an appropriate

ATBD for CMIS
Ocean EDR Algorithm Suite
Sea Surface Temperature EDR
Sea Surface Wind Speed/Direction EDR
Surface Wind Stress EDR

14-23

model function. The radar cross section is largely independent on the atmosphere and therefore the situation is much simpler than in radiometry, where the atmosphere contributes strongly to the signal. The A in (2.2) stands for all atmospheric parameters which have to be determined first at an intermediate step in order to calculate the SOS and perform the MLE. For all these atmospheric parameters we use linear regressions, as we do for the SST T_S . The whole wind vector retrieval algorithm for CMIS is therefore a combination between linear regression and non-linear SOS MLE. It is the first time that such a mixed type algorithm is used for wind vector retrieval in radiometry.

The MLE of the wind vector retrieval results in multiple solutions (ambiguities). The final step in the wind vector retrieval is to pass these ambiguities through a circular median filter (MF), which, in at least an ideal case, will select the ambiguity closest to the true wind vector. Median filtering is a well established technique in scatterometry and is or has been used for all the instruments mentioned above (Schultz 1990; Naderi, Freilich et al. 1991; Shaffer, Dunbar et al. 1991; Stoffelen and Anderson 1997). So far, it has never been applied in radiometry.

2.6. CMIS Instrument Characteristics

CMIS is a conically scanning microwave radiometer, intended for a sun-synchronous, near polar orbit with altitude between 816 and 850 km (nominal 833 km).   The instrument rotates continuously at 31.6 rpm about an axis parallel to the spacecraft nadir, taking measurements of the earth and intervening atmosphere along nearly semicircular arcs centered on the satellite ground track (the arcs would be circular except for the orbital motion of the satellite). The active scan is approximately 145 degrees, to accommodate a 1700 km swath width at all frequencies. The orbital velocity at the nominal altitude is such that the arcs for two successive scans are separated by 12.5 km in the along track direction.

CMIS has two separate reflectors for low (6-89 GHz) and high (166-183 GHz) frequencies. The algorithms contained in this document use only a portion (6-36 GHz) of the lower frequencies, and so our description will be confined to that which is relevant for these channels.

A 2.2m (2.06m aperture) offset parabolic reflector (the "main reflector") is used to collect the radiation and focus it onto the low frequency feed farm. The farm consists of 12 separate feedhorns in all, with one feedhorn (9 total) for each pair of orthogonal polarizations for each 6-36 GHz frequency. Each feed is the terminus of two total power radiometers, one for each polarization, fed by two orthogonal ortho-mode transducers (OMTs). For circular polarizations, a spiral staircase shaped polarizer in the feedhorn converts the radiation to linear polarizations accepted by the OMTs.

The basic characteristics of each lower frequency channel are included in Table 2 (throughout this document, we reference each channel by *truncating* the frequency to an integer). All the feeds for a given frequency share the same nadir angle so that the beam centers will be closely registered to one arc for a single scan. The feeds for different 6-36 GHz frequencies have three different nadir angles, so there are three separate arcs per scan. The nadir angle displacements are computed so that the along track separation between the three arcs equals a multiple of the 12.5 km separation, allowing the arcs of different frequencies to be coincident at the center of the scan (although the coincident arcs for the different frequencies are correspond to different scans).

Due to the different radii of scans at different nadir angles, there will be an increasing displacement between the arcs for different frequencies as one moves toward the edge of the scan.

Table 2: Characteristics of CMIS Channels.   Receiver ΔG/G and Quantization ΔT are 4.50E-5 and 0.12K, respectively, for all channels.

Feed	Center Frequency (GHz)	3 dB Bandwidth (B, MHz)	Nominal Nadir Angle (θ_n, deg)	Nominal EIA (θ_i, deg)	3dB EFOV Footprint (km)	Sampling Interval (ms)	Integration Time (τ, ms)	Noise Factor (NF, dB)	Video (ΔT, K)
6VH	6.625	350	47.0	55.79	67.7 x 39.3	5.06	5.00	1.99	0.10
10VH	10.65	100	48.7	58.16	45.5 x 24.8	2.53	2.47	1.85	0.10
10LR	10.65	100	48.7	58.16	45.5 x 24.8	2.53	2.47	2.05	0.10
18VH	18.70	200	45.4	53.62	23.5 x 15.5	1.265	1.20	2.83	0.14
18PM	18.70	200	45.4	53.62	23.5 x 15.5	1.265	1.20	2.83	0.14
18LR	18.70	200	45.4	53.62	23.5 x 15.5	1.265	1.20	3.33	0.14
23VH	23.80	400	45.4	53.62	24.4 x 15.7	1.265	1.20	3.59	0.14
37VH	36.50	1000	47.0	55.79	16.7 x 10.3	1.265	1.20	3.35	0.20
37PM	36.50	1000	47.0	55.79	16.7 x 10.3	1.265	1.20	3.35	0.20

The sample time, which is the time interval between the start of successive integrations, is set at 1.265 ms for the 18-36 GHz channels, twice that at 10 GHz, and four times that at 6 GHz. The along scan spacing between feeds and timing of the observations is set so that the beam centers for all 6-36 GHz observations are coregistered at the center of scan; then for each observation of a given frequency near the center of scan, there exist observations of all polarizations at that and all higher frequencies whose beam centers are coincident with the beam center of that observation. In total, the scan geometry and observation timing are optimized for the beam matching (footprint compositing) procedure, which is used to bring observations from different feeds to a common resolution and beam center.

The receiver subsystem accepts the RF noise power from the OMTs, and uses direct detection for the 6-36 GHz channels. The front end sections of the direct detection assembly are placed as close as physically possible to the OMTs to reduce front end losses and minimize Noise Equivalent ΔTs (NEDTs), and are connected to the OMTs by wave guides. The front end assembly for each channel amplifies the RF and filters the RF into a well defined bandpass, and consists of (in sequence) a low noise amplifier (LNA), a coaxial bandpass filter (BPF), a chain of amplifiers, and a final coaxial BPF. At 6 GHz, the wave guide connecting the OMT and LNA also serves as an initial BPF to eliminate a known emitter near 6.6 GHz. There are either 3 or 4 front end assemblies for each feed (i.e., orthogonal pair of channels) to provide redundancy and increase reliability.

The amplified RF signal from the front end assemblies is sent to the video unit, where it is square law detected, amplified, integrated over the required interval, and finally converted to a digital signal using a dedicated (one per front end) analog to digital converter. The gain of the video amplifiers is controllable. The digital signal that results becomes part of the Raw Data Record (RDR) to be transmitted to the ground along with the calibration, attitude and ephemeris data.

The parabolic reflector and feed farm are mounted on a triangular drum ("bucket") containing the radiometers, associated electronics, control subsystem and power subsystem. The drum is

ATBD for CMIS
Ocean EDR Algorithm Suite
Sea Surface Temperature EDR
Sea Surface Wind Speed/Direction EDR
Surface Wind Stress EDR

14-25

This document is intended for non-commercial use only. All other use is strictly forbidden without prior approval of the U.S. Government.

rotated about the nadir axis by a bearing and power transfer assembly (BAPTA). All data, commands, and power pass through slip ring connectors to the electronics in the drum. A cold space mirror and warm load are mounted on the BAPTA and do not rotate. The de-spun cold space mirror and warm load occult the main reflector once each rotation, allowing calibration data to be obtained for each channel for every scan. The number of usable observations of the calibration targets per scan varies from 4 at 6 GHz to 16 at 36 GHz, and is inversely proportional to the sample time.

2.7. Measurement Noise and Effective NEDTs

2.7.1. Single Observation NEDTs

The data from Table 2 can be used to compute the single observation NEDTs (not including calibration) for any observation using the equations

$$\Delta T = \sqrt{\Delta T_1^2 + \Delta T_{Video}^2 + \Delta T_{Quant}^2} \quad (2.3)$$

where

$$\Delta T_1 = T_{sys}\sqrt{\frac{1}{B\tau} + \left(\frac{\Delta G}{G}\right)^2} \quad (2.4)$$

and where the system temperature T_{sys} is defined by

$$T_{sys} = (f-1)T_{Amp} + T_A \quad (2.5)$$

and

$$f = 10^{\frac{NF}{10}} \quad (2.6)$$

In equation (2.5), the amplifier temperature is assumed to be 290K, and T_A is the antenna temperature of the observation. For the purpose of computing the typical single observation NEDT for each channel for each type of observation (Table 3), we use the cold space temperature (2.7K), the mean TB for each channel across the TB datasets for algorithm testing, and 300K as proxy for the antenna temperatures for the cold mirror, ocean, and hot load, respectively.

Table 3: Typical Single Observation NEDT for Ocean, Cold Mirror, and Warm Load Observations.

Channel	Mean Ocean TB (T_B, K)	Ocean NEDT (ΔT_o, K)	Cold Mirror NEDT (ΔT_c, K)	Hot Load NEDT (ΔT_h, K)
6V	173.2	0.302	0.203	0.388
6H	87.4	0.249	0.203	0.388

10V	186.4	0.703	0.352	0.927
10H	94.7	0.524	0.352	0.927
10L,R	140.6	0.654	0.390	0.969
18V	200.3	0.971	0.580	1.171
18H	138.1	0.846	0.580	1.171
18P,M	169.2	0.908	0.580	1.171
18L,R	169.2	1.044	0.712	1.308
23V	227.4	0.886	0.573	0.989
23H	184.3	0.825	0.573	0.989
36V	227.2	0.566	0.388	0.627
36H	171.7	0.520	0.388	0.627
36P,M	199.5	0.543	0.388	0.627

2.7.2. Footprint Compositing

2.7.2.1. Method and Noise Reduction Factors

Footprint compositing is the means by which observations of different frequencies are brought to a common resolution and beam center. The compositing routine, which is applied at the end of the SRD algorithm, is based on an optimal interpolation method, described in the ATBD for Footprint Matching and Interpolation (AER 2001). It uses observations from an area including and surrounding the target footprint to define the TBs for the composite cell as

$$T_{B,composite}(i_0, j_0) = \sum_{i=-N}^{N} \sum_{j=-M}^{M} c_{ij} T_B(i_0 + i, j_0 + j) \quad (2.7)$$

The coefficients c_{ij} define the footprint compositing. The NEDT of the composited observation is generally different than that for a single observation. If the composite size is larger than the size of an individual footprint, the noise in the composite is generally less. A noise reduction factor (NRF) that defines this decrease in the NEDT, assuming the noise in individual observations is uncorrelated, is found as

$$NRF = \sqrt{\sum_{i=-N}^{N} \sum_{j=-M}^{M} c_{ij}^2} \quad (2.8)$$

2.7.2.2. Why Composite Cells for Ocean EDR Retrieval are Ovals and Not Circles

Obviously, different sized composite cells lead to different coefficients c_{ij}, and therefore different NRFs. But, most importantly, for a given area enclosed by the composite (3dB) footprint, the shape of the composite strongly affects the NRFs.

Our experience with SSM/I, TMI, and now AMSR footprint compositing, has demonstrated that, for a given area enclosed by the composite footprint, the NRF is minimized when the composite has the same shape (height to width or *aspect* ratio) as the single observation footprint (EFOV). An example for the SST composite 6 GHz NRF, reproduced from the table on slide 5-

195 of the SFR presentation package, is shown in Table 4. Here the aspect ratio of the 6 GHz EFOV is about 1.63, and the height of the EFOV is on the order of 60 km. As the aspect ratio is increased from 1 to 1.64, the NRF drops by a factor of 63%, even though the area enclosed by the 3 dB composite has not changed. (Although not shown, the NRF begins to increase again when the aspect ratio is increased further.)

Table 4: Effect of Aspect Ratio of SST Composite Footprint on 6 GHz Noise Reduction Factor. (SFR era results-for example only)

Composite 3dB Dimensions (km)	Aspect Ratio	Area Enclosed (km^2)	NRF
50 x 50	1.00	1963	1.58
60 x 40	1.50	1884	0.76
64 x 39	1.64	1960	0.58

The SST and wind vector algorithms are very sensitive to the effective NEDTs at 6 and 10 GHz, respectively. Therefore to minimize the 6 and 10 GHz NRFs for the SST and wind vector retrievals, the composite cells are not circular, as for non-ocean algorithms, but instead are ovals with approximately the same aspect ratio as the individual observations. Stated another way, using composite cells with the same aspect ratio as the observations minimizes the composite area required to achieve a given NRF at 6 and 10 GHz. As the composite area required for retrieving SST and wind direction is larger than the area defined by the SRD Horizontal Cell Size requirement, this has the effect of minimizing the spatial error in the retrievals with respect to the horizontal cell.

The target composite footprint for the wind speed EDR is a circle. Here, the algorithm is less sensitive to compositing NRFs, so an elliptical composite is not necessary. However, due to the 18 and 23 GHz EFOVs being slightly longer than 20km cross-scan direction, the actual composite is slightly larger than 20km in this direction as well.

2.7.3. Effective NEDTs for the Composite Cell

We now turn to the problem of computing the effective NEDT and NRF for calibrated, composited ocean observations. Compositing occurs after the SDR algorithm, i.e., after the ocean observations have been calibrated against the warm load and cold mirror observations in the TDR algorithm. Let the measurement errors in a single observation of the ocean, cold mirror, and hot load be denoted ε_o, ε_c, ε_h. Multiple observations of the hot and cold load are obtained each scan (N_{cal} of them), and 8 scans of hot and cold load observations are averaged before using them in calibrating the ocean observation. Therefore, the effective NEDTs for the hot and cold loads are

$$\Delta T'_{c,h} = \frac{\Delta T_{c,h}}{\sqrt{8N_{cal}}} \quad (2.9)$$

ATBD for CMIS
Ocean EDR Algorithm Suite
Sea Surface Temperature EDR
Sea Surface Wind Speed/Direction EDR
Surface Wind Stress EDR

14-28

N_{cal} is 4 for 6 GHz, 8 for 10 GHz, and 16 for 18, 23, and 36 GHz. Let ε'_c and ε'_h denote the error in the 8-scan averaged measurements of the hot and cold load. Then to first order in the ε's, the result for calibrating an ocean observation is

$$T_{A,cal} = T_A + \varepsilon_o + \left[\varepsilon'_c + \frac{T_A - T_c}{T_h - T_c}(\varepsilon'_h - \varepsilon'_c)\right] \quad (2.10)$$

The term in brackets describes the error introduced by the TDR calibration: if the antenna temperature was equal to the cold space (hot load) temperature, the error introduced would be ε'_c (ε'_h); if the antenna temperature is in between, the error is found by linearly interpolating the error between that for the cold mirror and the warm load.

The difference between the ocean TA and the ocean TB that results from the SDR algorithm is few K, much smaller than TA or TB. So the T_A in the bracketed term in equation 8 can be approximated by T_B. Furthermore the effect of the SDR algorithm on the radiometer and calibration noise in the single ocean observation is minimal, so we can write

$$T_{B,cal} = T_B + \varepsilon_o + \left[\varepsilon'_c + \frac{T_B - T_c}{T_h - T_c}(\varepsilon'_h - \varepsilon'_c)\right](2.11)$$

Now we consider the effect of compositing the ocean TBs obtained from the SDR algorithm, which is represented below as angle brackets. If the number of observations used in the compositing is small enough that ε'_c and ε'_h are not changed significantly, then we obtain

$$\langle T_{B,cal} \rangle = \langle T_B \rangle + \langle \varepsilon_o \rangle + \left[\varepsilon'_c + \frac{\langle T_B \rangle - T_c}{T_h - T_c}(\varepsilon'_h - \varepsilon'_c)\right] \quad (2.12)$$

The effect of compositing is to reduce the noise the ocean TBs by a factor equal to the NRF. Assuming that the measurement errors in the ocean, cold mirror, and hot load observations are all uncorrelated, the error propagation formula derived from equation (2.12) reads (after expanding the term in brackets and substituting the mean TB for the composite value)

$$\Delta T^2_{B,cal,composite} = NRF^2 \Delta T^2_o + \left(\frac{\bar{T}_B - T_c}{T_h - T_c}\right)^2 \Delta T'^2_h + \left(1 - \frac{\bar{T}_B - T_c}{T_h - T_c}\right)^2 \Delta T'^2_c \quad (2.13).$$

Equation (2.13) slightly overestimates the effective NEDT for the composite cell when many scans are used in the compositing, because the running 8-scan average cold mirror and hot load tends to reduce the effective cold mirror and warm load NEDTs below the values found from equation (2.9).

We want to define an effective noise reduction factor such that, when multiplied by the single ocean observation NEDT, gives the effective NEDT of the calibrated, composited ocean observations:

$$\Delta T_{B,cal,composite} = NRF_{eff} \Delta T_o \ (2.14)$$

ATBD for CMIS
Ocean EDR Algorithm Suite
Sea Surface Temperature EDR
Sea Surface Wind Speed/Direction EDR
Surface Wind Stress EDR

14-29

By inspection, (2.13) gives

$$NRF_{eff} = \sqrt{NRF^2 + \left(\frac{\overline{T}_B - T_c}{T_h - T_c}\right)^2 \frac{\Delta T_h'^2}{\Delta T_o^2} + \left(1 - \frac{\overline{T}_B - T_c}{T_h - T_c}\right)^2 \frac{\Delta T_c'^2}{\Delta T_o^2}} \quad (2.15)$$

Since the departure of the effective NRF from the NRF is due to the calibration terms in (2.15), one can define an effective calibration amplification factor, CA_{eff}, as

$$NRF_{eff} = CA_{eff} * NRF \quad (2.16)$$

Once the NRFs for a given composite cell footprint size are computed, the typical effective NEDT for ocean observations can be computed using equations (2.9), (2.13), and the values from Table 3. The typical effective NRFs and CAs for each channel can then be computed through equations (2.14) and (2.16) and further use of Table 3. In Section 4 we compute the effective NRFs and CAs in this way. Using these effective NRFs allows a simplification in computing the effective NEDT in the sensor model used for assessing algorithm performance; the single observation ocean NEDT is computed on-the-fly from the actual simulated antenna temperature using equations (2.3) through (2.6) (i.e. it is different for each observation), and then equation (2.14) is used to define the effective NEDT for the composite of calibrated ocean observations (i.e., the inputs to the EDR algorithms). This simplifies the sensor model code and saves computation time over the alternatives of simulating the noise in the calibration and composite observations or using equation (2.13).

3. Geophysical Model for the Ocean and Atmosphere

3.1. Introduction

The key component of the EDR parameter retrieval algorithm is the geophysical model for the ocean and atmosphere. It is this model that relates the observed brightness temperature (T_B) to the relevant geophysical parameters. In remote sensing, the specification of the geophysical model is sometimes referred to as the forward problem in contrast to the inverse problem of inverting the model to retrieve EDR's. An accurate specification of the geophysical model is the crucial first step in developing the retrieval algorithm.

The RTM has been calibrated against SSM/I and TMI, and will shortly be calibrated against the two AMSRs and WindSat. In fact, it is a modification of the AMSR RTM that includes a proper treatment of the polarimetric brightness temperatures for +/-45 and circularly polarized radiation. As a test of the AMSR version of the RTM at 18-37 GHz, in 1998 we used training and test data simulated with the RTM to derive and assess performance of wind speed, columnar water vapor and cloud liquid water regression algorithms; the estimated performance was essentially the same as the actual performance with real SSM/I data.

3.2. Radiative Transfer Equation

We begin by deriving the radiative transfer model for the atmosphere bounded on the bottom by the Earth's surface and on the top by cold space. The derivation is greatly simplified by using the absorption-emission approximation in which radiative scattering from large rain drops and ice particles is not included. Over the spectral range from 6 to 37 GHz, the absorption-emission approximation is valid for clear and cloudy skies and for light rain up to about 0.5 mm/h.

In the microwave region, the radiative transfer equation is generally given in terms of the radiation brightness temperature (T_B), rather than radiation intensity. So we first give a brief discussion on the relationship between radiation intensity and T_B. Let P_λ denote the power within the wavelength range $d\lambda$, coming from a surface area dA, and propagating into the solid angle $d\Omega$. The specific intensity of radiation I_λ is then defined by

$$P_\lambda = I_\lambda \cos\theta_i \, d\lambda \, dA \, d\Omega \qquad (3.1)$$

The specific intensity is in units of erg/s-cm^3-steradian. The angle θ_i is the incidence angle defined as the angle between the surface normal and the propagation direction. For a black body, I_λ is given by Planck's law to be (Reif 1965)

$$I_\lambda = \frac{2hc^2}{\lambda^5 \left[\exp\left(hc/\lambda kT\right) - 1 \right]} \qquad (3.2)$$

where c is the speed of light (2.998×10^{10} cm/s), h is Planck's constant (6.626×10^{-27} erg-s), k is

Ocean EDR Algorithm Suite
Sea Surface Temperature EDR
Sea Surface Wind Speed/Direction EDR
Surface Wind Stress EDR

Boltzmann's constant (1.381×10^{-16} erg/K), λ (cm) is the radiation wavelength, and T (K) is the temperature of the black body. Consider a surface that is emitting radiation with a specific intensity I_λ. Then the brightness temperature T_B for this surface is defined as the temperature at which a black body would emit the radiation having specific intensity I_λ. In the microwave region, the exponent in (3.2) is small compared to unity, and (3.2) can be easily inverted to give T_B in terms of I_v.

$$T_B = \frac{\lambda^4 I_\lambda}{2kc} \tag{3.3}$$

This approximation is the well known Rayleigh-Jeans approximation for $\lambda \gg hc/kT$.

In terms of T_B, the differential equation governing the radiative transfer through the atmosphere is

$$\frac{\partial T_B}{\partial s} = -\alpha(s)\left[T_B(s) - T(s)\right] \tag{3.4}$$

where the variable s is the distance along some specified path through the atmosphere. The terms $\alpha(s)$ and $T(s)$ are the absorption coefficient and the atmospheric temperature at position s. Equation (3.4) is simply stating that the change in T_B is due to (1) the absorption of radiation arriving at s and (2) to emission of radiation emanating from s. We let s = 0 denote the Earth's surface, and let s = S denote the top of the atmosphere (i.e., the elevation above which $\alpha(s)$ is essentially zero).

Two boundary conditions that correspond to the Earth's surface at the bottom and cold space at the top are applied to equation (3.4). The surface boundary condition states that the upwelling brightness temperature at the surface $T_B\uparrow$ is the sum of the direct surface emission and the downwelling radiation that is scattered upward by the rough surface (Peake 1959).

$$T_{B\uparrow}(\mathbf{k_i}, 0) = E(\mathbf{k_i})T_S + \frac{\sec\theta_i}{4\pi} \int_0^{\pi/2} \sin\theta_s d\theta_s \int_0^{2\pi} d\varphi_s T_{B\downarrow}(\mathbf{k_s}, 0)\left[\sigma_{o,c}(\mathbf{k_s}, \mathbf{k_i}) + \sigma_{o,\times}(\mathbf{k_s}, \mathbf{k_i})\right] \tag{3.5}$$

where the first T_B argument denotes the propagation direction of the radiation and the second argument denotes the path length s. The unit propagation vectors $\mathbf{k_i}$ and $\mathbf{k_s}$ denote the direction of the upwelling and downwelling radiation, respectively. In terms of polar angles in a coordinate system having the z-axis normal to the Earth's surface, these propagation vectors are given by

$$\mathbf{k_i} = \left[\cos\varphi_i \sin\theta_i, \sin\varphi_i \sin\theta_i, \cos\theta_i\right] \tag{3.6}$$

$$\mathbf{k_s} = -\left[\cos\varphi_s \sin\theta_s, \sin\varphi_s \sin\theta_s, \cos\theta_s\right] \tag{3.7}$$

The first term in (3.5) is the emission from the surface, which is the product of the surface temperature T_S and the surface emissivity $E(\mathbf{k_i})$. The second term is the integral of downwelling radiation $T_{B\downarrow}(\mathbf{k_s})$ that is scattered in direction $\mathbf{k_i}$. The integral is over the 2π steradian of the

ATBD for CMIS
Ocean EDR Algorithm Suite
Sea Surface Temperature EDR
Sea Surface Wind Speed/Direction EDR
Surface Wind Stress EDR

14-32

This document is intended for non-commercial use only. All other use is strictly forbidden without prior approval of the U.S. Government.

upper hemisphere. The rough surface scattering is characterized by the bistatic normalized radar cross sections (NRCS) $\sigma_{o,c}(\theta_s,\theta_i)$ and $\sigma_{o,\times}(\theta_s,\theta_i)$. These cross sections specify what fraction of power coming from $\mathbf{k_s}$ is scattered into $\mathbf{k_i}$. The subscripts c and $\times$ denote co-polarization (i.e., incoming and outgoing polarization are the same) and cross-polarization (i.e., incoming and outgoing polarizations are orthogonal), respectively. The cross sections also determine the surface reflectivity $R(\mathbf{k_i})$ via the following integral.

$$R(\mathbf{k_i}) = \frac{\sec\theta_i}{4\pi} \int_0^{\pi/2} \sin\theta_s d\theta_s \int_0^{2\pi} d\varphi_s \left[\sigma_{o,c}(\mathbf{k_s},\mathbf{k_i}) + \sigma_{o,\times}(\mathbf{k_s},\mathbf{k_i}) \right] \tag{3.8}$$

The surface emissivity $E(\mathbf{k_i})$ is given by Kirchhoff's law to be

$$E(\mathbf{k_i}) = 1 - R(\mathbf{k}_i) \tag{3.9}$$

It is important to note that equations (3.5)and (3.8) provide the link between passive microwave radiometry and active microwave scatterometry. The scatterometer measures the radar backscatter coefficient, which is simply $\sigma_{o,c}(-\mathbf{k_i},\mathbf{k_i})$.

The upper boundary condition for cold space is

$$T_{B\downarrow}(\mathbf{k_s},S) = T_C \tag{3.10}$$

This simply states that the radiation coming from cold space is isotropic and has a magnitude of $T_C = 2.7$ K.

The differential equation (3.4) is readily solved by integrating and applying the two boundary conditions (3.5) and (3.10). The result for the brightness temperature at the top of the atmosphere (i.e., the value observed by Earth-orbiting satellites) is

$$T_{B\uparrow}(\mathbf{k_i},S) = T_{BU} + \tau \left[ET_S + T_{B\Omega} \right] \tag{3.11}$$

where T_{BU} is the contribution of the upwelling atmospheric emission, τ is the total transmittance from the surface to the top of the atmosphere, E is the Earth surface emissivity given by (3.9), and $T_{B\Omega}$ is the surface scattering integral in (3.5). The atmospheric terms can be expressed in terms of the transmittance function $\tau(s_1,s_2)$

$$\tau(s_1,s_2) = \exp\left(-\int_{s_1}^{s_2} ds\, \alpha(s) \right) \tag{3.12}$$

which is the transmittance between points s_1 and s_2 along the propagation path $\mathbf{k_s}$ or $\mathbf{k_i}$. The total transmittance τ in (3.11) is given by

$$\tau = \tau(0,S) \tag{3.13}$$

and the upwelling and downwelling atmosphere emissions are given by

$$T_{BU} = \int_0^S ds \, \alpha(s) \, T(s) \, \tau(s, S) \tag{3.14}$$

$$T_{BD} = \int_0^S ds \, \alpha(s) \, T(s) \, \tau(0, s) \tag{3.15}$$

The sky radiation scattering integral is

$$T_{B\Omega} = \frac{\sec \theta_i}{4\pi} \int_0^{\pi/2} \sin \theta_s d\theta_s \int_0^{2\pi} d\varphi_s (T_{BD} + \tau T_C) \left[\sigma_{o,c}(\mathbf{k_s}, \mathbf{k_i}) + \sigma_{o,\times}(\mathbf{k_s}, \mathbf{k_i}) \right] \tag{3.16}$$

Thus, given the temperature T(s) and absorption coefficient α at all points in the atmosphere and given the surface bistatic cross sections, T_B can be rigorously calculated. However, in practice, the 3-dimensional specification of T(s) and α over the entire volume of the atmosphere is not feasible, and to simplify the problem, the assumption of horizontal uniformity is made. That is to say, the absorption is assumed to only be a function of the altitude h above the Earth's surface, i.e., $\alpha(s) = \alpha(h)$. To change the integration variable from ds to dh, we note that for the spherical Earth

$$\frac{\partial s}{\partial h} = \frac{1 + \delta}{\sqrt{\cos^2 \theta + \delta(2 + \delta)}} \tag{3.17}$$

where θ is either θ_i or θ_s, $\delta = h/R_E$, and R_E is the radius of the Earth. In the troposphere $\delta \ll 1$, and an excellent approximation for $\theta < 60°$ is,

$$\frac{\partial s}{\partial h} = \sec \theta \tag{3.18}$$

With this approximation and the assumption of horizontal uniformity, the above equations reduce to the following expressions.

$$\tau(h_1, h_2, \theta) = \exp\left(-\sec \theta \int_{h_1}^{h_2} dh \, \alpha(h) \right) \tag{3.19}$$

$$\tau = \tau(0, H, \theta_i) \tag{3.20}$$

$$T_{BU} = \sec \theta_i \int_0^H dh \, \alpha(h) \, T(h) \, \tau(h, H, \theta_i) \tag{3.21}$$

$$T_{BD} = \sec \theta_s \int_0^H dh \, \alpha(h) \, T(h) \, \tau(0, h, \theta_s) \tag{3.22}$$

where $H = h(S)$. Thus, the brightness temperature computation now only requires the vertical profiles of T(h) and $\alpha(h)$ along with the surface cross sections. The following two sections discuss the atmospheric model for $\alpha(h)$ and the sea-surface model for the cross sections,

respectively. In closing, we note that the AMSR incidence angle is 55° and hence approximation (3.18) is quite valid, with one exception. In the scattering integral, θ_s goes out to 90°, and in this case we use (3.17) to evaluate the integral.

3.3. Model for the Atmosphere

In the microwave spectrum below 100 GHz, atmospheric absorption is due to three components: oxygen, water vapor, and liquid water in the form of clouds and rain (Waters 1976). The sum of these three components gives the total absorption coefficient (napers/cm).

$$\alpha(h) = \alpha_O(h) + \alpha_V(h) + \alpha_L(h) \tag{3.23}$$

Numerous investigators have studied the dependence of the oxygen and water vapor coefficients on frequency ν (GHz), temperature T (K), pressure P (mb), and water vapor density ρ_V (g/cm^3) (Becker and Autler 1946; Rosenkranz 1975; Waters 1976; Liebe 1985). To specify α_O and α_V as a function of (ν,T,P,ρ_V) we use the Liebe expressions with two modifications. In order to match the model brightness temperatures to SSM/I T_B measurements that have been collocated to radiosonde measurements of water vapor profiles we have reduced the self-broadening component of the water vapor continuum reduced by a factor of 0.52 and increased the width of the 22 GHz line by a factor of 1.015.

The liquid water coefficient α_L comes directly from the Rayleigh approximation to Mie scattering and is a function of T and the liquid water density ρ_L (g/cm^2). When the liquid water drop radius is small relative to the radiation wavelength, the absorption coefficient α_L (cm^{-1}) is given by the Rayleigh scattering approximation (Goldstein 1951):

$$\alpha_L = \frac{6\pi\rho_L(h)}{\lambda\rho_o} \text{Im}\left(\frac{1-\varepsilon}{2+\varepsilon}\right) \tag{3.24}$$

where λ is the radiation wavelength (cm), $\rho_L(h)$ is the density (g/cm^3) of cloud water in the atmosphere given as a function of h, ρ_o is the density of water ($\rho_o \approx 1$ g/cm^3), and ε is the complex dielectric constant of water. The specification of ε as a function of T and ν will be given in section 3.4. Note that the dielectric constant varies with temperature T(h) and hence is also a function of h.

Figure 3 shows the total atmospheric absorption for each component. Results for three water vapor cases (10, 30, and 60 mm) are shown. The cloud water content is 0.2 mm. This corresponds to a moderately heavy non-raining cloud layer.
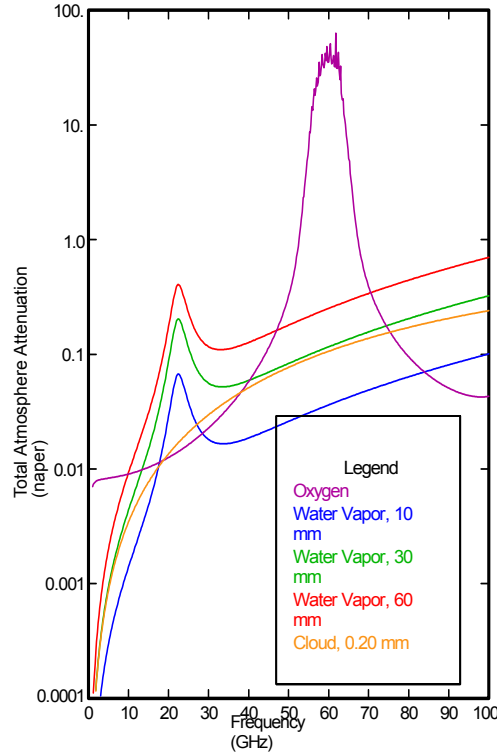
Figure 3: The atmospheric absorption spectrum for oxygen, water vapor, and cloud water. Results for three water vapor cases (10, 30, and 60 mm) are shown. The cloud water content is 0.2 mm, which corresponds to a moderately heavy non-raining cloud layer.

Let A_I denote the vertically integrated absorption coefficient.

$$A_I = \int_0^H dh \, \alpha_I(h) \tag{3.25}$$

where h is the height (cm) above the Earth's surface and subscript I equals O, V, or L. Equations (3.19) and (3.25) then give the total transmittance as

$$\tau = \exp\left[-\sec\theta_i \left(A_O + A_V + A_L\right)\right] \tag{3.26}$$

If we approximate the atmospheric temperature profile T(h) with a consrat effective temperature T_{eff} for the atmosphere – ocean system, then the integrals in equations (3.21) and (3.22) can be exactly evaluated in closed form to yield

$$T_{BU} = T_{BD} = \left(1 - \tau\right) T_{eff} \tag{3.27}$$

ATBD for CMIS
Ocean EDR Algorithm Suite
Sea Surface Temperature EDR
Sea Surface Wind Speed/Direction EDR
Surface Wind Stress EDR

14-36

In reality, the atmospheric temperature does vary with h, typically decreasing at a lapse rate of about -5.5 C/km in the lower to mid troposphere. In view of (3.27), we find it convenient to parameterize the atmospheric model in terms of the following upwelling and downwelling effective air temperatures:

$$T_U = T_{BU} /(1-\tau) \tag{3.28}$$

$$T_D = T_{BD} /(1-\tau) \tag{3.29}$$

These effective temperatures are indicative of the air temperature averaged over the lower to mid troposphere. Note that in the absence of significant rain, T_U and T_D are very similar in value, with T_U being 1 to 2 K colder.

3.4. Dielectric Constant of Sea-Water and the Specular Sea Surface

A key component of the sea-surface model is the dielectric constant ε of sea water. The parameter is a complex number that depends on frequency ν, water temperature T_S, and water salinity s. The dielectric constant is given by (Debye 1929; Cole and Cole 1941) as

$$\varepsilon = \varepsilon_\infty + \frac{\varepsilon_S - \varepsilon_\infty}{1+\left[j\lambda_R /\lambda \right]^{1-\eta}} - \frac{2j\sigma\lambda}{c} \tag{3.30}$$

where j = $\sqrt{-1}$, λ (cm) is the radiation wavelength, ε_∞ is the dielectric constant at infinite frequency, ε_S is the dielectric constant for zero frequency (i.e., the static dielectric constant), and λ_R (cm) is the relaxation wavelength. The spread factor η is an empirical parameter that describes the distribution of relaxation wavelengths.

The last term in (3.30) accounts for the conductivity of salt water. In this term, σ (sec^{-1}, Gaussian units) is the ionic conductivity and c is the speed of light.

Several investigators have developed models for the dielectric constant of sea water. In the (Stogryn 1971) model the salinity dependence of ε_S and λ_R was based on the (Lane and Saxton 1952) laboratory measurements of saline solutions. Stogryn noted that the Lane- Saxton measurements for distilled water did not agree with those of other investigators. The (Klein and Swift 1977) model is very similar to Stogryn model except that the salinity dependence of ε_S was based on more recent 1.4 GHz measurements (Ho and Hall 1973; Ho, Love et al. 1974). Klein-Swift noted that their ε_S was significantly different from that derived from the Lane and Saxton measurements. It appears that there may be a problem with Lane-Saxton measurements. However, in the Klein-Swift model, the salinity dependence of λ_R was still based on the Lane-Saxton measurements. We analyzed all the measurements used by Stogryn and Klein-Swift and concluded that the Lane-Saxton measurements of ε for both distilled water and salt water were inconsistent with the results reported by all other investigators. Therefore, we completely exclude the Lane-Saxton measurements from our model derivation.

The model to be presented is very similar to the Klein-Swift model, with two exceptions. First, since we excluded Lane-Saxton measurements, the salinity dependence of λ_R is different. For cold water ($0°C$ to $10°C$), our λ_R is about 5% lower than the Klein-Swift value and for warm water ($30°C$), it is about 1% higher. Second, our value for ε_∞ is 4.44 and the Klein-Swift value is 4.9, which was the value used by Stogryn. In the Stogryn model, $\eta = 0$, whereas in the Klein-Swift model, $\eta = 0.02$. (Grant, Buchanan et al. 1957) pointed out that the choice of ε_∞ depends on the choice for η, where $\eta = 0 \leftrightarrow \varepsilon_\infty = 4.9$ and $\eta = 0.02 \leftrightarrow \varepsilon_\infty = 4.5$. Thus the Klein-Swift value of $\varepsilon_\infty = 4.9$ is probably too high. In terms of brightness temperatures, these λ_R and ε_∞ differences are most significant at the higher frequencies. For example, at 37 GHz and $\theta_i = 55°$, the difference in specular brightness temperatures produced by our model and the Klein-Swift model differ by about ± 2 K. Analyses of SSM/I observations show that our new model, as compared to the Klein-Swift model, produces more consistent retrievals of ocean parameters. For example, using the Klein-Swift model resulted in an abundance of negative cloud water retrievals in cold water. This problem no longer occurs with the new model. (The negative cloud water problem was the original motivation for doing this reanalysis of the ε model.)

We first describe the dielectric constant model for distilled water, and then extend the model to the more general case of a saline solution. The static dielectric constant ε_{S0} for distilled water has been measured by many investigators. The more recent measurements (Malmberg and Maryott 1956; Archer and Wang 1990) are in very good agreement (0.2%). The (Malmberg and Maryott 1956; Archer and Wang 1990) values for ε_{S0}, which are reported in the *Handbook of Chemistry and Physics* (Lide 1993), are regressed to the following expression:

$$\varepsilon_{S0} = 87.90 \exp(-0.004585 \, t_S) \tag{3.31}$$

where $t_S = T_S - 273.16$ K is the water temperature in Celsius units. The accuracy of the regression relative to the point values for ε_{S0} is 0.01% over the range from $0°C$ to $40°C$.

The other three parameters for the dielectric constant of distilled water are the relaxation wavelength λ_{R0}, the spread factor η, and ε_∞. We determine these parameters by a least-squares fit of (3.30) to laboratory measurements ε_{mea} of the dielectric constant for the range from 1 to 40 GHz. A literature search yielded ten papers reporting ε_{mea} for distilled water. Values for λ_{R0}, η, and ε_∞ are found so as to minimize the following quantity:

$$Q = \left[\mathrm{Re}(\varepsilon - \varepsilon_{mea}) \right]^2 + \left[\mathrm{Im}(\varepsilon - \varepsilon_{mea}) \right]^2 \tag{3.32}$$

The relaxation wavelength is a function of temperature (Grant, Buchanan et al. 1957), but it is generally assumed that η and ε_∞ are independent of temperature. The least squares fit yields $\eta = 0.012$, $\varepsilon_\infty = 4.44$, and

$$\lambda_{R0} = 3.30 \, \exp(-0.0346 \, t_S + 0.00017 \, t_S^2) \tag{3.33}$$

These values are in good agreement with those obtained by other investigators. Our λ_{R0} agrees with the expression derived by (Stogryn 1971) to within 1%. The values for $\eta(\varepsilon_\infty)$

ATBD for CMIS
Ocean EDR Algorithm Suite
Sea Surface Temperature EDR
Sea Surface Wind Speed/Direction EDR
Surface Wind Stress EDR

14-38

reported in the literature vary from 0 to 0.02 (4 to 5). Note that using a larger value for η necessitates using a smaller value for ε_∞.

The presence of salt in the water produces ionic conductivity σ and modifies ε_S and λ_R. It is generally assumed that η and ε_∞ are not affected by salinity. (Weyl 1964) found the following regression for the conductivity of sea water.

$$\sigma = 3.39 \times 10^9 C^{0.892} \exp(-\Delta_t \zeta) \tag{3.34}$$

$$\zeta = 2.03 \times 10^{-2} + 1.27 \times 10^{-4} \Delta_t +$$
$$\quad 2.46 \times 10^{-6} \Delta_t^2 - C \left(3.34 \times 10^{-5} - 4.60 \times 10^{-7} \Delta_t + 4.60 \times 10^{-8} \Delta_t^2\right) \tag{3.35}$$

$$C = 0.5536 \; s \tag{3.36}$$

$$\Delta_t = 25 - t_S \tag{3.37}$$

where s and C are salinity and chlorinity in units of parts/thousand. Note that we have converted the Weyl conductivity to Gaussian units of $\sec^{-1}$.

To determine the effect of salinity on ε_S, we use low frequency (1.43 and 2.65 GHz) measurements of ε for sea water and saline solutions (Ho and Hall 1973; Ho, Love et al. 1974). For the Ho-Hall data, only the real part of the dielectric constant is used in the fit. Klein and Swift reported that the measurements of the imaginary part were in error. To determine the effect of salinity on λ_R, we use higher frequency (3 to 24 GHz) measurements of ε for saline solutions (Hasted and Sabeh 1953; Hasted and Roderick 1958). A least-squares fit to these data shows that the salinity dependence of ε_S and λ_R can be modeled as

$$\varepsilon_S = \varepsilon_{S0} \exp\left(-3.45 \times 10^{-3} s + 4.69 \times 10^{-6} s^2 + 1.36 \times 10^{-5} s t_S\right) \tag{3.38}$$

$$\lambda_R = \lambda_{R0} - 6.54 \times 10^{-3} \left(1 - 3.06 \times 10^{-2} t_S + 2.0 \times 10^{-4} t_S^2\right) s \tag{3.39}$$

The accuracy of the dielectric constant model is characterized in terms of its corresponding specular brightness temperature T_B. For each laboratory measurement of ε, we compute the specular T_B for an incidence angle of 55° using the Fresnel equations (3.40) and (3.41) below. Two T_B's are computed: one using ε_{mea} and the other using the model ε coming from the above equations. For the low frequency Ho-Hall data, the rms difference between the 'measurement' T_B and the 'model' T_B is about 0.1 K for v-pol and 0.2 K for h-pol. For the higher frequency data set, the rms difference is 0.8 K for v-pol and 0.5 K for h-pol.

Once the dielectric constant is known, the v-pol and h-pol reflectivity coefficients ρ_V and ρ_H for a specular (i.e., perfectly flat) sea surface are calculated from the well-known Fresnel equations

$$\rho_v = \frac{\varepsilon \cos\theta_i - \sqrt{\varepsilon - \sin^2\theta_i}}{\varepsilon \cos\theta_i + \sqrt{\varepsilon - \sin^2\theta_i}} \tag{3.40}$$

$$\rho_h = \frac{\cos\theta_i - \sqrt{\varepsilon - \sin^2\theta_i}}{\cos\theta_i + \sqrt{\varepsilon - \sin^2\theta_i}} \qquad (3.41)$$

where θ_i is the incidence angle. The power reflectivity R is then given by

$$R_{0p} = \left|\rho_p\right|^2 \qquad (3.42)$$

where subscript 0 denotes that this is the specular reflectivity and subscript p denotes polarization.

An analysis using TMI data indicates small deviations from the model function for the dielectric constant of sea water as discussed above. The effect is mainly noted in the v-pol reflectivity. In order to account for these small differences a correction term of

$$\Delta R_{0v} = 4.887 \cdot 10^{-8} - 6.108 \cdot 10^{-8} \cdot \left(T_S - 273\right)^3 \qquad (3.43)$$

is added to the v-pol reflectivity R_{0v} in (3.42). The resulting changes in the brightness temperature range from about +0.14K in cold water to about –0.36 K in warm water.

3.5. The Wind Roughened Sea Surface

It is well known that the microwave emission from the ocean depends on surface roughness. A calm sea surface is characterized by a highly polarized emission. When the surface becomes rough, the emission increases and becomes less polarized (except at incidence angles above 55º for which the vertically polarized emission decreases). There are three mechanisms that are responsible for this variation in the emissivity. First, surface waves with wavelengths that are long compared to the radiation wavelength mix the horizontal and vertical polarization states and change the local incidence angle. This phenomenon can be modeled as a collection of tilted facets, each acting as an independent specular surface (Stogryn 1967). The second mechanism is sea foam. This mixture of air and water increases the emissivity for both polarizations. Sea foam models have been developed by (Stogryn 1972) and (Smith 1988). The third roughness effect is the diffraction of microwaves by surface waves that are small compared to the radiation wavelength. (Rice 1951) provided the basic formulation for computing the scattering from a slightly rough surface. (Wu and Fung 1972) and (Wentz 1975) applied this scattering formulation to the problem of computing the emissivity of a wind-roughened sea surface. All of these three mechanisms depend both on wind speed and wind direction. In this section, we focus on the wind speed dependence. Wind direction dependence will be discussed in section 3.7.

The three effects can be parameterized in terms of the rms slope of the large-scale roughness, the fractional foam coverage, and the rms height of the small-scale waves. (Cox and Munk 1954; Monahan and O'Muircheartaigh 1980; Mitsuyasu and Honda 1982) derived wind speed relationships for the three parameters, respectively. These wind speed relationships in conjunction with the tilt + foam + diffraction model provide the means to compute the sea-

ATBD for CMIS
Ocean EDR Algorithm Suite
Sea Surface Temperature EDR
Sea Surface Wind Speed/Direction EDR
Surface Wind Stress EDR

14-40

This document is intended for non-commercial use only. All other use is strictly forbidden without prior approval of the U.S. Government.

surface emissivity. Computations of this type have been done by (Wentz 1975; Wentz 1983) and are in general agreement with microwave observations.

To model the rough sea surface, we begin by assuming the surface can be partitioned into foam-free areas and foam-covered areas within the radiometer footprint. The fraction of the total area that is covered by foam is denoted by f. The composite reflectivity is then given by

$$R = (1 - f)R_{clear} + f\kappa R_{clear} \qquad (3.44)$$

where R_{clear} is the reflectivity of the rough sea surface clear of foam, and the factor κ accounts for the way in which foam modifies the reflectivity. As discussed above, foam tends to decrease the reflectivity, and hence $\kappa < 1$. The reflectivity of the clear, rough sea surface is modeled by the following equation:

$$R_{clear} = (1 - \beta) \ R_{geo} \qquad (3.45)$$

where R_{geo} is the reflectivity given by the standard geometric optics model (see below) and the factor $1 - \beta$ accounts for the way in which diffraction modifies the geometric-optics reflectivity. (Wentz 1975) showed that the inclusion of diffraction effects is a relatively small effect and hence β small compared to unity.

Combining the above two equations gives

$$R = (1 - F)R_{geo} \qquad (3.46)$$
$$F = f + \beta - f\beta - f\kappa + f\kappa\beta \qquad (3.47)$$

where F is a 'catch-all' term that accounts for both foam and diffraction effects. All of the terms that makeup F are small compared to unity, and the results to be presented show that F < 10%. The reason we lump foam and diffraction effects together is that they both are difficult to model theoretically. Hence, rather than trying to compute F theoretically, we let F be a model parameter that is derived empirically from various radiometer experiments. However, the R_{geo} term is theoretically computed from the geometric optics. Thus, the F term is a measure of that portion of the wind-induced reflectivity that is not explained by the geometric optics.

The geometric optics model assumes the surface is represented by a collection of tilted facets, each acting as an independent reflector. The distribution of facets is statistically characterized in terms of the probability density function $P(S_u,S_c)$ for the slope of the facets, where S_u and S_c are the upwind and crosswind slopes respectively. Given this model, the reflectivity can be computed from equation (3.8). To do this, the integration variables θ_s,ϕ_s in (3.8) are transformed to the surface slope variables. The two equations governing this transformation are

$$\mathbf{k_s} = \mathbf{k_i} - 2(\mathbf{k_i} \cdot \mathbf{n})\mathbf{n} \qquad (3.48)$$

$$\mathbf{n} = \frac{[-S_u, -S_c, 1]}{\sqrt{1 + S_u^2 + S_c^2}} \qquad (3.49)$$

where **n** is the unit normal vector for a given facet. Transforming (3.8) to the S_u, S_c integration variables yields

$$R_{geo} = \frac{\int dS_u \int dS_c P(S_u, S_c) \sqrt{1 + S_u^2 + S_c^2} \, (\mathbf{k_i} \cdot \mathbf{n}) \left| (\mathbf{p} \cdot \mathbf{h_i}) \rho_h \mathbf{h_s} + (\mathbf{p} \cdot \mathbf{v_i}) \rho_v \mathbf{v_s} \right|^2 \left[\chi(\mathbf{k_s})(1 - R_\times) + R_\times \right]}{\int dS_u \int dS_c P(S_u, S_c) \sqrt{1 + S_u^2 + S_c^2} \, (\mathbf{k_i} \cdot \mathbf{n})}$$

(3.50)

where **p** is the unit vector specifying the reflectivity polarization. The unit vectors $\mathbf{h_i}$ and $\mathbf{v_i}$ ($\mathbf{h_s}$ and $\mathbf{v_s}$) are the horizontal and vertical polarization vectors associated with the propagation vector $\mathbf{k_i}$ ($\mathbf{k_s}$) as measured in the tilted facet reference frame. These polarization vectors in the tilted frame of reference are given by

$$\mathbf{h_j} = \frac{\mathbf{k_j} \times \mathbf{n}}{\left| \mathbf{k_j} \times \mathbf{n} \right|}$$

(3.51)

$$\mathbf{v_j} = \mathbf{k_j} \times \mathbf{h_j}$$

(3.52)

where subscript $j = i$ or s. The terms ρ_v and ρ_h are the v-pol and h-pol Fresnel reflection coefficients given above. The last factor in (3.50) accounts for multiple reflection (i.e., radiation reflecting off of one facet and then intersecting another). $\chi(\mathbf{k_s})$ is the shadowing function given by (Wentz 1975), and $R_\times$ is the reflectivity of the secondary intersection. The shadowing function $\chi(\mathbf{k_s})$ essentially equals unity except when $\mathbf{k_s}$ approaches surface grazing angles.

The interpretation of (3.50) is straightforward. The integration is over the ensemble of tilted facets having a slope probability of $P(S_u, S_c)$. The term $\sqrt{1 + S_u^2 + S_c^2} \, (\mathbf{k_i} \cdot \mathbf{n})$ is proportional to the solid angle subtended by the tilted facet as seen from the observation direction specified by $\mathbf{k_i}$. The term $\left| (\mathbf{p} \cdot \mathbf{h_i}) \rho_h \mathbf{h_s} + (\mathbf{p} \cdot \mathbf{v_i}) \rho_v \mathbf{v_s} \right|^2$ is the reflectivity of the tilted facet. And, the denominator in (3.50) properly normalizes the integral.

To specify the slope probability we use a Gaussian distribution as suggested by (Cox and Munk 1954), and we assume that the upwind and crosswind slope variances are the same. Wind direction effects are considered in section 3.7. Then, the slope probability is given by

$$P(S_u, S_c) = \left(\pi \Delta S^2 \right)^{-1} \exp \left[\frac{-S_u^2 - S_c^2}{\Delta S^2} \right]$$

(3.53)

where ΔS^2 is the total slope variance defined as the sum of the upwind and crosswind slope variances. Ocean waves with wavelengths shorter than the radiation wavelength do not contribute to the tilting of facets and hence should not be included in the ensemble specified by $P(S_u, S_c)$. For this reason, the effective slope variance ΔS^2 increases with frequency, reaching a maximum value referred to as the optical limit. The results of (Wilheit and Chang 1980) and (Wentz 1983) indicate that the optical limit is reached near $\nu = 37$ GHz. Hence, for $\nu \geq 37$ GHz, we use the (Cox and Munk 1954) expression for optical slope variance. For lower frequencies, a

ATBD for CMIS
Ocean EDR Algorithm Suite
Sea Surface Temperature EDR
Sea Surface Wind Speed/Direction EDR
Surface Wind Stress EDR

14-42

This document is intended for non-commercial use only. All other use is strictly forbidden without prior approval of the U.S. Government.

reduction factor is applied to the Cox and Munk expression. This reduction factor is based on ΔS^2 values derived from the SeaSat SMMR observations (Wentz 1983).

$$\Delta S^2 = 5.22 \times 10^{-3} W \qquad\qquad\qquad \nu \geq 37 \text{ GHz} \qquad\qquad (3.54)$$

$$\Delta S^2 = 5.22 \times 10^{-3} \left[1 - 0.00748(37 - \nu)^{1.3} \right] W \qquad \nu < 37 \text{ GHz} \qquad (3.55)$$

where W is the wind speed (m/s) measured 10 m above the surface. Note the Cox and Munk wind speed was measured at a 12.5 m elevation. Hence, their coefficient of 5.12×10^{-3} is increased by 2% to account for our wind being referenced to a 10 m elevation.

Table 5: Model Coefficients for Geometric Optics. r_0 in units of s/m, r_1 in units of s/m-deg, r_2 in units of s/m-K, r_3 in units of s/m-deg-K.

Freq. (GHz)	6.625	10.65	18.70	23.80	36.50
v-pol r_0	−0.27E−03	−0.32E−03	−0.49E−03	−0.63E−03	−1.01E−03
h-pol r_0	0.54E−03	0.72E−03	1.13E−03	1.39E−03	1.91E−03
v-pol r_1	−0.21E−04	−0.29E−04	−0.53E−04	−0.70E−04	−1.05E−04
h-pol r_1	0.32E−04	0.44E−04	0.70E−04	0.85E−04	1.12E−04
v-pol r_2	0.01E−05	0.11E−05	0.48E−05	0.75E−05	1.27E−05
h-pol r_2	0.00E−05	−0.03E−05	−0.15E−05	−0.23E−05	−0.36E−05
v-pol r_3	0.00E−06	0.08E−06	0.31E−06	0.41E−06	0.45E−06
h-pol r_3	0.00E−06	−0.02E−06	−0.12E−06	−0.20E−06	−0.36E−06

The sea-surface reflectivity R_{geo} is computed for a range of winds varying from 0 to 20 m/s, for a range of sea-surface temperatures varying from 273 to 303 K, and for a range of incidence angles varying from 49 deg to 57 deg. These computations require the numerical evaluation of the integral in equation (3.50). The integration is done over the range $S_u^2 + S_c^2 \leq 4.5\Delta S^2$. Facets with slopes exceeding this range contribute little to the integral, and it is not clear if a Gaussian slope distribution is even applicable for such large slopes. Analysis shows that the computed ensemble of R_{geo} is well approximated by the following regression:

$$R_{geo} = R_0 - \left[r_0 + r_1(\theta_i - 53) + r_2(T_S - 288) + r_3(\theta_i - 53)(T_S - 288) \right] W \qquad (3.56)$$

where the first term R_0 is the specular power reflectivity given by (3.42) and the second term is the wind-induced component of the sea-surface reflectivity. The r coefficients are given in Table 5 for all relevant CMIS channels. Equation (3.56) is valid over the incidence angle from 49 deg to 57 deg. It approximates the θ_i and T_S variation of R_{geo} with an equivalent accuracy of 0.1 K. The approximation error in the wind dependence is larger. In the geometric optics computations, the variation of R_{geo} with wind is not exactly linear. In terms of T_B, the non-linear component of R_{geo} is about 0.1 K at the lower frequencies and 0.5 K at the higher frequencies. However, in view of the general uncertainty in the geometric optics model, we will use the simple linear expression for R_{geo}, and let the empirical F term account for any residual non-linear wind variations, as is discussed in the next paragraph.

ATBD for CMIS
Ocean EDR Algorithm Suite
Sea Surface Temperature EDR
Sea Surface Wind Speed/Direction EDR
Surface Wind Stress EDR

14-43

In the 19-37 GHz band, the F term is found from collocated SSM/I-buoy observations. The procedure for finding F is essentially the same as described by (Wentz 1997) for finding the wind-induced emissivity, but in this case we first remove the geometric optics contribution to R. The F term is found to be a monotonic function of wind speed described by

$$F = m_1 W \qquad\qquad\qquad\qquad\qquad\qquad W < W_1 \qquad\qquad\qquad (3.57)$$
$$F = m_1 W + \tfrac{1}{2}(m_2 - m_1)(W - W_1)^2 / (W_2 - W_1) \qquad W_1 \leq W \leq W_2 \qquad (3.58)$$
$$F = m_2 W - \tfrac{1}{2}(m_2 - m_1)(W_2 + W_1) \qquad\qquad W > W_2 \qquad\qquad (3.59)$$

This equation represents two linear segments connected by a quadratic spline such that the function and its first derivative are continuous. The spline points W_1 and W_2 are 7 and 12 m/s, respectively. The m coefficients are found so that the T_B model matches the SSM/I observations when the buoy wind is used to specify W. Over the SSM/I range for frequencies from 19 to 37 GHz, we find that m_1 and m_2 are independent of both frequency and polarization. We find that $m_1 = 0.00254$ s/m and $m_2 = 0.00915$ s/m for $\nu \geq 19$ GHz.

At the two lowest CMIS frequency of 6.625 GHz and 10.7 GHz, there are no SSM/I data. Collocated SMMR-SASS observations suggest that the values for m_1 and m_2 at 10.7GHz (6.625 GHz) are about 82% (60%) of their values at 19 GHz. The following expressions model the observed behavior

$$m_1 = 2.89 \times 10^{-4} \nu - 9.28 \times 10^{-6} \nu^2 + 5.83 \times 10^{-8} \nu^3 \qquad \nu \leq 19 \text{ GHz} \qquad (3.60)$$
$$m_2 = 8.42 \times 10^{-4} \nu - 1.26 \times 10^{-5} \nu^2 - 3.35 \times 10^{-7} \nu^3 \qquad \nu \leq 19 \text{ GHz} \qquad (3.61)$$

where ν is frequency (GHz). These expressions monotonically increase with ν up to 19 GHz, at which $m_1 = 0.00254$ s/m and $m_2 = 0.00915$ s/m and $\partial m / \partial \nu = 0$. For $\nu > 19$ GHz, m_1 and m_2 are held at their 19-GHz value. The m_1 and m_2 are found to be independent of polarization.

These results indicate that diffraction plays a significant role in modifying the sea-surface reflectivity. If diffraction was not important, β would be 0 in equation (3.47), and F would be proportional to the fractional foam coverage f. Since f is essentially zero for W < 7 m/s, m_1 would be 0. This is not the case, and we interpret the m_1 coefficient as an indicator of diffraction.

We want to stress that all the expressions for the various components of the reflectivity R, such as the F-term (3.57)-(3.59) and the form of the m coefficients (3.60) and (3.61), will be updated as result of the Cal/Val for TMI, AMSR, WindSat and CMIS (chapter 0). This will provide values for R for all relevant frequencies, wind speeds, SST's and EIA's.

3.6. Atmospheric Radiation Scattered by the Sea Surface

The downwelling atmospheric radiation incident on the rough sea surface is scattered in all directions. The scattering process is governed by the radar cross section coefficients σ_o as

indicated by equation (3.16). For a perfectly flat sea surface, the scattering process reduces to simple specular reflection, for which radiation coming from the zenith angle θ_s is reflected into zenith angle θ_i, where $\theta_s = \theta_i$. In this case, the reflected sky radiation is simply RT_{BD}. However, for a rough sea surface, the tilted surface facets reflect radiation for other parts of the sky into the direction of zenith angle θ_i. Because the downwelling radiation T_{BD} increases as the secant of the zenith angle, the total radiation scattered from the sea surface is greater than that given by simple specular reflection. The sea-surface reflectivity model discussed in the previous section is used to compute the scattered sky radiation $T_{B\Omega}$. These computations show that $T_{B\Omega}$ can be approximated by

$$T_{B\Omega} = [(1+\Omega)(1-\tau)(T_D - T_C) + T_C]\, R \quad (3.62)$$

where R is the sea-surface reflectivity given by (3.46), T_D is the effective downwelling brightness temperature from zenith angle θ_i given by (3.29), and Ω is the fit parameter. The second term in the brackets is the isotropic component of the cold space radiation. This constant factor can be removed from the integral. The fit parameter for v-pol and h-pol is found to be

$$\Omega_V = [2.5 + 0.018(37 - \nu)\,][\Delta S^2 - 70.0\Delta S^6]\, \tau^{3.4} \quad (3.63)$$
$$\Omega_H = [6.2 - 0.001(37 - \nu)^2][\Delta S^2 - 70.0\Delta S^6]\, \tau^{2.0} \quad (3.64)$$

where ν is frequency (GHz) and ΔS^2 is the effective slope variance given by (3.54) and (3.55). The term $\Delta S^2 - 70.0\Delta S^6$ reaches a maximum at $\Delta S^2 = 0.069$. For $\Delta S^2 > 0.069$, the term is held at its maximum value of 0.046. Ω_V has a linear dependence on frequency, whereas Ω_H has a quadratic dependence, reaching a maximum value at $\nu = 37$ GHz. For $\nu > 37$ GHz, Ω_H is held constant at this maximum value. Approximation (3.63) and (3.64) is valid for the range of incidence angles from 52 deg to 56 deg. For moderately high winds (12 m/s) and a moist atmosphere (high vapor and/or heavy clouds), the scattering process increases the reflected 37 GHz radiation by about 1 K for v-pol and 5 K for h-pol. At 7 GHz, the increase is much less, being about 0.2 K for v-pol and 0.8 K for h-pol. The accuracy of the above approximation as compared to the theoretical computation is about 0.03 K and 0.2 K at 7 and 37 GHz, respectively. Note that when the atmospheric absorption becomes very large (i.e., τ is small), Ω tends to zero because the sky radiation for a completely opaque atmosphere is isotropic. (See also EN # 62 response.)

Similar to the reflectivity R, we will provide revised values for Ω during Cal/Val, which will be valid over the whole relevant ranges of frequency, SST, wind speed, EIA and atmospheric conditions.

3.7. The Wind Direction Signal

3.7.1. Introduction

In scatterometry, the anisotropy of capillary waves is responsible for the observed dependence of radar backscattering on wind direction (Jones, Black et al. 1979). The upwind radar return is considerably higher than the crosswind return. In addition, the modulation of the capillary waves by the underlying gravity waves causes the upwind return to be generally higher

ATBD for CMIS
Ocean EDR Algorithm Suite
Sea Surface Temperature EDR
Sea Surface Wind Speed/Direction EDR
Surface Wind Stress EDR

14-45

This document is intended for non-commercial use only. All other use is strictly forbidden without prior approval of the U.S. Government.

than the downwind return. These directional characteristics of the radar return have provided the means to sense wind direction from aircraft and satellite scatterometers (Jones, Black et al. 1979). The emission, which is radiated form the ocean surface, shows also a dependence on wind direction. Let us start by discussing the effects that are responsible for this.

The probability density function of the sea-surface slope is skewed in the alongwind axis and has a larger alongwind variance than crosswind variance (Cox and Munk 1954). The rms height of capillary waves is very anisotropic (Mitsuyasu and Honda 1982). The capillary waves traveling in the along-wind direction have a greater amplitude than those traveling in the crosswind direction. Another type of directional dependence occurs because the foam and capillary waves are not uniformly distributed over the underlying structure of large-scale waves. The aircraft radiometer measurements by (Smith 1988) show that the forward plunging side of a breaking wave exhibits distinctly warmer microwave emissions than does the back side. In addition, the capillary waves tend to cluster on the downwind side of the larger gravity waves (Cox 1958; Keller and Wright 1975). The dependence of foam and capillary waves on the underlying structure produces an upwind-downwind asymmetry in the sea-surface emissivity.

Both the upwind-crosswind asymmetries and the up-downwind asymmetries cause the measured brightness temperatures to depend on the relative wind direction $\varphi_r = \varphi_W - \varphi_i$. The φ_W is the wind direction and φ_i is the radiometer look azimuth, both measured relative to geographic North.

3.7.2. Stokes Parameters

The polarization state of thermal emission from an anisotropic medium or a medium with geometric directional features is completely determined by four Stokes parameters (Jackson 1975). The modified Stokes-4-vector can be represented in terms of TB's as:

$$\mathbf{T_B} = \begin{pmatrix} T_V \\ T_H \\ T_3 \\ T_4 \end{pmatrix} = \begin{pmatrix} T_V \\ T_H \\ T_P - T_M \\ T_L - T_R \end{pmatrix} \quad (3.65)$$

The notation for the polarizations is as follows:
- V: vertical polarization
- H: horizontal polarization
- P: +45 deg polarization
- M: -45 deg polarization
- L: left handed circular polarization
- R: right handed circular polarization

The components of the Stokes vector are functions of φ_r and must be periodic in 360 deg. Therefore they can be expressed as harmonic functions of φ_r. From reflection symmetry of the Maxwell equations it follows that T_V and T_H are even and T_3 and T_4 are odd functions of

φ_r (Yueh, Nghiem et al. 1994). Therefore the harmonic expansions of the components of (3.65) in terms of φ_r read:

$$T_V = T_{V0} + T_{V1}\cos(\varphi_r) + T_{V2}\cos(2\varphi_r)$$
$$T_H = T_{H0} + T_{H1}\cos(\varphi_r) + T_{H2}\cos(2\varphi_r)$$
$$T_3 = T_{31}\sin(\varphi_r) + T_{32}\sin(2\varphi_r) \qquad (3.66)$$
$$T_4 = T_{41}\sin(\varphi_r) + T_{42}\sin(2\varphi_r)$$

3.7.3. Separation of the Directional Signal

The isotropic (direction independent) part of the Stokes vector is T_{V0} and T_{H0}, which correspond to the V-pol and H-pol T_B's that can be computed using the RTM presented up to this point. We define $\Delta\mathbf{T_B} = \mathbf{T_B} - \mathbf{T_{B0}}$ as the wind direction signal. Analogously, we can define the emissivity directional signal $\Delta\mathbf{E}$ and the reflectivity directional signal $\Delta\mathbf{R}$.

For the approximation of a constant, effective temperature profile of the Atmosphere – Ocean scene $T(h) = T_S \equiv T_{eff} = const$ we can apply (3.27) (see EN #96 response). Furthermore let us neglect the small cold space temperature T_C as well as the small scatter term Ω in (3.62). This means we assume that $T_{B\Omega} \approx RT_{BD}$. Substituting this into (3.11) we find:

$$\mathbf{T_B} \approx \left(\mathbf{1} - \mathbf{R}\tau^2\right)T_{eff} \qquad (3.67)$$

and for the directional signal:

$$\Delta\mathbf{E} = -\Delta\mathbf{R} \approx \frac{\Delta\mathbf{T_B}}{\tau^2 T_{eff}} \qquad (3.68).$$

Equation (3.68) means that all directional dependence is effectively contained in $\mathbf{R} = \mathbf{1} - \mathbf{E}$ and the scattering coefficient Ω from section 3.6 is isotropic, i.e. $\Delta\Omega = 0$. This provides the means to determine the emissivity signal $\Delta\mathbf{E}$ from aircraft and satellite observations, as we will discuss in section 3.7.4. For the following we assume that $\tau = 0.9$ and $T_{eff} = 290$ K.

3.7.4. Determination of the Directional Component of Emissivity

In the 19 – 37 GHz band (Wentz 1992) determined the V and H polarized directional signal for an EIA of 53 deg using collocated SSM/I brightness temperatures and buoy wind vectors. (Wilson and Yueh 1996) measured the 3rd and 4th Stokes parameters from aircraft radiometer – buoy overpasses at 19 GHz and 37 GHz for EIA's between 45 and 65 deg using JPL's polarimatric radiometer WINDRAD. When we began developing the CMIS RTM and wind direction retrieval algorithm these were the best data available for the wind direction signal. Our RTM therefore uses the data from (Wentz 1992) for the V and H polarized signal and the data

from (Wilson and Yueh 1996) for the 3rd and 4th Stokes parameters, where each $\Delta \mathbf{T_B}$ signal has been converted to $\Delta \mathbf{E}$ using (3.68) with $\tau = 0.9$ and $T_{eff} = 290$ K .

(Wentz 1992) referenced the wind speed to 19.5 m above surface, whereas (Wilson and Yueh 1996) referenced then to 5 m above surface. In order to convert to a wind speed 10m above surface we assume a logarithmic wind profile. The scaling law is which transforms a wind speed at height h_1 into a wind speed at height h_2 is (Peixoto and Oort 1992):

$$W_{h_1} = \frac{\ln(h_1 / z_0)}{\ln(h_2 / z_0)} W_{h_2} \quad (3.69)$$

where z_0 is the surface roughness length, which equals 1.52×10^{-4} m assuming a drag coefficient of 1.3×10^{-3} .

We expect that the wind direction signal depends weakly on EIA in the range between 53 and 58 deg. We therefore assume the values of (Wentz 1992) that had been obtained for an EIA of 53 deg and the values of (Wilson and Yueh 1996) , which we had extracted at an EIA of 55 deg, remain the same for all CMIS EIA's.

It is convenient to regress the harmonic coefficients in (3.66) to a 2nd order polynomial:

$$p(W) = p_1 W + p_2 W^2 \quad (3.70)$$

Note that the wind direction signal must vanish, if there is no wind $W = 0$, so there is therefore no constant coefficient in (3.70). We write

$$\Delta E_P = \left(\gamma_{11}^P W + \gamma_{12}^P W^2 \right) \cos\left(\varphi_r \right) + \left(\gamma_{21}^P W + \gamma_{22}^P W^2 \right) \cos\left(2\varphi_r \right), \text{ P = V or H -POL}$$
$$\Delta E_P = \left(\gamma_{11}^P W + \gamma_{12}^P W^2 \right) \sin\left(\varphi_r \right) + \left(\gamma_{21}^P W + \gamma_{22}^P W^2 \right) \sin\left(2\varphi_r \right), \text{ P = 3rd and 4th Stokes}$$

$$(3.71)$$

The authors of our model found that the signal is essentially the same for 19 GHz and 37 GHz, so we use a single set of coefficients γ_{ij}^P in the 19 – 37 GHz band as listed in Table 6. Figure 4 shows the directional emission signal with $T_S = 290$K for the models included in our RTM at 19 – 37 GHz for various wind speeds.

Table 6: The coefficients γ_{ij}^P in the 19 – 37 GHz band.

(i,j)	11	12	21	22
V-POL	+7.83E-4	-2.18E-5	-4.46E-4	+3.00E-5
H-POL	+1.20E-3	-8.57E-5	-8.93E-4	+3.76E-5
3rd STOKES	-6.45E-4	+1.75E-5	-4.93E-4	+1.59E-5
4th STOKES	-1.60E-5	0	+4.12E-4	-1.44E-5
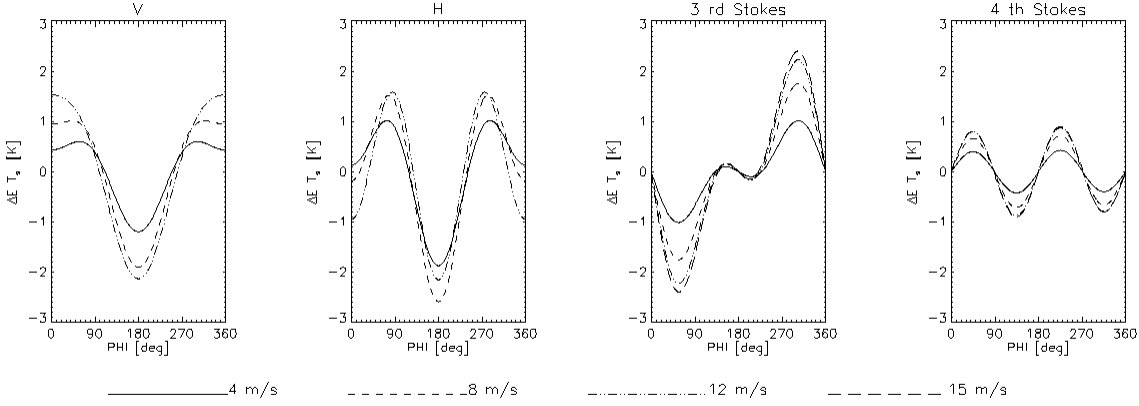
Figure 4: The wind direction emission signal ΔET_S (T_S=290K) for the directional emissivity model used in the CMIS RTM.

Little is known about the wind direction signal for frequencies below 19 GHz. Some very preliminary data from the Japanese AMSR aircraft simulations suggests that the signal for V and H polarizations decreases with decreasing frequency. Other than this, there are no experimental data on the variation of T_B versus ϕ at 6.625 and 10.7 GHz. As an educated guess, we assume that the wind direction signal for V and H pol will decrease at lower frequencies in the same way as the wind speed signal. This assumption is expressed by

$$\Delta \mathbf{E}(v) = \frac{m_1(v)\,\Delta \mathbf{E}(19-37\text{GHz})}{0.00254} \qquad (3.72)$$

where $m_1(v)$ is given by (3.60). That means we reduce the V and H-POL wind direction signals from their value at 19 GHz by a factor of 0.82 at 10.7 GHz and by a factor of 0.62 at 6.625 GHz.

The 3rd and 4th Stokes parameters are left unscaled at 10.7 GHz and 6.625 GHz from their values at 19 GHz.

3.7.5. Insertion of Wind Direction Signal $\Delta \mathbf{E}$ into RTM

For V and H polarizations, the isotropic parts of E and R were determined in sections 3.4 and 3.5. The scatter term was determined in section 3.6 (c.f. equations (3.63) and (3.64)). The total brightness temperatures T_V and T_H can therefore be obtained from the radiative transfer equation (3.11) using (3.62), where the contribution ΔE_V and ΔE_H from (3.71) has been included in E_V and E_H.

The total measured radiation is independent of the choice of the polarization basis vectors. This means that the T_B polarization sums V+H, P+M, L+R are identical:

$$T_V + T_H = T_P + T_M = T_L + T_R \qquad (3.73).$$

ATBD for CMIS
Ocean EDR Algorithm Suite
Sea Surface Temperature EDR
Sea Surface Wind Speed/Direction EDR
Surface Wind Stress EDR

14-49

This document is intended for non-commercial use only. All other use is strictly forbidden without prior approval of the U.S. Government.

We must insert the wind direction emissivity into the RTM in a way that is consistent with (3.73)
.

In the approximation (3.67):

$$E_V + E_H = E_P + E_M = E_L + E_R$$
$$R_V + R_H = R_P + R_M = R_L + R_R$$ (3.74).

The definitions of the Stokes and parameters and (3.67) imply (see <u>EN #45</u> and <u>#62</u> responses):

$$E_3 = E_P - E_M$$
$$E_4 = E_L - E_R$$ (3.75).

Now, the 3rd and 4th Stokes emissivities are pure wind direction signal, so E_3 (E_4) is synonymous with ΔE_3 (ΔE_4). Equation (3.71) provides the emissivity wind direction signal for all 4 Stokes parameters.

In case of the 3rd and 4th Stokes parameters we find from (3.74) and (3.75),

$$E_P = \frac{E_V + E_H + \Delta E_3}{2}$$
$$E_M = \frac{E_V + E_H - \Delta E_3}{2}$$
$$E_L = \frac{E_V + E_H + \Delta E_4}{2}$$ (3.76)
$$E_R = \frac{E_V + E_H - \Delta E_4}{2}$$

Here, E_V and E_H are the total emissivities, including the wind direction signals ΔE_V and ΔE_H.

Now, we must insure that we insert the wind direction signal in the RTM in a way that is consistent with (3.73). This requires determination of the scattering term for the polarimetric channels. We assume that:

$$\Omega_P = \Omega_M = \Omega_L = \Omega_R \equiv \overline{\Omega}$$ (3.77).

Because the atmospheric parameters τ, T_{BU} and T_{BD} are polarization independent, we obtain from equations (3.11), (3.62), (3.73) and (3.74):

$$1 + \overline{\Omega} = \frac{(1 + \Omega_V) R_V + (1 + \Omega_H) R_H}{R_V + R_H}$$ (3.78)

ATBD for CMIS
Ocean EDR Algorithm Suite
Sea Surface Temperature EDR
Sea Surface Wind Speed/Direction EDR
Surface Wind Stress EDR

14-50

This document is intended for non-commercial use only. All other use is strictly forbidden without prior approval of the U.S. Government.

where R_V and R_H are one minus the total emissivities for the V and H polarizations, including the wind direction component.

The radiative transfer equation (3.11) together with (3.62) and (3.78) for $\bar{\Omega}$ allows computation of T_P, T_M T_L and T_R by the RTM.

3.7.6. Comparison with Other Studies

Several theoretical attempts have been made to determine the wind direction from a two-scale model of the ocean. This model extents the geometric optics formulation by (Stogryn 1967), which studies the emission from the wind roughened ocean surface. The ocean surface is approximated by a two-scale surface where small scale capillary waves ride on top of large scale gravity waves (Wu and Fung 1972; Wentz 1975). It also includes diffraction effects and multiple scattering. Quantitative studies of the wind direction signal in all four Stokes parameters using this model have been performed by (Yueh 1997) and (Poe and St. Germain 1998; St. Germain and Poe 1998; St. Germain and Poe 1998; St. Germain and Poe 1999).

The most recent WINDRAD measurements by (Yueh and Wilson 1999; Yueh, Wilson et al. 1999) suggest substantially smaller signals for the 3rd and 4th Stokes parameters at low and moderate wind speeds than the first measurements (Wilson and Yueh 1996) did due to the inclusion of more low wind data. These studies also provide aircraft radiometer measurements for V and H pol, which suggest a smaller 1st harmonic for the H pol than (Wentz 1992) did.

A very recent reanalysis of the V and H-Pol signals in the $10 - 37$ GHz band at $\theta_i = 53$ deg used brightness temperatures from TMI and SSMI that were collocated with wind vectors from buoys and the scatterometer QUIKSCAT (Meissner and Wentz 2000). Results of this analysis suggest a substantially lower signal at low and moderate wind speeds than the original analysis by (Wentz 1992).

Figure 5 and Figure 6 compare the Peak-Peak amplitude of $\Delta\mathbf{T_B}$ from (3.68) with $\tau = 0.9$ and $T_{eff} = T_S = 290$ K, i.e. the maximum-minimum difference of the harmonic forms (3.66) at 19 GHz and 37 GHz that have been obtained by (Wentz 1992; Wilson and Yueh 1996; St. Germain and Poe 1998; Yueh and Wilson 1999; Meissner and Wentz 2000). The wind direction signal, which we will use for the performance estimates of the wind direction retrieval in section 6, correspond to the full lines. In section 6.6 we will briefly discuss how the performance of the wind vector retrieval algorithm changes if a different wind directional signal is used.

We see that at low wind speeds our signal this is close to the model calculation of (St. Germain and Poe 1998). Our signal for the 3rd and 4th Stokes parameters are a compromise between the more recent measurements (Yueh and Wilson 1999; Yueh, Wilson et al. 1999) and the theoretical calculations of (St. Germain and Poe 1998).

Figure 7 shows the Peak-to-Peak amplitude of our wind direction signal at 10.7 GHz compared with the model calculation by (St. Germain and Poe 1998).

We expect that within the next few years measurements from the ADEOS-2 AMSR and SeaWinds will become available and provide simultaneous brightness temperatures and wind vectors at all AMSR frequencies. This should enable us to further pin down the actual size of the v- and h-pol wind direction signal over the whole frequency range. Furthermore, the polarimetric radiometer WindSat, which will fly within the next couple of years, is expected to provide us with consistent data for all 4 modified Stokes parameters.
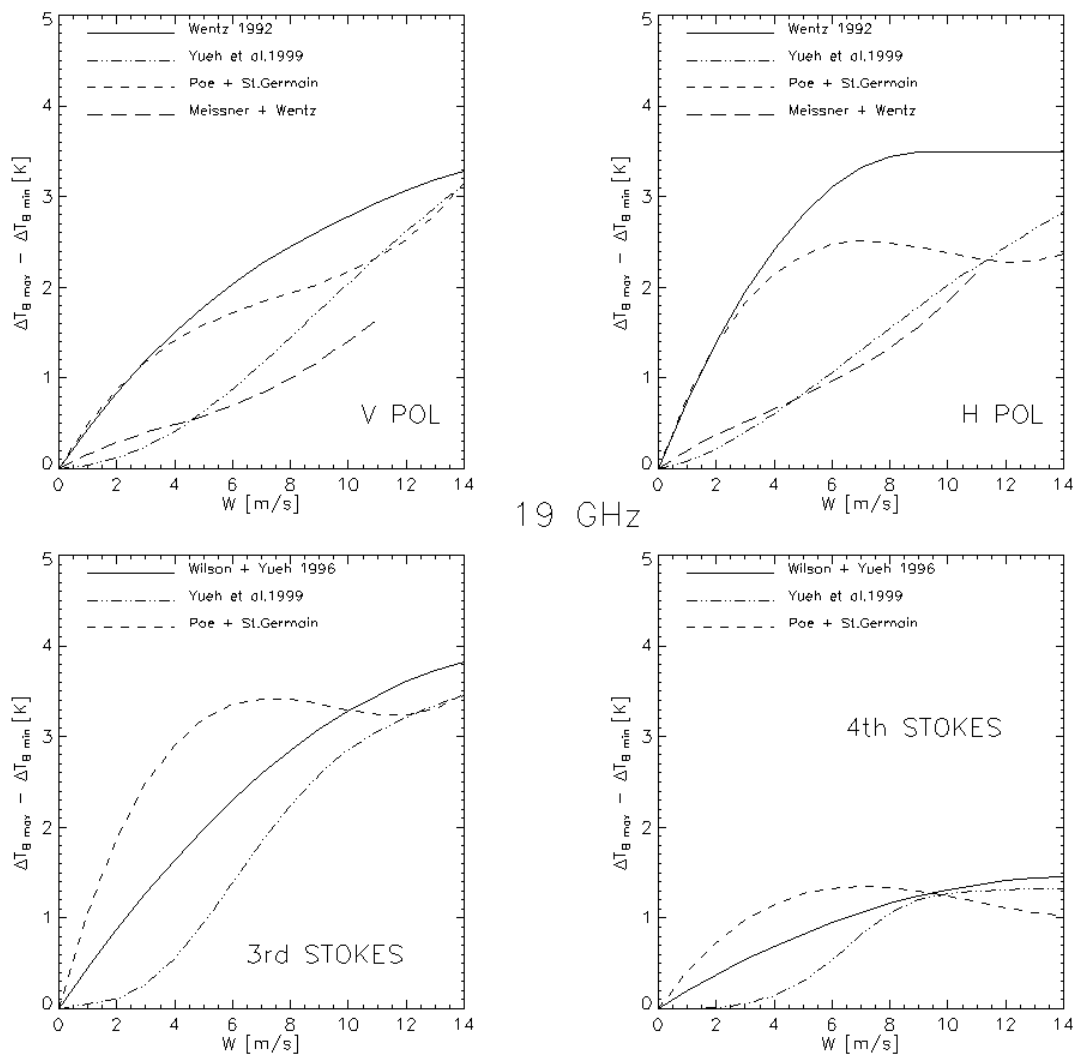
Figure 5: Wind Direction Signal for Modified Stokes Parameters at 19 GHz. The figure shows the Peak-to-Peak amplitude of T_B, i.e. the MAX-MIN value from equation (3.66). We compare (Wentz 1992; Wilson and Yueh 1996; St. Germain and Poe 1998; Yueh and Wilson 1999; Meissner and Wentz 2000). We have assumed that $\tau = 0.92$ and $T_S = 290\,K$.

ATBD for CMIS
Ocean EDR Algorithm Suite
Sea Surface Temperature EDR
Sea Surface Wind Speed/Direction EDR
Surface Wind Stress EDR

14-52

This document is intended for non-commercial use only. All other use is strictly forbidden without prior approval of the U.S. Government.
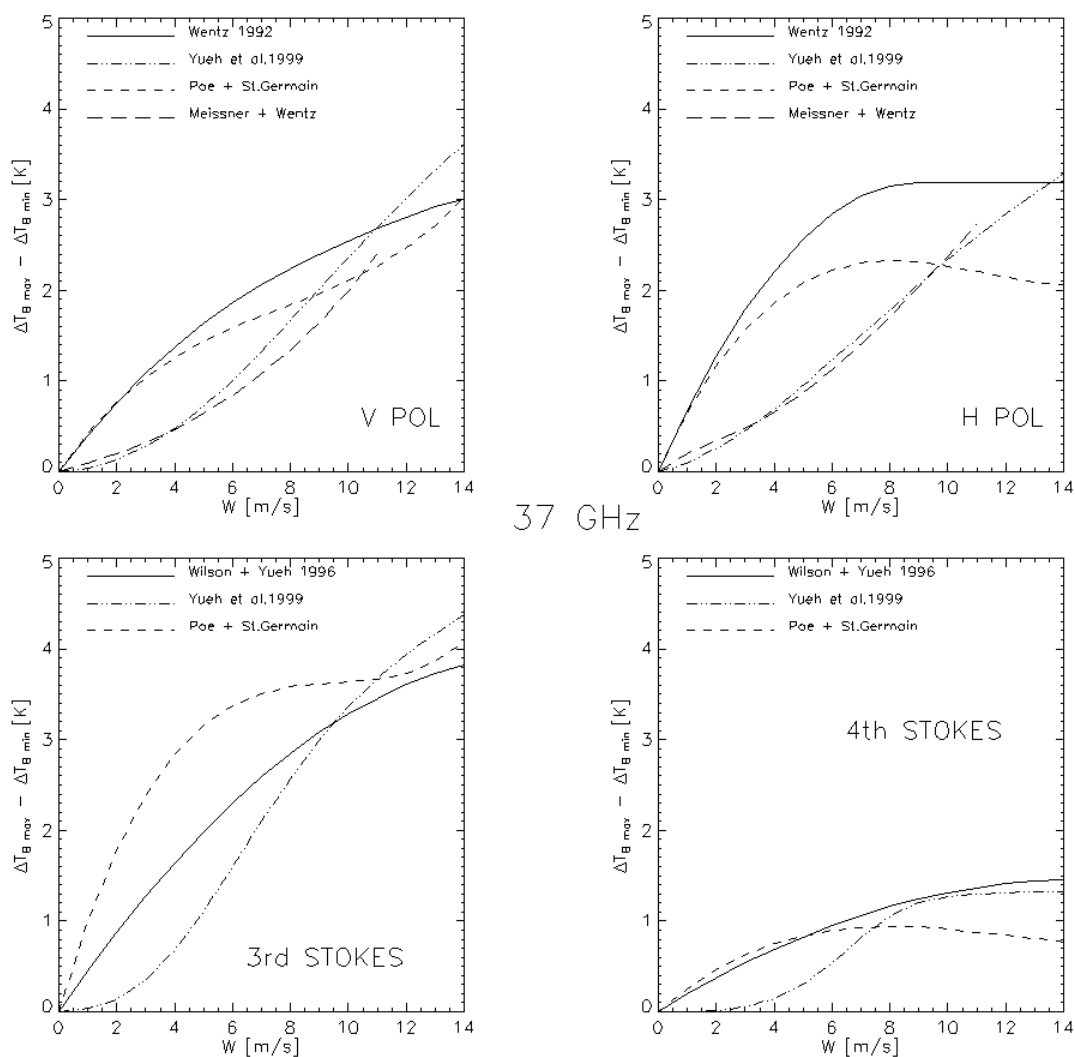
Figure 6: Wind Direction Signal for Modified Stokes Parameters at 37 GHz. The figure shows the Peak-to-Peak amplitude of T_B, i.e. the MAX-MIN value from equation (3.66). We compare (Wentz 1992; Wilson and Yueh 1996; St. Germain and Poe 1998; Yueh and Wilson 1999; Meissner and Wentz 2000). We have assumed that $\tau = 0.88$ **and** $T_S = 290\,K$ **.**
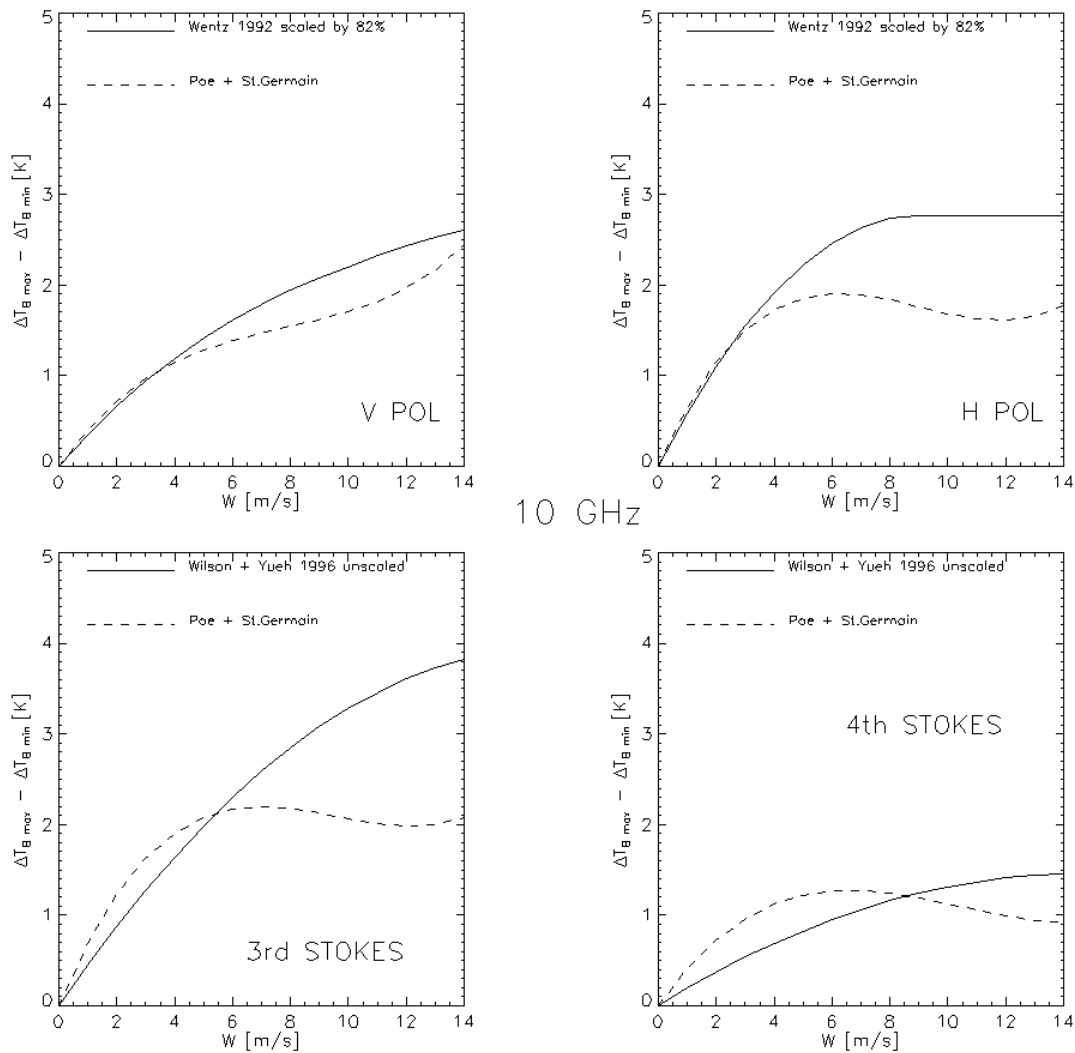
Figure 7: Wind Direction Signal for Modified Stokes Parameters at 10 GHz. The figure shows the Peak-to-Peak amplitude of T$_B$, i.e. the MAX-MIN value from equation (3.66). We compare (Wentz 1992; Wilson and Yueh 1996; St. Germain and Poe 1998; Yueh and Wilson 1999). The V and H –POL from (Wentz 1992) have been scaled by 82 % from their values at 19 GHz. The 3rd and 4th Stokes parameters from (Wilson and Yueh 1996) are the same as at 19 GHz.

ATBD for CMIS   14-54   This document is intended for non-commercial
Ocean EDR Algorithm Suite   use only. All other use is strictly forbidden without
Sea Surface Temperature EDR   prior approval of the U.S. Government.
Sea Surface Wind Speed/Direction EDR
Surface Wind Stress EDR

4. Algorithm Descriptions

4.1. Introduction

In this section, we discuss the physical basis for retrieval and give the mathematical description of each of the Ocean EDR algorithms. These are top down descriptions, so details not found in the first sub-section or two for each algorithm may be found in later subsections. Wherever useful, we back up the mathematical description with a flowchart. Channel selection and the data needed for each algorithm are also detailed, as well as the conditions under which the algorithms are trained. The data sets for algorithm training and testing (measuring performance) are described in detail in Section 5.

4.2. Top Level Ocean Algorithm Flow

4.2.1. Basic Inputs and Interdependencies

In keeping with the top down approach, we begin by describing the overall data flow for the algorithms. Figure 8 is a simplified diagram (i.e SDR geolocation data inputs not shown) of inputs of and interdependencies among the ocean EDR algorithms. The SDR geolocation inputs will be discussed in the next two subsections. All algorithms other than wind stress uses SDR derived brightness temperatures, composited to differing resolutions for different EDRs. The resolutions given in the figure are the 3dB dimensions of the composite footprints.

The reasons for the differing resolutions will be discussed shortly. But, we draw the reader's attention to the distinction between the two wind speeds reported. We are reporting the wind speed determined by the wind vector algorithm, which we call the low resolution wind speed (LR wind speed), with the wind direction. We find this necessary if the customer wishes to interpolate the wind vectors from a scan based to some other grid system; scalar or vector methods using only the wind direction tend to produce less accurate results. But, the LR wind speed in all likelihood will not meet the 20 km SDR Horizontal Cell Size requirement, as the composite cell size is 56 x35 km. Therefore, in order to meet all Category IA EDR requirements, we provide another wind speed that will meet the 20 km requirement. When we say wind speed EDR, it is this wind speed to which we are referring.

The SST algorithm depends on no other EDRs. The wind vector algorithm requires as input the SST from a circumscribing SST composite cell. The wind speed EDR algorithm depends on no other EDRs. The wind stress algorithm requires no input other than the high resolution (20 km) wind speed EDR .

ATBD for CMIS
Ocean EDR Algorithm Suite
Sea Surface Temperature EDR
Sea Surface Wind Speed/Direction EDR
Surface Wind Stress EDR

14-55

This document is intended for non-commercial use only. All other use is strictly forbidden without prior approval of the U.S. Government.
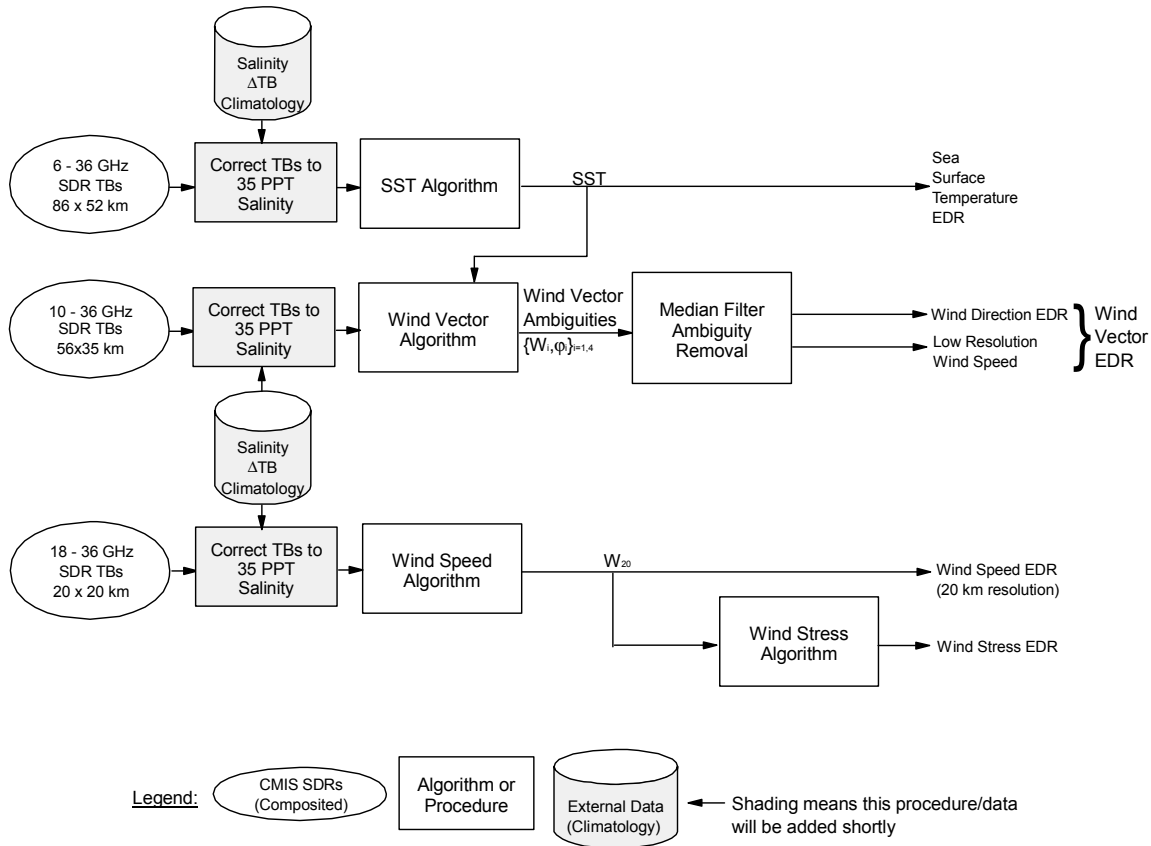
Figure 8: Top Level Flow Diagram for Ocean Algorithms

4.2.2. Salinity Correction

Each CMIS EDR algorithm is tuned or trained to a ocean salinity (s) of 35 PPT. Like their SSM/I and TMI predecessors, each of these algorithms will use a monthly sea surface salinity correction map to correct the TBs for all channels to a common salinity of 35 PPT. These climatology maps are created from the World Ocean Atlas salinity climatology and the Reynolds SST climatology whenever either of these climatologies are updated. We use the WOA salinity because it is updated most frequently of any climatology salinity, and has worked well with our TMI SST algorithm.

The maps are created by determining TB(s=35, SST)-TB(s, SST) at the nominal EIA for each channel, using the radiative transfer model of the last section, and s and SST from the two climatologies; that it should be determined as a function of SST is demonstrated by the cross-terms between salinity and SST in the dielectric constant for sea water (equations (3.34) through (3.39)). The maps are created on a 1 degree latitude-longitude grid, and are tri-linearly interpolated to time of the observation and the beam center of the composite footprint in the EDR algorithm.

We have kept the use of external data to a minimum, and the only non-CMIS data needed by the algorithms is this simple climatology. We do not anticipate any loss of this climatology, since the data files are kept with the algorithm. Each algorithm also needs the time, latitude and

ATBD for CMIS
Ocean EDR Algorithm Suite
Sea Surface Temperature EDR
Sea Surface Wind Speed/Direction EDR
Surface Wind Stress EDR

14-56

This document is intended for non-commercial
use only. All other use is strictly forbidden without
prior approval of the U.S. Government.

longitude of the observations, so the ΔTB climatology can be interpolated. Each algorithm also requires the EIA of the 37 GHz observations, as shown in the next subsection.

4.2.3. Accommodating the EIA Range in the EDR Algorithms

4.2.3.1. EIA Considerations

The earth incidence angle for any frequency v can be computed as

$$\sin\theta_i(v) = \frac{R'_E + H'_{SC}}{R'_E}\sin\theta_n(v) \qquad (4.1)$$

Here, R'_E is the effective radius of curvature of the earth at the latitude of the observations, H'_{SC} is the spacecraft altitude, and $\theta_n(v)$ is the nadir angle of the observations at frequency v (Wentz 1991). Therefore we expect the EIA to vary from observation to observation due to (1) oblateness of the Earth, (2) ellipticity of the orbit, and (3) changes is CMIS attitude (nadir angles).

The nominal EIAs, $\theta_i^0(v)$, in Table 2 were computed using the nominal radius of the earth (R_E) as 6371 km, the nominal altitude, H_{SC} (833 km), and the nominal nadir angles for each frequency ($\theta_n^0(v)$) as given in that table:

$$\sin\theta_i^0(v) = \frac{R_E + H_{SC}}{R_E}\sin\theta_n^0(v) \qquad (4.2)$$

Using our orbit simulator, which will be described later, we find that oblateness of the earth by itself causes, for example, the 36 GHz EIA to vary from 55.58 to 55.87, which is up to a 0.21 deg deviation from the nominal (we use 36 GHz as example, as it has the median nadir angle across the 6-36 GHz range). Ellipticity of the orbit can also have a significant effect on the EIA. For SSM/I, the slight eccentricity (ε=0.0015), combined with the earth oblateness results in a +/- 0.25 degree EIA variation; for F10 (ε=0.0085) the EIA variation is +/- 0.75 deg (Wentz 1991). For the CMIS orbit, where the altitude can vary between 816 and 850 km, equation (4.1) with R'_E=R_E shows that the 36 GHz EIA can vary by +/-0.20 deg.

On the other hand, differentiation of equation (4.1), with the nadir angle, earth radius spacecraft and altitude set to the nominal values, shows that the 36 GHz EIA variation will be 1.37 times the nadir angle control error. Given that the CMIS Interface Requirement Document (CMIS IPO, 1998) states that the spacecraft attitude will be controlled to 0.01 deg under normal circumstances, the variation in EIA due to attitude control will be the smallest component of EIA variation.

Given the above, we want to accommodate a wide range of EIAs (+/- 1.0 deg, to be safe) in our algorithms. For physical algorithms, the exact EIA that is reported for each frequency can be used in the retrievals. However, all of our algorithms are either regressions or depend upon regressions. Our investigation of the change in TBs with the change in EIA shows that the TB

ATBD for CMIS
Ocean EDR Algorithm Suite
Sea Surface Temperature EDR
Sea Surface Wind Speed/Direction EDR
Surface Wind Stress EDR

14-57

This document is intended for non-commercial use only. All other use is strictly forbidden without prior approval of the U.S. Government.

change is very linear over a 0.5 deg change in EIA. Therefore, we develop 5 regression algorithms, for deviations of -1.0, -0.5, 0.0, 0.5, and 1.0 degree increments from the nominal EIA. But which nominal EIA? There will be three different EIAs, corresponding to the three different nadir angles for the 6-36 GHz channels. Futhermore, the change in these EIAs with respect to a change in any of earth effective radius, altitude, or nadir angle, will be different.

We have chosen a regression method that allows us to index the regressions to the reported EIA for one frequency (36 GHz). This method treats the change in the other EIAs exactly with respect to earth oblateness and ellipticity of the orbit, the two largest factors in causing the EIA to deviate from nominal. That is, with respect to a change in earth effective radius or spacecraft altitude, there is zero difference between the EIAs for the other frequencies that are assumed in the regressions and the actual EIAs at those frequencies. However, the method does not treat the change in EIAs with repect to a change in nadir angles exactly, requiring us to set a requirement on the nadir angle control error for the spacecraft.

The regression method can be derived as follows. From equation (4.1), it can be seen that, for observations at two different frequencies for the same earth location,

$$ \frac{\sin\theta_i(\nu)}{\sin\theta_i(36)} = \frac{\sin\theta_n(\nu)}{\sin\theta_n(36)} \qquad (4.3) $$

This equation is exact under all circumstances. Given that the nadir angle variation, as discussed above, will be on the order of 0.01 deg under normal circumstances we can further approximate the nadir angles by their nominal values to obtain

$$ \sin\theta_i(\nu) \approx \left(\frac{\sin\theta_n^0(\nu)}{\sin\theta_n^0(36)} \right) \sin\theta_i(36) \qquad (4.4) $$

4.2.3.2.   Accomodating EIA Variation in the Regressions

Therefore, the procedure for defining the regression coefficients is as follows. For each ½ degree increment in the 36 GHz EIA around the nominal value, we define the values of the EIAs for all other frequencies using equation (4.4), i.e.

$$ \sin\theta_i^{reg}(\nu) \equiv \left(\frac{\sin\theta_n^0(\nu)}{\sin\theta_n^0(36)} \right) \sin\theta_i(36) \qquad (4.5) $$

and the nominal nadir angles from Table 2. We then develop a training dataset, as described in Section 5, using this set of EIAs. Then a regression algorithm is trained for this dataset. We then repeat this process for each increment in the 36 GHz EIA, and have only 5 sets of regression coefficients when finished.

In the retrievals, we use the reported 36 GHz EIA and the 2 sets of coefficients bracketing this value to interpolate the regression coefficients. Thus, all regressions are keyed to the 36 GHz EIA.

ATBD for CMIS
Ocean EDR Algorithm Suite
Sea Surface Temperature EDR
Sea Surface Wind Speed/Direction EDR
Surface Wind Stress EDR

14-58

This document is intended for non-commercial use only. All other use is strictly forbidden without prior approval of the U.S. Government.

4.2.3.3. Robustness in Conditions where Nadir Angles Change

Equation (4.5) is exact when the nadir angles are fixed at the nominal values. However, we prefer algorithms that continue to work well under adverse circumstances, such as temporary loss or degradation of attitude control (i.e., when the nadir angles change). Therefore, we perform the following sensitivity analysis to determine the error in equation (4.5) when nadir angles depart from nominal.

If the spacecraft attitude slew rate is slow, then the nadir angle control error will not change appreciably between the successive scans necessary for all 6-36 GHz feeds to observe the same spot on the earth. This means that each frequency has the same nadir angle offset, $\Delta\theta_n$:

$$\theta_n(v) = \theta_n^0(v) + \Delta\theta_n \quad (4.6)$$

The question is then, what is the error in using equation (4.5) to define the EIAs in the training data when the nadir angles vary as per equation (4.6)? Stated another way, what is the difference between the EIAs reported by the SDR geolocation algorithm and those assumed in the regressions when the nadir angle varies? To determine this, we plug equation (4.6) into equation (4.1), assuming the nominal earth radius and altitude, to compute the EIA that would be reported by the SDR geolocation algorithm for all frequencies. Then we use the 36 GHz EIA that would be reported to compute the EIAs assumed in the regressions using equation (4.5). We then find the difference between the assumed and reported EIAs for each frequency:

$$\Delta\theta_i(v) \equiv \theta_i^{reg}(v) - \theta_i(v) \quad (4.7)$$

The results are shown in Table 7.

Table 7: Errors in the EIAs Assumed for the Regression Coefficients as a Function of Nadir Angle Departure from Nominal (Nadir Angle Control Error)

$\Delta\theta_n$	$\Delta\theta_i(6)$ (deg)	$\Delta\theta_i(10)$ (deg)	$\Delta\theta_i(18)$ (deg)	$\Delta\theta_i(23)$ (deg)
0.05	0	0.0044	-0.0036	-0.0036
0.10	0	0.0087	-0.0073	-0.0073
0.15	0	0.0131	-0.0110	-0.0110
0.20	0	0.0175	-0.0146	-0.0146

The error in the 6 and 36 GHz EIAs are of course, zero: they share the same nadir angle, and the reported EIA for both frequencies is derived from this nadir angle. Without doing extensive simulation to determine the EDR sensitivity to this particular error, we consider an error on the order of 0.01 deg in the EIAs assumed in the regressions to be acceptable. This means that we must set a nadir angle control error requirement of 0.12 deg—hard limit.

There is an alternate method for defining the EIAs assumed in the regressions that we have explored extensively. In that method, we define the EIAs for the training data by finding the departure of the 36 GHz EIA from nominal, and add that to the nominal EIAs for all other frequencies. That is, for all 6-36 GHz frequencies.

ATBD for CMIS
Ocean EDR Algorithm Suite
Sea Surface Temperature EDR
Sea Surface Wind Speed/Direction EDR
Surface Wind Stress EDR

14-59

$$\theta_i^{reg}(v) = \theta_i^0(v) + [\theta_i(36) - \theta_i^0(36)] \quad (alternate\ method) \quad (4.8).$$

In other words, the sets of regression coefficients have assumed EIAs that depart from the nominal set by an identical amount (-1.0, -0.5,..., or 1.0 deg) for all frequencies. Like the chosen method, $\Delta\theta_i$ for 6 and 36 GHz is zero. Unlike the chosen method, $\Delta\theta_i$ is not zero for 10-23 GHz, regardless of whether it is the earth effective radius, altitude, or nadir angle that departs from nominal. This is a disadvantage with respect to the chosen method, which has $\Delta\theta_i$ equal to zero for earth effective radius and altitude variations from nominal. However, the errors in Table 6 are exactly halved using this method, and $\Delta\theta_i$ due to earth oblateness is less than 0.0043 deg (negligible) over the globe. The real weakness of this method is that $\Delta\theta_i$ reaches 0.018 deg when the altitude departure from nominal is 16 km (corresponding to the maximum and minimum altitude).

This disadvantage could be fixed by having three sets of regression coefficients, one for each of −16, 0, 16 km altitude departures from nominal, for each 0.5 degree increment in the 36 GHz EIA. But, one then has 3x5=15 sets of regression coefficients for each regression, and the interpolation becomes more complex.

We have used the chosen method to determine our regression coefficients, because (1) the EIAs assumed for the regressions exactly match the EIAs that would be reported by the SDR geolocation algorithm for each frequency, with respect to earth effective radius and altitude changes, and (2) it appears from the IRD that, under normal circumstances, the nadir control error will be small enough (on the order of 0.01 deg) that error in the assumed EIAs due to this effect will be negligible. However, this method results in a derived requirement of 0.12 deg (hard limit) for the nadir angle control error. Yet, if we determine that the government or spacecraft contractor would prefer a larger nadir angle control error requirement, we can easily double it to 0.24 deg by switching to the alternate method using 15 sets of regression coefficients.

4.3. Sea Surface Temperature Algorithm

4.3.1. Physical Basis

The signature of the SST (T_S) signal across frequency and polarization is defined mainly by the specular emissivity obtained through equations (3.30) to (3.43). Figure 9 shows the contribution of the term ET_s in equation (3.11), where we consider only the specular emissivity (one minus the specular reflection coefficient of equation (3.42)). The salinity is 35 PPT, and the earth incidence angle in equations (3.40) and (3.41) is 55 degrees. Keep in mind that this term is reduced by the atmospheric transmission at each frequency (not shown in the figure), which can be significantly less than one for the 18-36 GHz channels.

ATBD for CMIS
Ocean EDR Algorithm Suite
Sea Surface Temperature EDR
Sea Surface Wind Speed/Direction EDR
Surface Wind Stress EDR

14-60

This document is intended for non-commercial use only. All other use is strictly forbidden without prior approval of the U.S. Government.
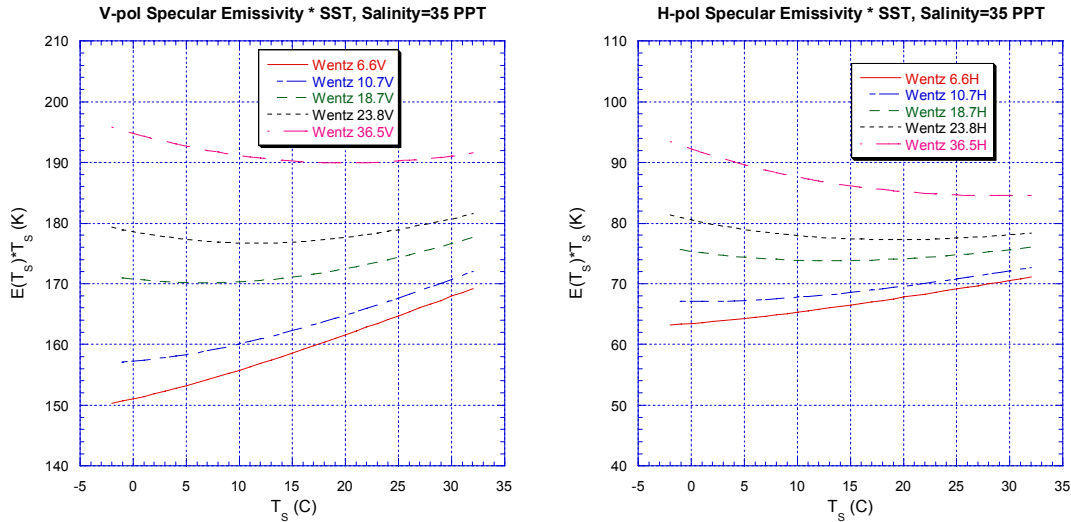
Figure 9: Specular Emission Component ($E_{specular}*T_S$) of SST Signal

The figure corroborates the finding from our TMI studies that the use of 10-36 GHz channels alone is insufficient for accurate retrieval of SST in cold water (less than 15C); the derivative $\partial(ET_s)/\partial T_s$ at 10 GHz is too small below 15C to allow retrieval algorithms to differentiate between small changes in T_S. On the other hand, the 6 GHz channels show little decline in the derivative in cold water. This is why the 6 GHz channels (especially 6V, which shows the largest deriviative) are required for SST retrieval at the low end of the measurement range. At 6 GHz, the full TB signature, $\partial T_B/\partial T_S$, is roughly 0.5K/K for the vertical polarization, and about half that for the horizontal polarization.

4.3.2. Mathematical Description

4.3.2.1. The Basic Algorithm

The SST algorithm is a pure statistical (regression) algorithm of the form

$$T_S = c_0 + \sum_{i=1}^{18} a_i t_i + \sum_{i=1}^{18} b_i t_i^2 \qquad (4.9)$$

The arguments are related to the input TBs as

$$\begin{aligned} t_i &= T_{Bi} - 150K, \quad \textit{all channels except } 23 \textit{ GHz} \\ t_i &= -\ln(290K - T_{Bi}), \quad 23 \textit{ GHz channels} \end{aligned} \qquad (4.10)$$

Taking the logarithm at 23 GHz reduces the variance of the TBs for channels sensitive to water vapor, which tends to reduce the EDR retrieval errors.

All eighteen 6-36 GHz channels are used in the regression. The index i in equations (4.9) and (4.10) corresponds to the 18 channels listed in Table 5.

Table 8: Index of Channels used in Regressions

i	1	2	3	4	5	6	7	8	9	10	11	12	13	14	15	16	17	18
Freq	6	6	10	10	10	10	18	18	18	18	18	18	23	23	36	36	36	36
POL	V	H	V	H	L	R	V	H	P	M	L	R	V	H	V	H	P	M

The coefficients a_i, b_i, c_0 are determined from a standard least squares fit on the set of SSTs and TBs from the training data sets that will be discussed in Section 5. Gaussian noise is added to the TBs in the least squares fit to simulate radiometer noise. The sigma of the Gausian parent population is given by the effective NEDTs, which are obtained by multiplying the single observation NEDTs by the effective noise reduction factors (NRF_{eff}). The effective noise reduction factors are obtained from equation (2.15) and the data in Table 3; the NRFs for footprint compositing (optimal interpolation) to the 86 x 52 km retrieval resolution are supplied by AER.

Table 9 lists the channels used in the algorithm and the typical effective NEDTs for each channel. Also shown is the AER supplied NRF, the effective NRF, and the effective calibration amplification factor, defined as the NRF_{eff}/NRF. Once can see that the effective calibration amplification factors that result from a detailed treatment of the calibration in Section 2.7.3 are larger than the calibration amplification factor that would be determined using the standard equation $\sqrt{1+1/N_{cal}}$; we are penalizing our performance slightly by treating the calibration in a more detailed fashion.

In training or assessing the performance of the algorithms we use the effective NRFs, as shown in the table, to transform the single ocean observation NEDTs (computed for each observation) to the effective NEDTs for the composite TBs (inputs).

Table 9: Channels used in the SST Algorithm, Noise Reduction Factors from Compositing, and Typical Effective NEDTs for SST Algorithm Training and Testing.

Channel	NRF	NRF_{eff}	CA_{eff}	Typical $NEDT_{eff}$ (K)
6V	0.243	0.280	1.153	0.085
6H	0.243	0.275	1.133	0.069
10V	0.128	0.165	1.292	0.116
10H	0.128	0.156	1.221	0.082
10L,R	0.128	0.159	1.244	0.104
18V	0.081	0.109	1.347	0.106
18H	0.081	0.104	1.280	0.088
18P,M	0.081	0.106	1.309	0.096
18L,R	0.081	0.105	1.301	0.110
23V	0.080	0.110	1.378	0.098
23H	0.080	0.106	1.320	0.087
36V	0.081	0.111	1.367	0.063
36H	0.081	0.105	1.297	0.055

ATBD for CMIS
Ocean EDR Algorithm Suite
Sea Surface Temperature EDR
Sea Surface Wind Speed/Direction EDR
Surface Wind Stress EDR

14-62

| 36P,M | 0.081 | 0.108 | 1.329 | 0.058 |

4.3.2.2.   Earth Incidence Angle Handling

To accommodate variations in EIA, the algorithm uses 5 sets of regression coefficients, spaced in 0.5 degree increments around the 36 GHz nominal EIA, as discussed in Section 4.2.3.2. In the retrieval algorithm, we linearly interpolate the regression coefficients to the 36 GHz EIA reported with the observations.

4.3.3. Data Required by the SST EDR Algorithm

The CMIS Data required by the algorithm consists of:

(1) The 6-36 GHz SDR derived brightness temperatures, composited to the 86 x 52 km resolution (3dB beamwidth).

(2) The earth incidence angle of the 36 GHz feeds. This is obtained from the SDR geolocation algorithm, and is used to interpolate the regression coefficients for each retrieval.

(3) Geographic latitude and longitude of the center of the 86 x 52 km composite retrieval cell, and the date of the observation. The source is the SDR geolocation algorithm, and they are used for determination of the ΔTB salinity correction for each observation, discussed in Section 4.2.2.

The external data required by the algorithm are the monthly ΔTB salinity correction maps, discussed in the same section. We anticipate no loss of this external data source, as they are static files are kept with the algorithm.

4.4. Wind Speed EDR (20km Wind Speed) Algorithm

4.4.1. Physical Basis

Wind roughens the sea surface, and therefore changes the isotropic component of the surface emissivity. The facets of waves with wavelengths that are long compared to the wavelength of the radiation considered mix the polarization states of the radiation and change the local incidence angle (Section 3.5, in specific the introductory paragraphs and equation (3.56)).

Furthermore, foam, which is a mixture of air and sea water, increases the emissivity of the surface. Short waves (capillary waves) diffract the microwave radiation. Foam and diffraction are modeled together in our RTM (equations (3.46) and (3.57) through (3.61)). Foam appears at about 7 m/s, and its effect on the isotropic emissivity overtakes that of diffraction at about 12 m/s. These are the major effects of wind speed on the brightness temperatures, but there are other smaller effects such as the fact that atmospheric radiation reflected into the CMIS beams

come from a range of incidence angles (equations (3.54) and (3.55) plus (3.62) through (3.64)) that depends on surface roughness i.e., wind speed.

Unlike the SST signature, which is stronger in the vertical channels, and decreases with frequency above 6 GHz, the wind speed signature is mainly in the horizontally polarized channels, and tends to increase with frequency. $\partial T_V / \partial W$ is small and positive for EIAs less than 55 degrees, but crosses zero between 55 and 60 degrees, the exact value depending on frequency. On the other hand, $\partial T_H / \partial W$ is roughly 0.8K/(m/s) at 18 GHz and EIA=55 degrees, and increases with EIA. The magnitude of $\partial T_B / \partial W$ tends to increase with wind speed for both polarizations, due to the quadratic (cubic between 7-12 m/s) dependence of the isotropic reflectivity (emissivity) on wind speed (equations (3.46), (3.56) , and (3.57) through (3.59)). The signature of wind speed in the polarimetric channels is the average of the vertical and horizontally polarized signatures.

4.4.2. Mathematical Description of Algorithm

4.4.2.1. The Basic Algorithm

The wind speed EDR algorithm is designed to meet all EDR requirements, especially the horizontal cell size requirement of 20km. That is the composite footprint (3dB) size is 20 km, and so we expect little spatial error between the retrieval and the uniform average of wind speed over the 20x20 km square horizontal cell. Therefore, we denote this wind speed by W_{20}. It is a pure regression algorithm, analogous to the SST algorithm:

$$W_{20} = c_0 + \sum_{i=7}^{18} a_i t_i + \sum_{i=7}^{18} b_i t_i^2 \quad (4.11)$$

But, here only the twelve 18-36 GHz channels are used (all polarizations). The definitions of the t_i's are the same as for the SST algorithm (equation (4.10)), and the regression coefficients are derived in the same way.

Table 10 gives the channels used in the algorithm, the NRFs for compositing to the 20 km retrieval cell, the effective NRFs, and typical effective NEDTs, computed using the method of Section 2.7. Also shown are the effective calibration amplification factors, computed as NRF_{eff}/NRF. Because the NRFs are much larger than those for the SST composite cell,, the efect of the calibration on the efective NEDTs is not as significant (c.f. equation (2.15)).

When computing the actual effective NEDTs for training and testing the algorithms, we use the effective NRFs from Table 10 to transform the single ocean observation NEDTs (computed for each observation) to the effective NEDT for the composite TBs (inputs).

Table 10: Compositing and Effective NRFs, Effective Calibration Amplification Factors, and Mean Effective NEDTs for the (20 km) Wind Speed EDR Algorithm

Channel	NRF	NRF$_{eff}$	CA$_{eff}$	Typical NEDT$_{eff}$

18V	0.440	0.446	1.014	0.433
18H	0.440	0.445	1.011	0.376
18P,M	0.440	0.445	1.012	0.404
18L,R	0.440	0.445	1.012	0.465
23V	0.440	0.446	1.015	0.396
23H	0.440	0.445	1.012	0.368
36V	0.418	0.425	1.016	0.240
36H	0.418	0.423	1.013	0.220
36P,M	0.418	0.424	1.014	0.230

4.4.2.2. Earth Incidence Angle Considerations

The earth incidence angle variation is handled exactly the same as for the SST algorithm. 5 sets of regression coefficients are generated, corresponding to 0.5 degree increments in the 36 GHz EIA. During retrieval, the regression coefficients are interpolated using the reported 36 GHz EIA.

4.4.3. Data Required by the Wind Speed EDR Algorithm

The CMIS data required by the algorithm consist of:

(1) CMIS SDR derived 18-36 TBs, composited to the 20 km resolution (3dB beamwidth).

(2) The reported EIA for 36 GHz. This is obtained from the SDR geolocation algorithm, and is used to interpolate the regression coefficients for each retrieval.

(3) The geographic latitude and longitude of the center of the composite footprint, and the date of the observation. The source is the SDR geolocation algorithm, and the data is used for the determination of the ΔTB salinity correction, as discussed in Section 4.2.2.

The external data required by the algorithm are the monthly ΔTB salinity correction maps, discussed in the same section. We anticipate no loss of this external data source, as they are static files are kept with the algorithm.

4.5. The Wind Direction EDR Algorithm

4.5.1. Physical Basis

The physical basis of the wind direction retrieval algorithm is the variation of the modified Stokes vector, $\mathbf{T_B}$,defined in equation (3.65), with relative wind direction φ_r, as discussed in Section 3.7. Given the periodic nature of this signal, there are several relative wind directions (ambiguities) that correspond to the modified Stokes parameter for a given value of φ_r. However, the periodic wind direction signal is different for modified Stokes parameter (c.f. Table 6 and Figure 4). Thus, including effective NEDTs, each Stokes parameter will have an

ambiguity close to the true wind direction, but the other ambiguities will generally lie at different wind directions for different modified Stokes parameters.

This is the basis of the wind direction retrieval; we rely on the fact that the periodic signal is different for each modified Stokes parameter to rank the ambiguities in terms of goodness of fit (χ^2) to the modified Stokes vector. If the periodic signals were identical across all four Stokes parameters, there would be no way to distinguish between the ambiguities; they would all result in the same χ^2.

4.5.2. Mathematical Description

4.5.2.1. Basic Concepts

The wind direction algorithm is a hybrid statistical/physical algorithm using all 10-36 GHz channels. Basically, regressions are used to fill in all values except wind speed and direction in an RTM based TB model function, and then a search in wind speed and direction is performed to minimize the sum-square difference between the model function and the measurements.

Combining equations (3.11), (3.29), and (3.62) gives an expression for the top of the atmosphere brightness temperature as

$$T_B = T_{BU} + \tau\left\{ET_S + (1-E)\left[(1+\Omega)\left(T_{BD} + (1-\tau)T_C\right) + T_C\right]\right\} \quad (4.12)$$

The up-welling atmospheric radiation at the top of the atmosphere (T_{BU}), the down-welling atmospheric radiation at the surface (T_{BD}), and the atmospheric transmission (τ) are independent of the surface parameters. These atmospheric parameters, as well as the cold space temperature (T_C), depend on frequency but are assumed to be independent of polarization in the forward model.

In the forward model, the total surface emissivity depends on the sea surface temperature, wind speed, relative wind direction, and EIA (equations (3.30), (3.31), (3.33) to (3.43), (3.46), (3.56) to (3.59), and (3.71)):

$$E = E(\theta_i, T_S, W, \varphi_r) \quad (4.13)$$

It is also a function of frequency and polarization (and salinity s, although we correct the observations to s = 35 PPT in pre-processing, so we implicitly include that parameter here).

The scattering term depends on the atmospheric transmission and wind speed (equations (3.54), (3.55), (3.63), and (3.64)), and for the polarimetric (P, M, L, R) polarizations, on the V and H reflectivity as well (equations (3.77) and (3.78)):

$$\Omega = \Omega(W, \tau; E_V, E_H) \quad (4.14)$$

ATBD for CMIS
Ocean EDR Algorithm Suite
Sea Surface Temperature EDR
Sea Surface Wind Speed/Direction EDR
Surface Wind Stress EDR

14-66

This document is intended for non-commercial use only. All other use is strictly forbidden without prior approval of the U.S. Government.

Therefore, it is sufficient to know T_{BU}, T_{BD}, τ at each frequency, and T_S, W, and φ_r (and s) to compute the model function at any frequency and polarization for a given EIA.

Therefore, the idea of the algorithm is to use equation (4.12) for the model function, denoted F, and use regressions to fill in T_{BU}, T_{BD}, τ, and T_S in the model function (i.e., all needed parameters except W and φ_r).

$$F(W,\varphi_r) = F(W,\varphi_r; T_{BU,reg}, T_{BD,reg}, \tau_{reg}, T_{S,reg}) \quad (4.15)$$

T_S is obtained from the SST EDR retrieval on a circumscribing SST retrieval cell. Regressions for the three atmospheric parameters are described in the next sub-section.

Once the model function is filled in, a search is then performed in the space of wind speed and direction in order to find local minima of the χ^2 function given below

$$\chi^2(W,\varphi_r) = \sum_{\alpha=1}^{12} \frac{\left[T_{B_\alpha} - F_\alpha(W,\varphi_r) \right]^2}{\Delta_\alpha^2} \quad (4.16)$$

i.e., in order to find a sets of values for $\{W,\varphi_r\}$ which best fit the model function to the measurements. The search is started with an initial value for the wind speed obtained using a regression using all 10-36 GHz channels (described in section 4.5.2.3).

Instead of using the individual polarized measurements and model functions in the χ^2, we use the modified Stokes parameters, which include the vertical (V), horizontal (H) polarizations as well as the 3rd (U), and the 4th (4) Stokes parameters. This has the effects of (1) canceling out most of the atmospheric signal in the χ^2 that is present in the individual P, M, L, and R polarized measurements, and (2) reducing the influence of the errors in the regressions for T_{BU} and T_{BD} on χ^2 that is in the model function for the same polarizations.

To be explicit, we list the modified Stokes parameters (defined in equation (3.65)) used in the algorithm in the following table.

Table 11: Modified Stokes Parameters Used in the χ^2 for the Wind Vector Search

α	1	2	3	4	5	6	7	8	9	10	11	12
Frequency	10	10	10	18	18	18	18	23	23	36	36	36
Stokes Parameter	V	H	4	V	H	3	4	V	H	V	H	3

For a true χ^2 function, Δ_α^2 would be the expected variance of the difference between the model function and measurements, i.e. the variance of the "modeling error" in F_α. Functionally, Δ_α^2 can be obtained as the variance over the test data set of the difference between $T_{B\alpha}$ and F_α, where the true values of W and φ_r (and the regression values for T_{BU}, T_{BD}, τ and retrieval value for T_S) are used in computing F_α, and the effective NEDT's in Table 12 have been added to the T_B's before the regressions and before forming $T_{B\alpha}$. However, we find weighting by the

ATBD for CMIS
Ocean EDR Algorithm Suite
Sea Surface Temperature EDR
Sea Surface Wind Speed/Direction EDR
Surface Wind Stress EDR

14-67

modeling error under-weights the terms for the 3rd and 4th Stokes parameters relative to those for the V and H polarizations, and results in inferior wind direction performance than if we do not apply any weighting at all. If we increase the weighting the 3rd and 4th Stokes terms in (4.16) more than those for the V and H polarizations, then we obtain inferior wind speed product. We therefore do not weight the χ^2 function at all, and set: $\Delta_\alpha = 1\text{K}$ for all α in (4.16).

Each set of values for $\{W, \varphi_r\}$ obtained from the search is called a wind vector ambiguity. The ambiguity which results in the smallest χ^2 is denoted the first rank ambiguity, the ambiguity which results in the next smallest value of is denoted the second rank ambiguity, and so on. Two to four ambiguities are retrieved. As we find in the wind direction performance section, the fourth rank ambiguities are never found to be the closest ambiguity to the true wind direction, and are never selected by the median filter. Therefore, it is perfectly acceptable to truncate the list of retrieved ambiguities after the third rank.

In post processing, the wind vector ambiguities for all retrievals in a half orbit are assembled into a rectangular array indexed by scan position and scan number (and rank), and a median filter (MF) is applied to select the ambiguity for each cell.

To recount, the basic steps in the wind vector retrieval algorithm are:

1. Determine the required geophysical parameters. Take T_S as the SST retrieval on a circumscribing SST retrieval cell. Perform regressions to find τ, T_{BU} and T_{BD} for each 10-36 GHz frequency. Perform a regression to obtain a wind speed estimate to initialize the next step.

2. Fill in the model function for all 10-36 GHz channels with the required parameters. Then apply a χ^2 minimization algorithm to determine the local minima. In general, the minimization results in multiple solutions (ambiguities); these are ranked from lowest to highest χ^2.

3. In post processing, assemble the set of ambiguities for each retrieval in a half orbit into a scan geometry based array, and apply a circular median filter for selecting one ambiguity as a final solution for each retrieval.

A flowchart of the entire wind vector algorithm is shown in Figure 10.

4.5.2.2.   Regressions for the Atmospheric Parameters

There are 3 atmospheric parameters (T_{BU}, T_{BD}, τ) to determine at the four 10-36 GHz frequencies, so there are 12 regressions in total. Each regression has identical form,

$$A = c_0 + \sum_{i=3}^{18} a_i t_i + \sum_{i=3}^{18} b_i t_i^2 + d_1 T_S \qquad (4.17)$$

where A is one of the three atmospheric parameters at one of the frequencies. We use all 10-36 GHz channels in the regressions. The t_i's have the same definitions as in the SST EDR algorithm (equation (4.10)). We also include terms in the regression that are linear and quadratic in SST to

eliminate cross-talk from SST (necessary for obtaining optimal performance from the wind direction search).

The regressions are trained in the same way as the SST and wind speed EDR algorithms, except we add a random deviate (Gaussian distribution, standard deviation of 0.5K) to the truth SST to simulate the SST retrieval error in deriving the regression coefficients. No sensor errors other than effective NEDTs for a 56 x 35 km composite footprint are included in the training.

The channels used in the wind direction algorithm, including the regressions, the NRFs for compositing, and the effective NRFs, CAs and typical effective NEDTs (computed using the method of Section 2.7) are shown in Table 12. In training the regressions or assessing the performance of the algorithm, the effective NRFs are used to convert the single ocean observation NEDT (computed for each ocean scene) to the effective NEDT for the composite TBs (inputs).

Table 12: Compositing and Effective NRFs, Effective Calibration Amplification Factors, and Mean Effective NEDTs for the Wind Direction Algorithm

Channel	NRF	NRF_{eff}	CA_{eff}	Typical $NEDT_{eff}$ (K)
10V	0.260	0.280	1.078	0.197
10H	0.260	0.275	1.058	0.144
10L,R	0.260	0.277	1.064	0.181
18V	0.150	0.167	1.112	0.162
18H	0.150	0.163	1.089	0.138
18P,M	0.150	0.165	1.099	0.150
18L,R	0.150	0.164	1.096	0.172
23V	0.142	0.161	1.134	0.143
23H	0.142	0.158	1.112	0.130
36V	0.142	0.161	1.132	0.091
36H	0.142	0.157	1.106	0.082
36P,M	0.142	0.159	1.118	0.086

The EIA variation is handled in the same way as for SST and wind speed EDR regressions (5 sets of coefficients for each regression, indexed by 36 GHz EIA), giving a total of 60 sets of regression coefficients. In the retrieval, the regression coefficients are again interpolated using the reported EIA for 36 GHz.

4.5.2.3. Wind Speed Regression

The wind vector search (χ^2 minimization routine) discussed in the next section is initialized with a wind speed estimate that is also obtained from regression:

$$W_{est} = c_0 + \sum_{i=3}^{18} a_i t_i + \sum_{i=3}^{18} b_i t_i^2 \quad (4.18)$$

ATBD for CMIS
Ocean EDR Algorithm Suite
Sea Surface Temperature EDR
Sea Surface Wind Speed/Direction EDR
Surface Wind Stress EDR

14-69

The regression and regression training are identical to that for the 20 km wind speed, except that, here, all 10-36 GHz channels are used. The NEDTs used in regression training are, or course, produced using the same effective NRFs as for the atmospheric parameter regressions. Earth incidence angle dependence is handled in the same way as for all other regression algorithms (5 sets of coefficients, indexed to ½ degree increments in the 36 GHz EIA, and interpolated for the retrievals using the reported 36 GHz EIA). Over the entire test dataset, the wind speed estimate has a precision error of about 0.55 m/s, and near zero accuracy error.

Because of the quality of the estimate, W_{est} could serve another purpose. As we saw at the end of Section 3.7.6, the wind direction signal becomes negligible below about 3 m/s. This results in a very flat χ^2 surface (next section), and requires longer for the χ^2 minimization complete, only to find wind direction ambiguities that are essentially random. Therefore W_{est} could be used to decide if the wind speed is too low to execute the wind direction search; if used in this way, we would suggest a W_{est} threshold of 1.0 m/s for executing the wind direction search, which is more than 3.5-sigma below 3 m/s.

4.5.2.4. The Wind Vector Search (χ^2 Minimization)

Sets of wind speed and relative wind direction ambiguities are retrieved by minimizing the cost function:

$$\chi^2\left(W,\varphi_r\right)=\sum_{\alpha=1}^{12}\left[T_{B_\alpha} - F_\alpha\left(W,\varphi_r\right)\right]^2 \qquad (4.19)$$

T_{B_α} denotes the modified Stokes parameter α, as listed in Table 11. F_α is the forward model function for Stokes parameter α, evaluated with T_S equal to the SST retrieval on a circumscribing SST retrieval cell, and the regression values for the atmospheric parameters τ, T_{BU} and T_{BD}.

We use a simple 2-dimensional search in W and φ_r to find the set of wind vector ambiguities. This search is broken down into one dimensional searches, similar to that used for determining the wind vector from scatterometer data. First, we perform a one-dimensional search, for each 2 degree increment in φ_r in the interval 0-360 degrees, to find the value of W which minimizes the χ^2; the resulting values are denoted $W_{min}(\varphi_r)$. This minimization is accomplished using a successive interval partition search (Section 4.5.2.5). The search is initialized with $W=W_{est}$ from equation (4.18) for the first minimization (at $\varphi_r = 0$ deg), but all subsequent minimizations are started with W equal to the value that minimized the χ^2 for the last value of φ_r (i.e. $W_{min}(\varphi_r - 2$ deg)).

The 180 values of φ_r, $W_{min}(\varphi_r)$, and $\chi^2(W_{min}(\varphi_r), \varphi_r)$ are saved in an array. Finally, a simple discrete minimization of $\chi^2\left(W_{min}(\varphi_r),\varphi_r\right)$ along φ_r is performed, the local minima of which form the set of wind vector (ambiguities), usually numbering between 2 and 4. In the very rare event that more than 4 ambiguities are found we restrict ourselves to the first 4. The ambiguities

ATBD for CMIS
Ocean EDR Algorithm Suite
Sea Surface Temperature EDR
Sea Surface Wind Speed/Direction EDR
Surface Wind Stress EDR

14-70

This document is intended for non-commercial use only. All other use is strictly forbidden without prior approval of the U.S. Government.

are then ranked in ascending order of their χ^2, and then stored in an array that is indexed by scan number, scan position and rank.
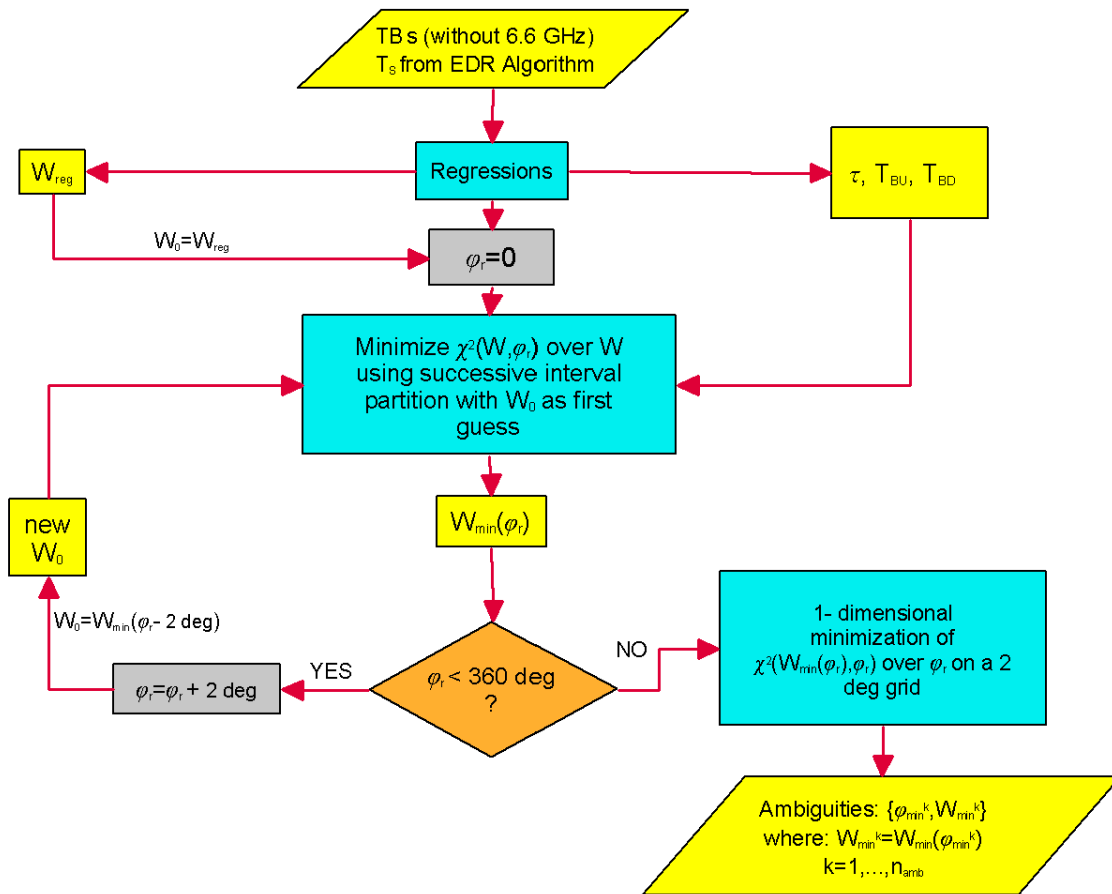
Figure 10: Flowchart diagram of the wind vector retrieval algorithm.

Figure 11 shows a typical example of the 2 dimensional level surface of $\chi^2(W, \varphi_r)$. In this case, there are 3 minima (ambiguities) and the ambiguity closest to the true wind vector (denoted by a *) is the 2nd ranked one.

ATBD for CMIS 14-71
Ocean EDR Algorithm Suite
Sea Surface Temperature EDR
Sea Surface Wind Speed/Direction EDR
Surface Wind Stress EDR

This document is intended for non-commercial use only. All other use is strictly forbidden without prior approval of the U.S. Government.
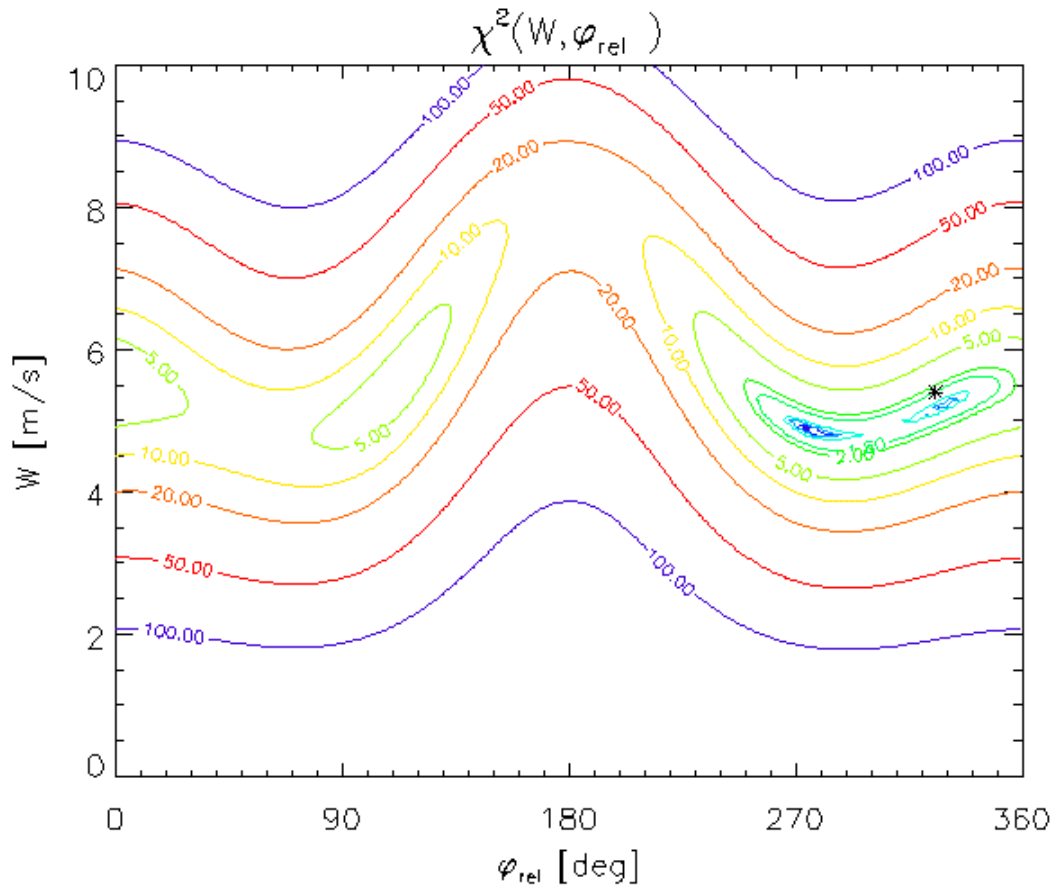
Figure 11: 2 dimensional contour plot for $\chi^2\left(W,\varphi_r\right)$. The & symbol denotes the location of the true minimum.

4.5.2.5.   One-Dimensional Minimization (Successive Interval Partition)

The 1 dimensional minimization of χ^2 along W for each value of φ_r uses an elementary iterative interval partition algorithm. This method needs an initial first guess, W_2, as well as interval boundaries $\left[W_1,W_4\right]$. The initial interval boundaries are $W_1 = 0$ and $W_4 = 26\,m/s$. For the first minimization at $\varphi_r = 0$ deg, we use the value of the regressed wind speed W_{est} from (4.18) as the first guess value.   For all other values of φ_r the result for W_{min} from the last minimization (at $\varphi_r - 2$ deg) is taken as first guess.   No wind direction retrieval is performed if at one value of φ_r the first guess value for W does not lie in the interval $\left[0, 26\,m/s\right]$.

For each value of φ_r, an iteration of the partition algorithm divides the larger of the two intervals $\left[W_1,W_2\right]$ or $\left[W_2,W_4\right]$ into two subintervals, resulting in a new point W_3. It has been shown that fastest convergence is obtained if one uses the golden section ratio for this division (Press, Teukolsky et al. 1992). If, for example $\left[W_2,W_4\right]$ is the larger subinterval, then we choose W_3 so that $\dfrac{W_3 - W_2}{W_4 - W_3} = \dfrac{W_4 - W_3}{W_4 - W_2}$. If $\chi^2\left(W_3,\varphi_r\right) < \chi^2\left(W_2,\varphi_r\right)$, then the interval for the next

iteration is $[W_2, W_4]$ and W_3 is the new intermediate point. If $\chi^2(W_3, \varphi_r) > \chi^2(W_2, \varphi_r)$, then the interval for the next iteration is $[W_1, W_3]$ and W_2 is the new intermediate point. This iteration brackets the true minimum of $\chi^2(W, \varphi_r)$ within the interval $[0, 26\,{}^m\!/_s]$.

This step is repeated until the accuracy $|W_4 - W_1| < 10^{-3}\, \dfrac{|W_4 + W_1|}{2}$ is reached.

4.5.2.6. Median Filter and Ambiguity Removal

In the absence of any further information, the solution that is chosen by the wind vector algorithm is the first ranked wind vector ambiguity. However, the precision for the first ranked ambiguity wind direction is about 41 degrees for wind speed between 3-5 m/s, which is insufficient to meet the wind direction precision requirement of the SRD. On the other hand, the precision error for selecting the closest ambiguity to the true wind direction for each retrieval is less than 20 degrees for the same wind speed range.   There are a variety of "ambiguity removal" algorithms that attempt to select the closest ambiguity to the true wind direction, and the wind direction precision for the closest ambiguity represents a lower bound to the wind direction precision for such algorithms.

To attempt to select the ambiguity closest to the true wind field we pass the ambiguities obtained from the χ^2 minimization through a *circular vector median filter*. This technique is well established in scatterometry (Schultz 1990; Shaffer, Dunbar et al. 1991).   The median filter is an iterative algorithm that operates on the entire set of ambiguities for all pixels in a half orbit. It selects for each pixel the ambiguity that that minimizes the vector distance between the wind vector for that pixel and the vector ambiguity selected for neighboring pixels within a rectangular box.

Because it operates on wind fields, as opposed to individual pixels, all development and testing of the median filter must be done with the NCEP-orbit test datasets discussed in Section 5.5.

Let the kth rank wind vector ambiguity for scan number i and scan position j (pixel i,j) be denoted $\vec{A}_{ij}^k$. The median filter cost function for that ambiguity, E_{ij}^k, has the form:

$$E_{ij}^k = \sum_{\substack{m=i-h \\ m \neq i}}^{m=i+h} \sum_{\substack{n=j-h \\ n \neq j}}^{n=j+h} \frac{1}{f(W_{mn})} \cdot \sqrt{\left(\vec{A}_{ij}^k - \vec{U}_{mn}\right)^2} \qquad (4.20)$$

Note that the window indices $\{m, n\}$ do not include the window center $\{i, j\}$. The index k runs over all ambiguities from 1 to n_{amb}, which is between 2 and 4. $\vec{A}_{ij}^k$ is the wind field which is currently passed through the filter, whereas $\vec{U}_{mn}$ denotes the wind field consisting of ambiguities selected on the last pass, which serves as the filter. The filter is initialized with the first ranked ambiguity from the SOS minimization, i.e. $\vec{U}(\text{start}) = \vec{A}^1$. During each pass the ambiguity $\vec{A}^k$

ATBD for CMIS
Ocean EDR Algorithm Suite
Sea Surface Temperature EDR
Sea Surface Wind Speed/Direction EDR
Surface Wind Stress EDR

14-73

This document is intended for non-commercial use only. All other use is strictly forbidden without prior approval of the U.S. Government.

that minimizes the cost function E^k is the newly selected one. The updating of the filter U to the newly selected ambiguities is done only after all cells have been filtered.

Closest ambiguity means the ambiguity, which is closest to the true wind vector, in the sense that it has smallest distance. *First ranked ambiguity* is the ambiguity with the lowest value of χ^2, i.e. k= 1. *Selected ambiguity* is the ambiguity selected by the MF. The skill rate of a certain type of ambiguity (first ranked or selected) measures how often this type of ambiguity matches the closest ambiguity.

In order to achieve a maximum skill improvement by the MF, the window size h has to be chosen so that areas with high first ranked skill penetrate into the windows for areas with lower first ranked skill. In other words, any "wrong" wind vector must be influenced by a sufficient number of correct wind vectors to be converted into the "correct" (closest ambiguity) wind vector. This means that h is inversely proportional to the grid spacing (i.e. reporting interval).

We have found, that first ranked skill increases noticeably with wind speed and therefore the confidence in vectors with higher wind speed is correspondingly larger. We therefore seek to give a larger weight to the higher wind speed pixels in U in the cost function. Therefore, we have introduced a *skill guidance weight function* $f(W)$, which has the form:

$$f(W) \equiv \left(1 - e^{-\frac{W^2}{a^2}} \right)^p \qquad (4.21)$$

where $a = 7.0 \, m/_s$ and $p = 1$.

The resolution of input the NCEP-wind field (c.f. section 5.5.4) is about 100km. There is no small-scale variability contained in the input wind field. Interpolating the input wind field to the CMIS along scan and along track sampling interval results in very smooth wind fields. This, in turn, could distort the MF results, because the MF performance depends strongly on the special correlation between the wind vectors. If certain meteorological features, such as frontal boundaries, are smoothed too much, the MF will give better results for the test wind fields than it would for a wind field with more realistic small scale variability. On the other hand the MF performance could be degraded in areas of low wind speeds, which have a low first ranked skill; in order to populate the windows in these areas with wind vectors that have a high wind speed (and large first ranked skill) it would be necessary to increase the window size h. However, the running time increases quadratically with h.

The orbit simulator duplicates the CMIS scan geometry. So as to avoid having the MF results overly influenced by the smoothness of the interpolated NCEP wind field, we run the MF on every 4th observation along scan, and every 2nd scan. This corresponds to an interval (grid spacing) of roughly 25 km between observations in both directions.

We have obtained best skill by running the MF with a window size of $h = 5$ for every 2nd scan and for every 4th cell provided by the NCEP-orbit test data set (sections 5.3 and 5.5.4). We have tested the dependence of the skill rate with window size h keeping the grid spacing fixed as

above, and found a larger skill rate with a window size of $h = 5$ than for $h = 3$. Increasing the window size beyond 5 did not improve the skill noticeably.

The performance test examples (section 6) were all run with a window size of $h = 5$, the skill guidance weight function $f(W)$ (4.21) and using every 2nd scan and every 4th cell. It is difficult to say what the optimum choice for h and the grid spacing would be if the MF was run on realistic wind fields. Clearly, the grid spacing should not be more than the horizontal reporting interval (20 km), which confines us to using every scan. The crucial parameter is the spatial variability of the true wind fields. There are, of course, technical limitations, because the running time for the MF increases quadratically with h and grows linearly with the number of grid points used. In scatterometry, window sizes between 5 and 7 and grid resolutions between 25 km and 50 km are very common for MF (Shaffer, Dunbar et al. 1991).

We terminate the median filter algorithm as soon as the relative difference in the minimum cost function E, summed up over all cells, between pass $N-1$ and pass N reaches a threshold $\varepsilon = 10^{-3}$:

$$\frac{\left| \sum_{ij} E_{ij}^{k_{min}(N)} - \sum_{ij} E_{ij}^{k_{min}(N-1)} \right|}{\sum_{ij} E_{ij}^{k_{min}(N-1)}} < \varepsilon \qquad (4.22)$$

Figure 12 shows a flowchart for the MF algorithm.
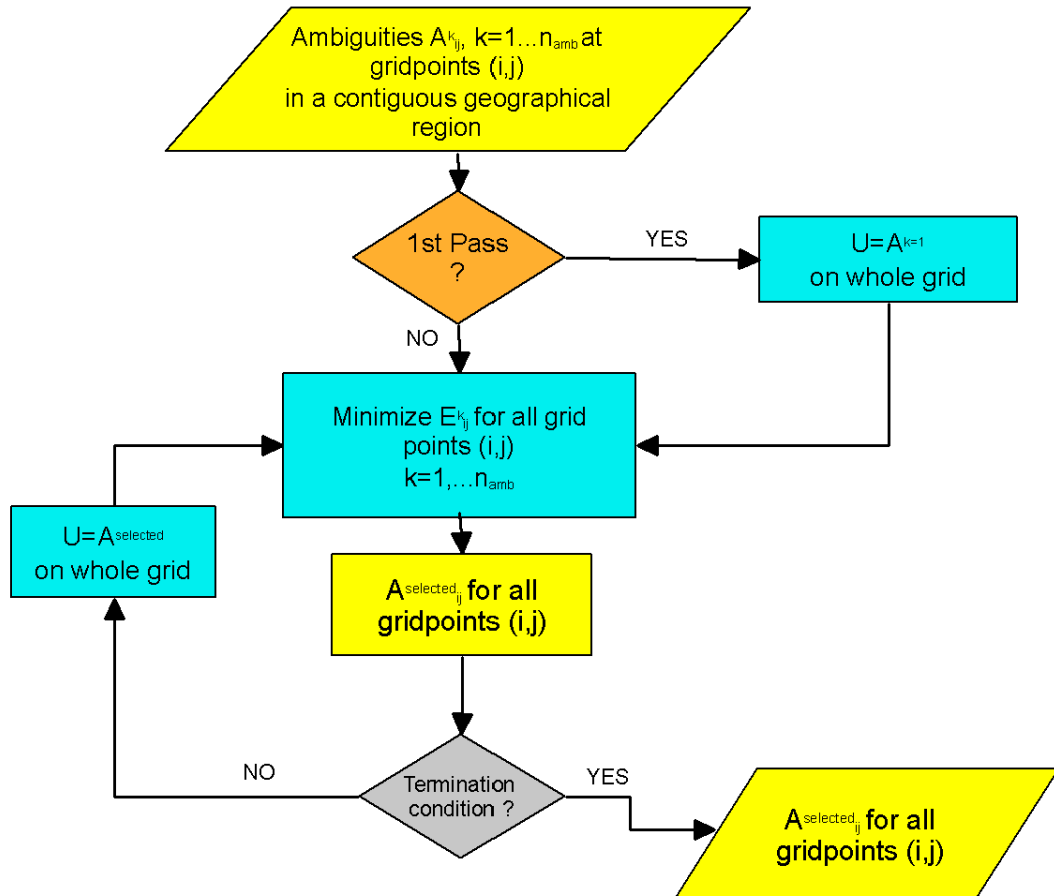
Figure 12: Flowchart Diagram for the MF.

4.6. Wind Stress

4.6.1. Physical Basis

Wind transfer momentum to the ocean surface, creating waves and wind-drift currents. When the fetch is large, one can find wind stress as a function of wind speed; this is called the bulk formulation for wind stress. The connection between wind speed and stress is the coefficient of drag. Our wind speed algorithms actually measure surface roughness; therefore wind speed is the inferred product and wind stress is actually being measured.

Our RTM is based upon neutral stability wind speed at 10 m height; that is all wind speeds used in Section 3 are neutral stability wind speeds at 10 m height. Any algorithm trained or based on our RTM, such as our wind speed and wind vector EDR algorithms, therefore retrieves neutral stability wind speed at 10 m. Thus the coefficient of drag used to determine wind stress should be that for neutral stability, 10 m winds.

4.6.2. Mathematical Description of Algorithm

The algorithm uses a bulk formation for wind stress using the 20 km wind speed EDR retrieval. We use a lookup table on the neutral stability coefficient of drag at 10m height (C_{DN10}) to interpolate it to the retrieved wind speed. The lookup table has been determined using an iterative algorithm based on parameters and equations in (Smith 1988; Liu and Tang 1996). The computation for each wind speed W begins with a first guess roughness length of $z_0=1.2 \times 10^{-4}$m, and the following 4 equations are iterated until C_{DN10} converges to 1 part in 10^5:

$$C_{DN10} = \frac{k^2}{\ln^2\left(\frac{10}{z_0}\right)} \quad (4.23)$$

$$\tau = \rho_{air} C_{DN10} W_{N10}^2 \quad (4.24)$$

$$u_* = \left(\frac{\tau}{\rho_{air}}\right)^{\frac{1}{2}} \quad (4.25)$$

$$z_0 = \frac{0.11\upsilon}{u_*} + \frac{au_*}{g} \quad (4.26)$$

k is the von Karman constant (0.40), υ is the dynamic viscosity of air (1.5×10^{-5} ms^{-1}), a=0.011, g is the gravitational field at the surface (9.8ms^{-2}), and ρ_{air} is the density of air (1.292 kgm^{-3}).
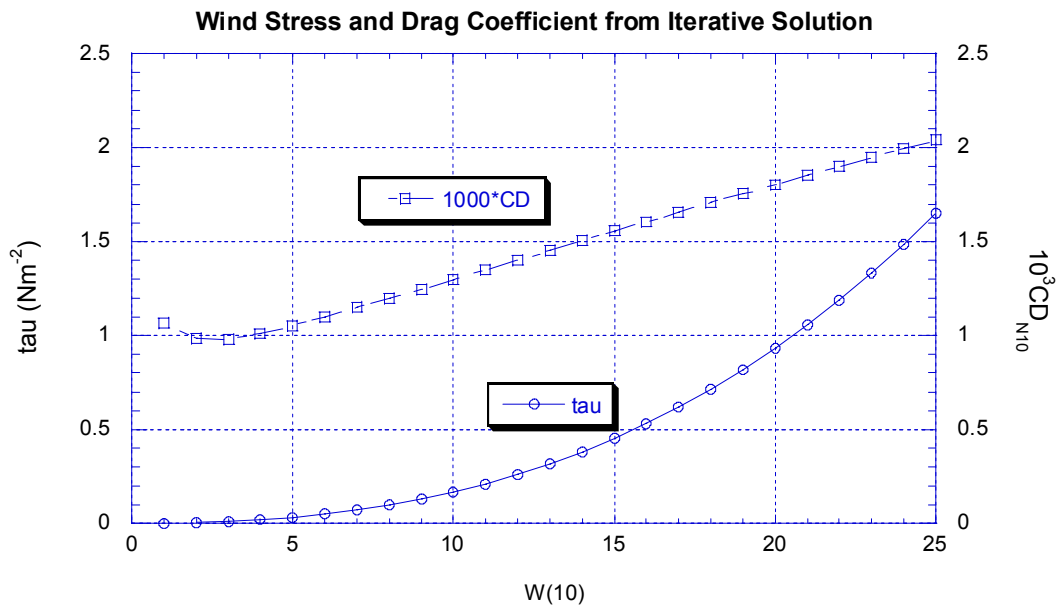
Figure 13: Wind Stress and Coefficient of Drag for 10m Neutral Stability Winds

ATBD for CMIS   14-77   This document is intended for non-commercial
Ocean EDR Algorithm Suite   use only. All other use is strictly forbidden without
Sea Surface Temperature EDR   prior approval of the U.S. Government.
Sea Surface Wind Speed/Direction EDR
Surface Wind Stress EDR

The C_{DN10} obtained from the iterative computation, shown in Figure 13, correctly models the upturn in the coefficient of drag toward low wind speeds, and is in agreement with the C_{DN10} that can be obtained from (Smith 1988). Also shown in the plot is the wind stress computed from the coefficient of drag using equation (4.24), which also constitutes the
equation for the algorithm. It is clear than the range of wind stress for neutral stability winds ranging from 0 to 25 m/s is 0 to 1.65 Nm^{-2}.

Given the wind stress values above, we could interpolate wind stress directly given the wind speed. However, given the curvature in the wind stress curve, it is slightly more accurate to interpolate the coefficient of drag and then apply equation (4.24).

4.6.3. Data Needed by the Algorithm

The data needed by the algorithm is the retrieved 20 km wind speed EDR for the retrieval cell. No other CMIS or external data is needed.

ATBD for CMIS
Ocean EDR Algorithm Suite
Sea Surface Temperature EDR
Sea Surface Wind Speed/Direction EDR
Surface Wind Stress EDR

14-78

This document is intended for non-commercial use only. All other use is strictly forbidden without prior approval of the U.S. Government.

5. TB Data Sets for Algorithm Training and Testing

5.1. Introduction

A crucial part in developing and testing the EDR algorithms is the simulation of TB data sets. The data sets are used for deriving the regression coefficients (Section 4), assessing EDR retrieval performance and algorithm optimization (Section 6), and deriving requirements for sensor errors and knowledge errors for environmental conditions (Cross Polarization Correction Section of TDR/SDR Algorithm ATBD). The data sets are derived using the forward RTM (Section 3), and truth geophysical data from the sources described in this section.

Section 5.2 details the method of using the forward RTM, and the truth data required, to simulate the TB data sets. Section 5.3 makes the distinction between the spatially uncorrelated truth data used for training and testing the EDR algorithms ("radiosonde" data sets) and the spatially correlated data that is used for testing the ambiguity removal post-processing for the wind direction EDR (NCEP-Orbit datasets). The datasets are named by the source of truth data for atmospheric profiles used to generate the dataset.

Section 5.4 covers the radiosonde datasets. The distinction between algorithm training and data sets is made based on the differing requirements for the distributions of the geophysical parameters and the correlations between them. For the wind EDRs, it is important that all wind speeds be represented sufficiently to allow high confidence in the EDR error statistics at any wind speed. However, it is shown that realistic assessment of SST EDR performance requires that the wind speed distribution in the test data set approximate the natural distribution.

Section 5.5 discusses the geographically based data sets that are used in testing the median filter. Here, an orbit simulator is used to obtain geophysical truth data from NCEP fields of atmospheric profiles, SST and wind vectors.

5.2. RTM and Truth Data for Training and Test Data Sets

The forward RTM of Section 3 is used to simulate the brightness temperatures for all training and test data sets. This allows the RTM to be split into two components, one that computes the atmospheric parameters T_{BU}, T_{BD}, and τ from atmospheric profiles, and one that uses the atmospheric parameters along with values for the surface parameters to compute the T_B's.

The parameters required by the forward RTM are:

1) Sea surface temperature (SST), T_S .
2) Wind speed, W (neutral stability, 10m above the ocean surface).
3) The wind direction relative to the radiometer look direction, φ_r
4) The atmospheric temperature profile, $T(h)$.
5) The atmospheric air pressure profile, $p(h)$.

ATBD for CMIS
Ocean EDR Algorithm Suite
Sea Surface Temperature EDR
Sea Surface Wind Speed/Direction EDR
Surface Wind Stress EDR

14-79

This document is intended for non-commercial use only. All other use is strictly forbidden without prior approval of the U.S. Government.

6) The atmospheric profile for water vapor pressure, $p_V(h)$ (or, equivalently, the water vapor density, $\rho_V(h)$, or the relative humidity, $RH(h)$).

7) The atmospheric profile of liquid cloud water density $\rho_L(z)$.

The forward RTM is conveniently split into two parts, an atmospheric component which computes the transmission coefficient, upward and downward welling radiation, and a surface component which computes the total emissivity and scattering term for the ocean surface. Then, the atmospheric and surface parameters are used together to simulate the brightness temperatures.

5.2.1. The RTM for the Atmosphere

The atmospheric portion of the RTM consists of the computation of the parameters T_{BU}, T_{BD}, and τ from the atmospheric profiles of temperature, pressure, water vapor and cloud liquid water. A top-level description is given by equations (3.19) through (3.24).

5.2.2. Surface Portion of RTM

The surface portion of the RTM code computes the total emissivity, reflectivity, and scattering coefficient for all 6 polarizations. We outline the procedure, as follows:

The specular sea surface reflectivity is computed using the equations of Section 3.4 for the vertical and horizontal polarizations. The wind driven isotropic portion of the reflectivity for the same polarizations is then computed using equations (3.46), and (3.56) through (3.61). The isotropic emissivities are then computed as one minus the isotropic reflectivities, and the wind direction components of emissivity ΔE^V and ΔE^H, as found from equations (3.71) and (3.72), are added to obtain the total emissivity for the vertical and horizontal polarizations; these are then used with equations (3.71) and (3.76) to compute the total emissivity for the P, M, L, and R polarizations.   The total reflectivity for each polarization is then computed as one minus the total emissivity.

The vertical and horizontal polarized scattering coefficient for downwelling radiation are computed according to equations (3.54), (3.55), (3.63) and (3.64); this requires knowing the atmospheric transmission from the atmospheric component of the RTM (which is why it is run first). Then the total reflectivities and the scattering coefficients for the vertical and horizontal polarizations are used to compute the scattering coefficient for the P, M, L, and R polarizations via equation (3.78).

Finally, equations (3.11), (3.29) and (3.62) (already combined as equation (4.12)) are used to compute the top-of the atmosphere brightness temperatures using the total emissivity and the scattering term for each polarization, and the atmospheric parameters T_{BU}, T_{BD}, and τ. All 6 polarizations are simulated at each 6-36 GHz frequency, to allow for channel trade studies using the EDR algorithms.

ATBD for CMIS
Ocean EDR Algorithm Suite
Sea Surface Temperature EDR
Sea Surface Wind Speed/Direction EDR
Surface Wind Stress EDR

14-80

This document is intended for non-commercial use only. All other use is strictly forbidden without prior approval of the U.S. Government.

5.3. Spatially-Correlated (NCEP-Orbit) vs Non-Correlated (Radiosonde) Data Sets

For both training and testing all EDR algorithms other than the Median Filter wind direction post-processing, the spatial correlations of geophysical parameters in the test data are not important. The geophysical data can be Monte Carloed from pixel to pixel, without concern that the data from one pixel to the next is completely uncorrelated. Instead, the emphasis is placed on the distributions of the geophysical parameters in the training and test datasets; that the distributions cover the required measurement ranges of the parameters, and that all physically allowable combinations of geophysical parameters are well-represented. Data sets generated in this way are called radiosonde data sets.

However, the median filter algorithm operates on wind fields, i.e. requires as input the wind vector ambiguities for all pixels on a contiguous area of ocean, on a grid matching the CMIS scan geometry. Realistic testing of the algorithm requires that the spatial correlation in the truth wind fields be on a scale of roughly that found in nature. The simplest way to achieve these requirements is to sample the geophysical fields of a global circulation model (GCM) in a way that mimics the CMIS scan geometry, and use the resulting geophysical fields as the truth data in simulating the TBs for wind direction/median filter retrieval. We chose the NCEP GCM as the source of the truth data, as it contains fields of all the parameters necessary to simulate TBs except cloud liquid water. An orbit simulator was developed for extracting the NCEP truth data on a grid matching the CMIS scan geometry. Thus, training and test data sets simulated from truth data acquired this way are called NCEP-Orbit data sets.

5.4. Radiosonde Data Sets

5.4.1. Structure of the Radiosonde Data Sets

The radiosonde data sets derive their name from the fact that a set of 42,195 quality controlled radiosonde observations are used to derive the profiles of temperature, pressure, and water vapor that are used in the atmospheric component of the RTM. This set of profiles, along with the simulated cloud profiles discussed below, provides the basis for simulating all radiosonde data sets. All surface parameters needed to compute the brightness temperatures are Monte Carloed. The training and test data sets differ only in the distributions of the wind speed, and the filtering for unphysical combinations of surface and atmospheric parameters.

To the temperature and water profiles derived from each radiosonde observation, we attach 7 different cloud profiles, gradually increasing the liquid water density from one to the next while varying cloud base and top height randomly; while the cloud density is stepped through the same 7 values, the columnar cloud liquid water values are different for each radiosonde observation. This gives a large number of simulated atmospheres, from which we compute T_{BU}, T_{BD} and τ from the atmospheric part of the RTM. To each simulated cloud profile, we attach 20 simulated ocean surfaces (different for each cloud model and radiosonde observation), each consisting of a Monte Carloed SST, wind speed, and wind direction. Thus, 140 different simulated ocean-atmosphere scenes are generated for each radiosonde observation.

ATBD for CMIS   14-81   This document is intended for non-commercial
Ocean EDR Algorithm Suite   use only. All other use is strictly forbidden without
Sea Surface Temperature EDR   prior approval of the U.S. Government.
Sea Surface Wind Speed/Direction EDR
Surface Wind Stress EDR

For each simulated ocean-atmosphere scene, the forward RTM is used to simulate TBs of all 6 polarizations for all frequencies between 6-36 GHz. This ensures that the development, testing, and comparison of algorithms using different polarimetric channel configurations can be achieved with a single set of test and training datasets (i.e. without simulating additional polarizations).

5.4.2. Truth Data for Atmospheric Temperature and Water Vapor Profiles

The atmospheric profiles of temperature and water vapor are derived from 42,195 quality controlled radiosonde flights launched from over small islands in the 1987-1990 time period. The quality control procedures are described and the locations of the island radiosonde stations are given in (Wentz 1997). To specify the water vapor density, we used the expression for ρ_v given in (Liebe 1985) as a function of the air and dew point temperatures. The altitude h is found from the standard hydrostatic equations that give geopotential height as an integral of temperature and pressure (Peixoto and Oort 1992).

We use the Reynolds monthly SST to specify the SST offshore from the radiosonde site. This "site SST" is used later in simulating the ocean scenes.

5.4.3. Simulated Cloud Scene Truth Data

The atmospheric part of the RTM requires the cloud liquid water profile in addition to the radiosonde profiles to determine the atmospheric parameters T_{BU}, T_{BD} and τ. Therefore, for each pair of water vapor and temperature profiles, we simulate7 cloud profiles (cloud models). The cloud water densities for the seven cloud models range from 0.0 to 0.6 gm^{-3}, with slight emphasis on the lower densities. For each cloud model, we Monte Carlo a cloud base height as a random deviate between 500 and 2000 m, and a cloud top height as the cloud base height plus a random deviate between 500 and 2500 m. Both random deviates are taken from a uniform (boxcar) distribution.

5.4.4. Simulated Ocean Surface Truth Data

To each randomly generated cloud profile, we attach 20 randomly generated ocean surface models that consist of a Monte Carloed SST, wind speed and wind direction. The 20 surface models are different for each cloud model-radiosonde combination.

There is a strong correlation between SST and columnar water vapor (V) in nature. We could have incorporated the extent of this correlation into the radiosonde data sets by using the site SST as the SST for each simulated surface. However, this correlation can lead regression algorithm developers astray; for example, it generally results in an SST algorithm that influenced not just by the SST signal in the T_B's , but also water vapor signal. Such algorithms perform poorly when confronted with cases where the water vapor does not follow the usual correlation with SST. But, these are precisely the interesting cases—fronts and other disturbances—where the SST retrievals are most valuable.

ATBD for CMIS   14-82   This document is intended for non-commercial
Ocean EDR Algorithm Suite   use only. All other use is strictly forbidden without
Sea Surface Temperature EDR   prior approval of the U.S. Government.
Sea Surface Wind Speed/Direction EDR
Surface Wind Stress EDR

Therefore, we find it worthwhile to reduce the correlation of SST and V in the training data sets, so that the interesting cases are well represented in the training data. While this results in a slight overall increase in the modeling error of the regressions, the resulting algorithms are well suited to handling these cases. We reduce the correlation of SST and V in test data sets as well, so that we can verify that good performance is obtained for the same cases.

To reduce the correlation between SST and V, we Monte Carlo the truth SST as the site SST plus a uniform random deviate over a specified interval. In previous algorithm development work, we have used an interval of [-10,10] C. The size of the interval for our CMIS data sets is dictated by the fact that the highest site SST in the radiosonde data is 29 C, whereas the required measurement range for the SST algorithm is up to 40 C. Therefore we use an interval of [-11,11] C for our CMIS data sets, and choose a new deviate if the resulting SST is below –2 or above 40 C. Use of either interval results in some unphysical ocean-atmosphere scenes, which are filtered out of the data sets, as discussed in section 5.4.7.

For each surface model, we also Monte Carlo a wind speed and relative wind direction. The wind direction is chosen as a uniform random deviate on the interval $[0, 360]$ deg. However, the distribution from which the wind speed is chosen depends on the purpose of the dataset.

5.4.5. Wind Speed Distribution for Training Data Sets

A regression algorithm tends to perform optimally only over the range and combinations of geophysical parameters that are well represented in the training data. We desire EDR algorithms that work optimally over the range of wind speeds from 0 to 25 m/s. Therefore, we Monte Carlo the wind speed for the radiosonde training data as a uniformly distributed random deviate in the range [0,25] m/s.

5.4.6. Wind Speed Distribution for Test Data Sets

5.4.6.1. Test Data Set for Wind EDRs

The SDR requirements for the wind EDRs must be fulfilled over a range of wind speeds extending to 25 m/s. To obtain the most reliable wind EDR error statistics over the required range of wind speeds, it is important that all wind speeds in this range be adequately represented in the test data set. Therefore we Monte Carlo the wind speed as a uniform random deviate on the interval [0,25] m/s. The lower end of this range was chosen as zero, because we want to provide error statistics showing that both the (20 km) wind speed EDR and low resolution wind speed meet or exceed all required EDR error thresholds from 0 to 3 m/s as well.

5.4.6.2. Test Data Set for SST

However, the assessing SST algorithm performance presents a different requirement on the wind speed distribution. The bulk of the SST signature is contained the ET_S term in equation (3.11), which serves as the basis for the retrieval algorithm. However, the emissivity includes the directional component as defined by equation (3.71), leading to cross-talk from wind direction. The cross-talk, which manifests as a wind direction dependent bias in the SST

ATBD for CMIS
Ocean EDR Algorithm Suite
Sea Surface Temperature EDR
Sea Surface Wind Speed/Direction EDR
Surface Wind Stress EDR

14-83

This document is intended for non-commercial use only. All other use is strictly forbidden without prior approval of the U.S. Government.

retrievals, becomes part of the uncertainty error for each SST bin in the SST performance statistics (because each SST bin contains all wind directions). This cross-talk is a problem for the SST retrieval at high winds; as the amplitude of the wind direction emissivity signal grows with wind speed (Figure 4), so does the amplitude of the cross talk and the SST uncertainty statistics. Our TMI experience has shown that wind direction cross-talk into SST can be up to several K at the highest wind speeds.

Over-emphasizing the high wind speeds in the test data set for the SST algorithm would therefore inflate the SST uncertainty errors beyond what is expected for a natural distribution of wind speeds. To solve this problem, we develop a special test data set that mimics the actual distribution of wind speeds as closely as possible, including variations in the distribution with respect to SST.

5.4.6.3. Rayleigh Distribution of Wind Speeds

The global distribution of wind speeds approximately follows a Rayleigh (or Weibull) distribution, with PDF:

$$p(W)dW = \frac{1}{\delta^2} e^{-\frac{W^2}{2\delta^2}} W \, dW \qquad (5.1)$$

This distribution can be obtained by assuming that the two Cartesian components of the wind vector winds are independent and follow Gaussian PDF's with identical widths and zero mean.

The PDF peaks at $W_{max} = \delta$ and has a mean of

$$\langle W \rangle = \delta \sqrt{\pi/2} = 1.2533\,\delta \quad (5.2)$$

and a standard deviation

$$\sigma_W = \delta \sqrt{2 - \pi/2} = 0.655\delta \qquad (5.3)$$

The best-fit Rayleigh distribution for the NCEP/NCAR Reanalysis (Kalnay, Kanamitsu et al. 1996) ocean surface winds has $\langle W \rangle = 7.0\,m/s$ (Meissner, Smith et al. 2001).

Using a Rayleigh distribution of wind speeds in the radiosonde test data improves the overall SST performance by a few times 0.01K. However, there remained an excess upward slope in the SST precision vs SST curve when compared to retrievals using the NCEP test data sets and to the Wentz TMI SST retrievals. Investigation showed that the slope difference is attributable in part to the NCEP and TMI wind speed distributions being correlated with SST. That is, <W> and σ_W first increase at low SST, then drop rapidly at higher SSTs. This is shown in Figure 14 for the NCEP data used in the NCEP-Orbit data sets discussed in Section 5.4. The physical explanation is that wind speed constrains the SST, because heat loss from the surface due to evaporation and heat transfer increases with wind speed.

ATBD for CMIS
Ocean EDR Algorithm Suite
Sea Surface Temperature EDR
Sea Surface Wind Speed/Direction EDR
Surface Wind Stress EDR

14-84

This document is intended for non-commercial use only. All other use is strictly forbidden without prior approval of the U.S. Government.
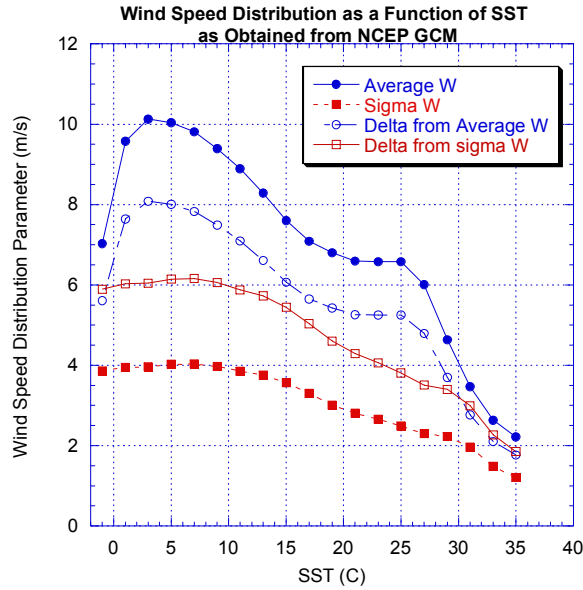
Figure 14: NCEP Wind Speed Distribution Parameters as a Function of SST

The objective is produce and SST data set where the wind speed distribution matches the natural distribution as a function of SST, i.e. the parameters of Figure 14, while maintaining the overall Rayleigh distribution as much as possible. To do this we compute a δ for each SST bin using the data in the figure; then, in generating the wind speed for each simulated surface, we first Monte Carlo an SST, and then Monte Carlo a wind speed from a Rayleigh distribution using the δ appropriate to the SST.

The limitation to this technique is that the wind speeds for individual SST bins may not be Rayleigh distributed. An indication of this is the difference between the δ's computed from the average and standard deviation W (i.e. by inverting (5.2) and (5.3)) for the intermediate SST bins, as shown in Figure 14. Using the average of the two δ's for each bin in Monte Carloing the wind speeds results in a low estimate of δ for most bins; this gives an overall distribution with too many low wind speeds compared to the <W>=7.0 m/s Rayleigh distribution. Using the δ's derived from the average wind speeds results in far too many high wind speeds. The best compromise seems to be finding the scaling factor that best fits the lower δ curve to the upper on in Figure 14, and then taking the average of the scaled lower curve and the upper curve. For the highest two SST bins, where no NCEP data is available, we continue the δ curve by successively reducing the slope, so as not to underestimate δ at the largest SSTs. The resulting δ curve, compared to the upper NCEP δ curve (repeated from Figure 14) is shown in the left panel of Figure 15.

5.4.6.4. Final Wind Speed Distribution for SST Test Data Set

The resulting wind speed distribution (after filtering—see next section) is shown in Figure 15. This is the wind speed distribution for the SST test data set. Also shown is the best fitting Rayleigh distribution (the difference in the location of the maxima is mainly due to binning of the test data set wind speeds in 2 m/s increments). Both distributions have a mean W of 6.60 m/s, close the global value for all NCEP data (Figure 14 and the δ's were computed from only the NCEP-Orbit test data of Section 5.5.)
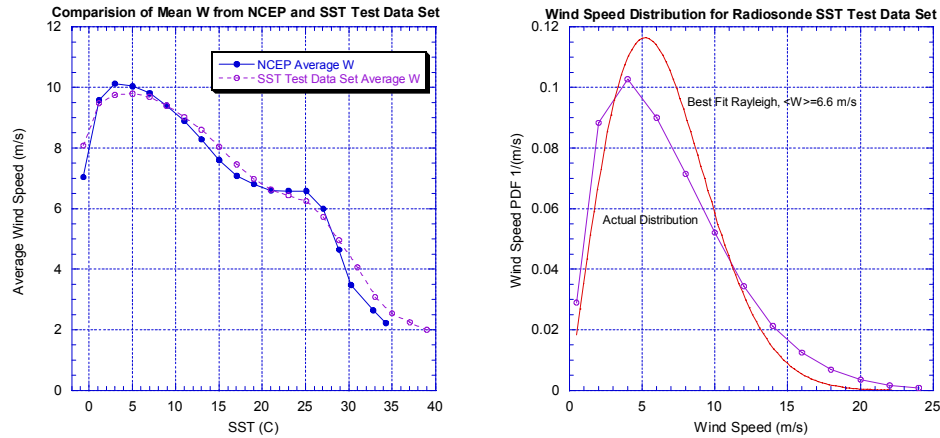
Figure 15: Wind Speed Distribution for the SST Test Data Set Compared to Best Fit Rayleigh Distribution

The excess of low wind speeds compared to the best fit Rayleigh distribution is caused by the addition of the low δ Rayleigh distributions for the two highest SST bins (not contained in the NCEP data). The under-representation of moderate (4-10 m/s) wind speeds is caused by this and the over-representation of high wind speeds, due to the using high δ Rayleigh distributions for low SSTs. But, given that the overall mean wind speed for the distribution is close to that found in nature, and the overall distribution approximates a Rayleigh distribution this data set is suitable for testing the SST algorithm performance.

5.4.7. Geophysical Filtering for Radiosonde Data Sets

5.4.7.1. SST-Water Vapor Filtering

While reducing the correlation between SST and V in the data sets is desirable, it also results in some rather unphysical ocean atmosphere scenes.

We have obtained the relationship between SST and V by regressing the site SST against V derived from the radiosonde observations:

$$T_{S0}(V) = 273.16 + 0.8337V - 3.029 \times 10^{-5} V^{3.33} \quad V \le 48mm$$
$$T_{S0}(V) = 301.16 \quad V > 48mm$$

$$(5.4)$$

ATBD for CMIS
Ocean EDR Algorithm Suite
Sea Surface Temperature EDR
Sea Surface Wind Speed/Direction EDR
Surface Wind Stress EDR

14-86

This document is intended for non-commercial use only. All other use is strictly forbidden without prior approval of the U.S. Government.

The rms error in this relationship is approximately 3K over the entire range of V. Therefore, in the *test* datasets for previous radiometers, we have traditionally rejected simulated ocean-atmosphere scenes for which $|T_S-T_{S0}(V)|>\Delta T_S$, with ΔT_S set at 10K (more than 3 sigma); the remaining scenes included more than 99% of the combinations of SST and V found in nature. However, as a result of the distribution of the site-SSTs, the traditional filter provides a maximum truth SST of 39 C, and SSTs higher than 37 C would not be represented with enough frequency to provide accurate performance and stratification statistics. In order to obtain SSTs as high as 40 C with a frequency sufficient to obtain reliable EDR performance statistics, we find it necessary to widen the filter to $\Delta T_S = 13$ K. While exceptionally rare in nature, the newly included cases of highly decorrelated SST and V tend to degrade overall EDR algorithm performance metrics by a few percent, and are responsible for the remaining upward slope in the SST precision curve of section 6.2.3.

So that the regressions perform well under all circumstances, we decorrelate SST and V in the *training* datasets as much as possible without introducing significant overall modeling error into the regressions (modeling error is the result of the finite ability of the regression to model the geophysical parameter given the variation of the other geophysical parameters). The SST and all W regressions can be derived over a large range of ΔT_S without excessive modeling error; so, for training the W and SST regressions, a ΔT_S of 40 K is used, which essentially includes all simulated observations. But the overall modeling error of the atmospheric regressions rises rapidly as ΔT_S grows beyond the natural limit of 10 K in the training data sets. However, we find it necessary to train the atmospheric regressions over the same range of ΔT_S that we use in the test data sets (13 K) in order to avoid a much larger modeling error in the regressions for cases where ΔT_S is between 10 and 13K.

5.4.7.2. Cloud Liquid Water Filtering

The Monte Carlo for cloud liquid water profiles results in a range of columnar liquid water that extends far beyond the limit for which light rain is expected. Let R be the rain rate (mm/hr) averaged over the rain column H (km). (Wentz and Spencer 1998) show that the typical value of cloud liquid water associated with R is

$$L[mm] = 0.18(1+\sqrt{HR})\quad (5.5)$$

For very light rain (0.1 mm/hr), the rain drops are small enough that they Rayleigh scatter radiation. As the rain rate increases, the drops become large enough that the Mie scattering mechanism begins to dominate, and the emission-absorption approximation used in the CMIS RTM breaks down. As a result, our TMI SST and wind speed retrieval algorithms (derived from a similar RTM) show significantly degraded rms errors in the 0.1 to 0.5mm/hr region (discussed under degraded conditions), and unacceptably large errors for rain rates above 0.5mm.

The rain column varies greatly between non-tropical and tropical locations, with a maximum column height in the tropical regions (corresponding to a maximum of L in equation (5.5)). There is some debate as to whether the rain column extends to the freezing level in the tropics, in which case the column could reach 5 km, or extends only to 3 km (Wentz and Spencer 1998). In

ATBD for CMIS
Ocean EDR Algorithm Suite
Sea Surface Temperature EDR
Sea Surface Wind Speed/Direction EDR
Surface Wind Stress EDR

14-87

This document is intended for non-commercial use only. All other use is strictly forbidden without prior approval of the U.S. Government.

the following table we use equation (5.5), to determine the maximum CLW that can be associated with rain rates of 0.1 and 0.5 mm/hr for the two maximum column heights.

H (km)	R= 0.1mm/hr	R=0.5 mm/hr
3	0.28 mm	0.40 mm
5	0.31 mm	0.46 mm

Table 13: Maximum Cloud Liquid Water Associated with Rain Rates of 0.1 and 0.5 mm/hr.

Therefore, the rain rate becomes sufficient to degrade EDR performance starting at about L=0.3mm, and to corrupt the retrievals somewhere between L=0.4 and 0.46 mm. Since we do not simulate rain in the TB datasets, it is not possible to show this degradation, and retrievals for L greater than 0.3mm will give overly optimistic results. Therefore, we filter all simulated observations for which L exceeds 0.3mm from the test datasets when assessing the performance versus the SRD requirements in Chapter 6. Since the RTM dictates that retrieval algorithms can only be generated for cases of no or very light rain (R<0.1 mm/hr), we filter the training data sets in the same way.

In practice, all filtering of the data sets takes place during training of the regressions and testing of the EDR algorithms and not during the simulation of the radiosonde datasets; this allowed us to experiment with various values of the ΔT_S and L cutoffs to attain the desired SST measurement range, and assess the performance of the algorithms for various ranges of L.

5.4.8. Filtered Distributions of Geophysical Truth Data in Radiosonde Data Sets

PDFs for the radiosonde test data set used for the wind EDRs are shown in Figure 16. The plots show the results after filtering the observations, as described in the last section, using a L cutoff of 0.3mm and a ΔT_S of 13K. The only difference between the distributions in the wind EDR and SST test data sets is that the wind speed distribution of the later is given in Figure 15.

The training data sets all have a uniform distribution of wind speeds. The only difference is in the filtering of the observations. For training the regressions for the atmospheric parameters, the filtering is identical to that for the test data sets; the resulting distributions of the geophysical parameters are identical to Figure 16. However, for training the SST and wind speed regressions, the filtering uses the same L cutoff, but the ΔT_S cutoff is 40 K, i.e. practically no filtering for unphysical combinations of SST and V. This has the effect of including more ocean scenes with very high and low SST or V (i.e. widens these distributions slightly). All other distributions remain the same as in Figure 16.

ATBD for CMIS
Ocean EDR Algorithm Suite
Sea Surface Temperature EDR
Sea Surface Wind Speed/Direction EDR
Surface Wind Stress EDR

14-88
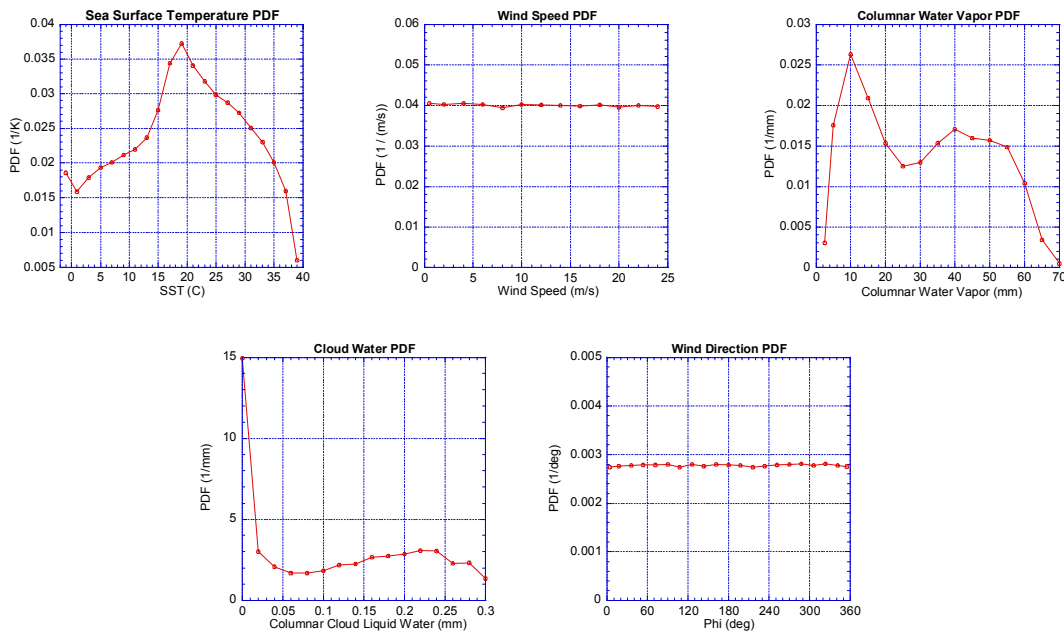
Figure 16: Distributions of Geophysical Parameters in Wind EDR Test Data Sets. (Wind speed distribution for SST Test Data Set shown in Figure 15.)

5.5. NCEP-Orbit Data Sets

5.5.1. Purpose of NCEP-Orbit Data Sets

The purpose of the NCEP-orbit data sets is ostensibly to test the median filter (MF) wind direction ambiguity removal algorithm. Since the MF algorithm depends on the relationship between the retrieved wind vector in a given observation and those for neighboring observations in the scan based grid, realistic testing requires that the TBs be simulated using wind fields that approximate the natural spatial variability of the wind vector.

However, having just realistic wind fields is not sufficient. If we Monte Carlo the other geophysical parameters that are necessary to simulate the TBs, then the wind direction ambiguities that are retrieved from neighboring observations will be biased in different ways that do not correspond to how they would be biased if the fields of the other geophysical parameters were varied realistically. Therefore, another requirement for realistic testing is that all the fields of geophysical parameters follow the natural spatial variation. At the same time, it is important that the geophysical fields include as many combinations as possible of meteorological and oceanographical conditions that exist naturally. The geophysical fields must also have global coverage, so that they can be sampled over any ocean.

The best way to ensure that all these criteria are met is to obtain all the geophysical parameters we can from a general circulation model (GCM) and sample them in a way that mimics the CMIS scan geometry. For the GCM, we use the real time final analysis (FNL) of the

ATBD for CMIS
Ocean EDR Algorithm Suite
Sea Surface Temperature EDR
Sea Surface Wind Speed/Direction EDR
Surface Wind Stress EDR

14-89

This document is intended for non-commercial use only. All other use is strictly forbidden without prior approval of the U.S. Government.

General Data Assimilation System (GDAS), which is run by the National Centers of Environmental Prediction (NCEP). Fields of SST, wind vectors, and atmospheric profiles are obtained from the NCEP data; only cloud liquid water must be obtained from another source.

5.5.2. Limitations of NCEP-Orbit Data Sets

Because the NCEP geophysical fields represent realistic yet smoothed meteorological and oceanographical conditions, the natural range of the geophysical parameters (in specific, the required ranges for the EDRs) are not completely covered. The NCEP-Orbit data sets contain very few SSTs above 30 C or wind speeds above 18 m/s. Furthermore the NCEP-Orbit data sets do not contain any profiles for cloud liquid water.

5.5.3. Orbit Simulator

The first step is to create CMIS orbits that provide time and geo-location of all CMIS observations over the world oceans. The computation of observation time and geo-location has been described in (Wentz 1990) for the SSM/I instrument. We have used the same routines but substituted the scan geometry and nominal altitude for CMIS.

The orbit simulation renders a set of space-time coordinates (t, x_{lat}, x_{lon}) as well as a value for the EIA for each frequency and the looking azimuth φ_i for each CMIS observation. The values extracted from NCEP are those for the antenna boresight location, and no spatial averaging of the geophysical parameters is performed (which would further smooth the geophysical fields). However, tri-linear interpolation of the NCEP data to the boresight point is done. We use the extracted NCEP data and the EIAs for the 6-36 GHz frequencies to simulate TBs that would be obtained from co-registered footprints using the footprint compositing routine.

We have processed 5 orbits (Table 14) at 5 different days of the year. We have also varied the equatorial crossing longitude in order to obtain different geographical locations of the CMIS orbits.

Table 14: Approximate time and location for simulated orbits.

Orbit	Date	Approximate local equatorial crossing time for ascending swath	Approximate equatorial crossing longitude for ascending swath
0	02 APR 1999	5:30	180
1	05 JUN 1999	5:30	180
2	06 JUN 1999	5:30	180
3	21 SEP 1999	5:30	0
4	03 APR 1999	5:30	60

Orbit 0 is used for algorithm training, i.e. for deriving the SST, wind speed, and atmospheric parameter regression coefficients. Following section 4.2.3.2, for the training orbit we do not use the EIA from the orbit simulator. Instead, we compute 5 training data sets that correspond to 5

ATBD for CMIS
Ocean EDR Algorithm Suite
Sea Surface Temperature EDR
Sea Surface Wind Speed/Direction EDR
Surface Wind Stress EDR

14-90

This document is intended for non-commercial use only. All other use is strictly forbidden without prior approval of the U.S. Government.

values for the 36 GHz EIA ($\theta_i(36)$) in steps of 0.5 deg. Given $\theta_i(36)$ and the nominal nadir angles θ_n at all frequencies, we compute the EIAs for the other frequencies as per equation (4.5).

The orbits 1-4 are set aside for testing the algorithm performance (Section 6). For these test data sets, we use the EIAs reported for each observation by the orbit simulator.

5.5.4. Geophysical Parameters from the NCEP GDAS FNL Analysis

As the next step, we need a set of geophysical parameters that will enable us to compute a value for the brightness temperature at each observation point using the full RTM from section 3. These parameters are listed in Section 5.2.

The NCEP GDAS FNL analysis provides W, φ_W, T_S, T(h), p(h) and RH(h). It is a global spectral model with series truncated at wave number 126 (T126), which is equivalent to a globally homogeneous grid resolution of 105 km. The model is run 4 times daily (00Z, 06Z, 12Z, 18Z) and available interpolated to a 1deg x 1 deg LAT-LON grid. We do not consider cases, where the observation is over either land or over ice. Each orbit contains approximately 400,000 – 500,000 valid observations.

The parameter φ_W is the wind direction relative to North, which determines the relative wind direction as $\varphi_r = \varphi_W - \varphi_i$, where φ_i is the look direction relative to North (φ_i is computed by the orbit simulator).

The NCEP GDAS FNL analysis contains basically no cases where $W > 18 \, m/s$. In order to obtain sufficiently large population of the higher wind speed bins we have applied a scaling to the NCEP wind speeds:

$$W \to W \cdot s(W)$$
$$s(W) := \frac{a + b \cdot W}{a + c \cdot W} \qquad (5.6)$$
$$a = -17.6454 \, m/s, \ b = 0.982133, \ c = 1$$

This scaling leaves the wind speed distribution below 15 m/s basically unchanged but ensures that the higher wind speed bins 15 m/s < W < 25 m/s are sufficiently populated for obtaining EDR error statistics.

5.5.5. Cloud Liquid Water

The NCEP GDAS FNL analysis does not contain clouds. In order to simulate clouds realistically we have prepared maps that contain values for the columnar liquid cloud water L measured from SSM/I for all the days for which the simulations were run (Table 14). In order to obtain as many valid measurements as possible we have collected data from all three available satellites, both for ascending and for descending swaths. If there were 2 or more valid

ATBD for CMIS
Ocean EDR Algorithm Suite
Sea Surface Temperature EDR
Sea Surface Wind Speed/Direction EDR
Surface Wind Stress EDR

14-91

This document is intended for non-commercial use only. All other use is strictly forbidden without prior approval of the U.S. Government.

measurements for L available, we have chosen the highest value. We chose a cloud base height $h_{base}=1000m$ and a cloud top height $h_{top}=3000m$. The cloud is assumed to have uniform liquid cloud water $\rho_L(h)=\bar{\rho}$ between the profile level h_k lying directly above h_{base} and the profile level h_l lying directly below h_{top}. Between h_{k-1} and h_k and between h_l and h_{l+1} the density is made to drop linearly from $\bar{\rho}$ to 0. The value for $\bar{\rho}$ is chosen so that $L = \int_0^\infty dh\, \rho_L(h)$.

5.5.6. Distribution of Geophysical Parameters

Figure 17 and Figure 18 show the distributions for wind speed W, SST, columnar water vapor V, columnar liquid cloud water L and relative wind direction φ_r for the NCEP training orbit data set 0 and the NCEP retrieval orbit data sets 1-4 from Table 14, together with the cloud profiles from section 5.5.5.
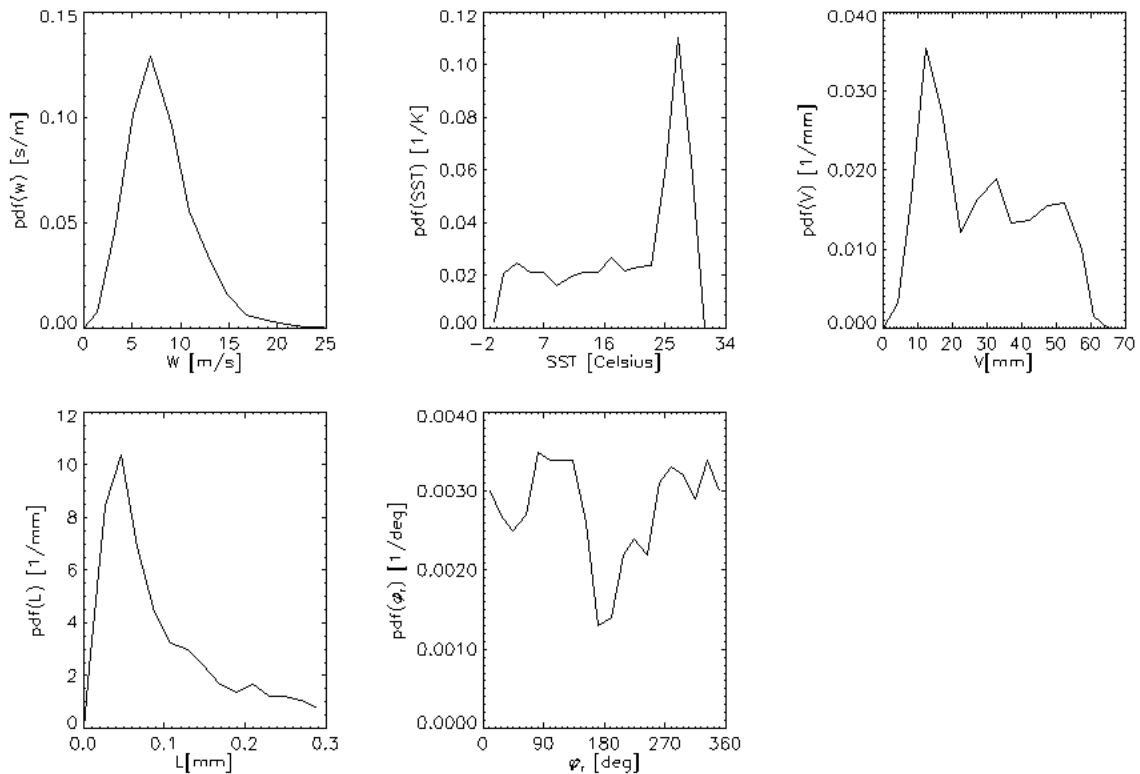
Figure 17: Distributions of Geophysical Parameters for the Training Orbit Data Set (Orbit 0).

ATBD for CMIS
Ocean EDR Algorithm Suite
Sea Surface Temperature EDR
Sea Surface Wind Speed/Direction EDR
Surface Wind Stress EDR

14-92
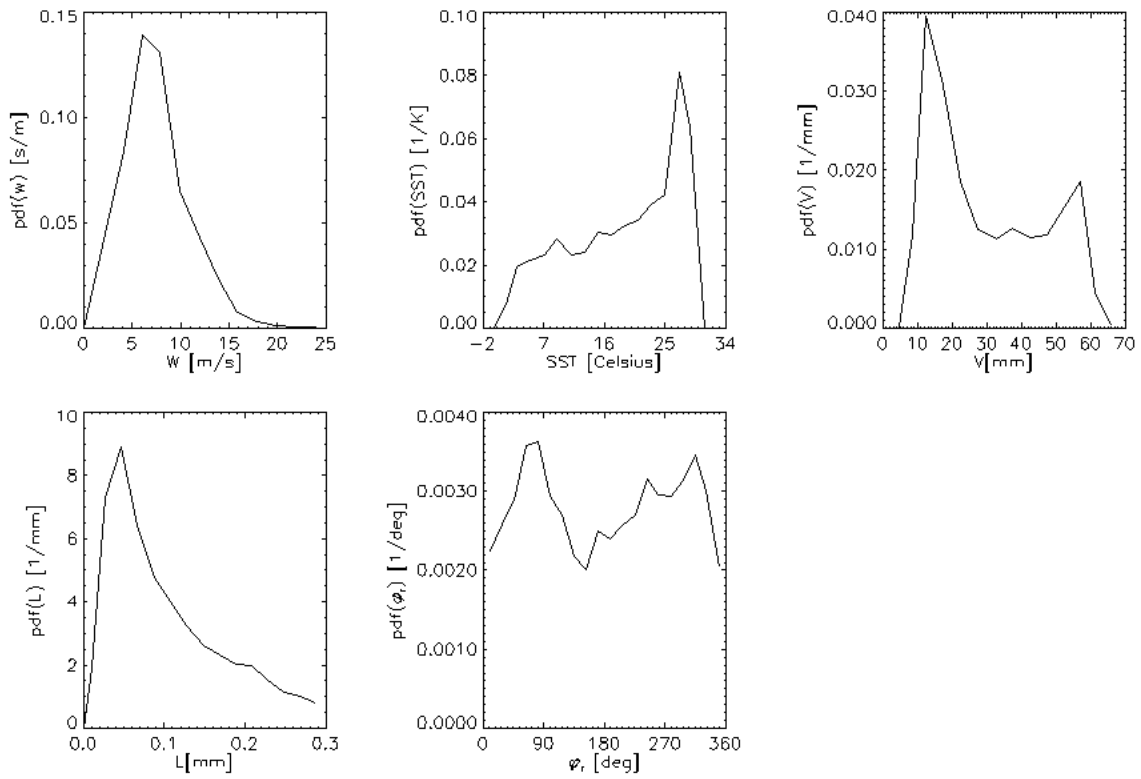
Figure 18: Distributions of Geophysical Parameters for the Test Orbits (Orbit 1-4).

6. Algorithm Performance

6.1. Simulation Method

6.1.1. Sensor Error Model

For the performance of all EDR algorithms in this section, other than the median filter, all sensor errors are included at the requirement levels. (The sensor errors included in the median filter will be discussed in Section 6.5). The sensor errors, their requirement values, and the method used for simulating them are included in Table 15. (See also EN #100 response.)

Table 15: Requirements Values and Simulation Method for Sensor Errors included in EDR Performance Statistics

Sensor Error	Bias/Random	Derived Requirement	Method of Simulation	Comment
Cross polarization* (M-matrix)	Constant	Polarization Purity 99%	Use Boeing computed M-matrices	Polarization Purity (diag elements) greater than 0.99
Cross-pol matrix knowledge**	Bias	0.001 (-30 dB) all elements	Gaussian noise with σ=0.001, independent for each matrix element	Simulated as random to avoid dependence of result on bias realization
M-matrix Magnitude	Constant	0.02 on columns of matrix eliminated in cross-pol correction	Replace each affected matrix element by 0.02 in Boeing computed matrices	Residual cross-polarization from polarizations not measured
Polarization Rotation (Control error)*	Bias + Random	0.60 deg RMS	Gaussian noise with σ=0.60 deg	
Polarization Rotation (Knowledge Error)***	Uncertainty	0.05 deg	Gaussian Noise with σ=0.05 deg	
EIA Control Error (ref 36 GHz)	Range	+/- 1 degree of nominal EIA	Boxcar distribution +/- 1 deg of nominal EIA	EIAs for all other frequencies are as per equation 4.5
EIA Knowledge**	Bias	0.06 deg	Gaussian noise, σ=0.06 deg	Simulated as noise because Boeing quotes knowledge bias as RMS
EIA Knowledge	Noise	0.02 deg	Gaussian noise, σ=0.02 deg	
TB accuracy (post calibration to RTM)	Common bias, all 6-36 GHz channels ($TB_{post\ cal}$-TB_{RTM})	0.10 K	0.10K added to all TBs post simulation of calibration to RTM	
TB accuracy (post calibration to RTM)	1-sigma of difference between ($TB_{post\ cal}$-TB_{RTM})	0.04K	Gaussian noise with σ=0.04K added to each	

ATBD for CMIS
Ocean EDR Algorithm Suite
Sea Surface Temperature EDR
Sea Surface Wind Speed/Direction EDR
Surface Wind Stress EDR

14-94

This document is intended for non-commercial use only. All other use is strictly forbidden without prior approval of the U.S. Government.

	for any two channels		channel	
Faraday Rotation	Not Applicable	No requirement	Constant 0.60 deg @ 10.7 GHz	FR can reach 0.6 deg at solar max
Faraday Rotation (Knowledge Error)	0.20 deg	0.20 deg @ 10.7 GHz		Requirement may not be met during magnetic storms

* Corrected (up to knowledge error) in SDR Algorithm Simulation

** The constant TB biases resulting from these knowledge error biases are corrected in the simulation of the Calibration to the RTM. The noise in the TBs due to these knowledge error biases is not corrected (calibration to RTM only takes out TB biases).

*** Bias portion should be ** above, which would improve all EDR performance, but not significantly. Requires breaking down RMS into bias and noise as per Boeing pointing budget.

The sensor error model provides a complete end-to-end simulation of all the sensor errors included (not just a poor-man simulation where brightness temperatures are perturbed according to the knowledge errors). That is, the effect of the sensor control errors are added to the TBs in the correct sequence, the knowledge errors are used to perturb the truth values of the control errors, and then the perturbed values of the control errors are used in the in the SDR algorithm, which corrects for the sensor cross-polarization, polarization rotation, and Faraday Rotation knowledge errors. A flow diagram for the sensor error model is shown in Figure 19.

ATBD for CMIS
Ocean EDR Algorithm Suite
Sea Surface Temperature EDR
Sea Surface Wind Speed/Direction EDR
Surface Wind Stress EDR

14-95

This document is intended for non-commercial use only. All other use is strictly forbidden without prior approval of the U.S. Government.
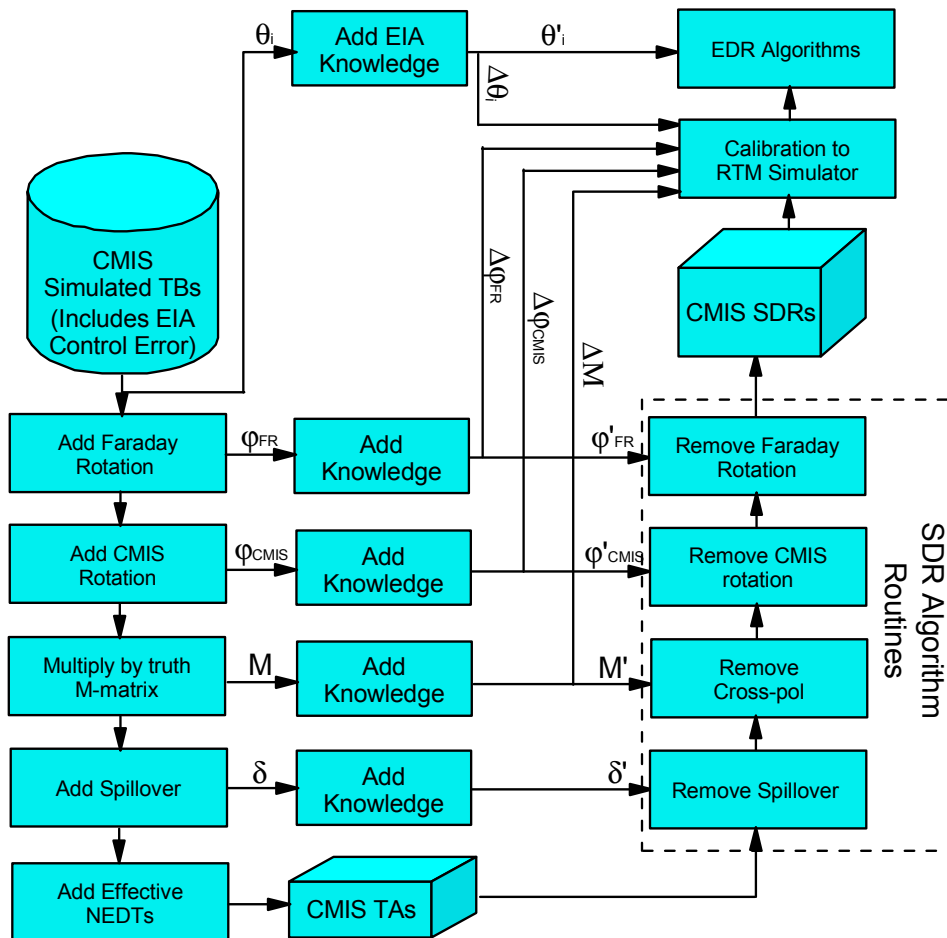
Figure 19: Sensor Error Simulation Model, Including SDR Algorithm and CMIS Calibration to RTM simulation . Knowledge error is added to each parameter before SDR correction routines. Bias portion of the knowledge errors (Δ's) are sent to calibration to RTM simulator; there the mean TB bias over the test data set due to each knowledge error bias is computed and subtracted from the TBs, i.e., replaced by the post-calibration TB accuracy errors. Spillover knowledge is turned off at this time, and $\Delta\varphi_{CMIS}$ is set to zero until error broken out into bias and noise (see *** below Table 15).

6.1.2. Calibration to the RTM

6.1.2.1.   Motivation

Calibration of the CMIS TBs to the radiative transfer model is assumed in all EDR error estimates given in this section for the SST, wind speed, and wind stress EDRs, as well as for the first ranked and closest wind direction ambiguities obtained using the radiosonde data sets. That is, we simulate the effect of the calibration of the CMIS TBs to the RTM as a last step before running the retrievals, as shown in Figure 19.

Calibration of the CMIS TBs to the RTM takes place during the Cal/Val period. A set of offsets (and/or slopes) are found that, when applied to the CMIS TBs, make them consistent with the RTM in the least squares sense. The calibration to the RTM removes the biases in the TBs with respect to the RTM, without regard to the source of the bias. While sensor knowledge error noise generates noise in the TBs exclusively, sensor knowledge error biases cause a bias component and a noise component in the TBs. The bias component is eliminated during the calibration to the RTM. We will now assess the TB bias component due to each of the sensor knowledge error biases. In the process, we will show that the bias component is much larger than the noise component.

The knowledge error in Faraday rotation, the cross-polarization matrix (M), and the CMIS rotation cause the SDR algorithm to produce imperfect TBs. We now compute the bias in the SDR TBs due to the bias component of each sensor knowledge error; these will be subtracted by the simulator, and replaced by the post-calibration TB accuracy errors as per Table 15.

6.1.2.2.   TB Bias Due to Cross Polarization Knowledge Bias

Let us begin by considering the effect of the M-matrix knowledge bias, ΔM, ignoring all other sensor errors. The vector T's below represent the TBs (all polarizations) for each frequency). The expression for the antenna temperatures is given in terms of the true cross-polarization matrix

$$\vec{T}_A = M_{true}\vec{T}_B \quad (6.1)$$

while the SDR cross-polarization correction uses the M-matrix that is computed from range measurements of the antenna

$$\vec{T}_{B,SDR} = M_{meas}^{-1} T_A . \quad (6.2)$$

The cross-polarization error matrix is defined as

$$\Delta M = M_{meas} - M_{true} \quad (6.3)$$

Therefore the SDR derived brightness temperatures can be expressed as

$$\begin{aligned}
\vec{T}_{B,SDR} &= M_{meas}^{-1} M_{true} \vec{T}_B \\
&= M_{meas}^{-1} \left(M_{meas} - \Delta M \right) \vec{T}_B \quad (6.4) \\
&= \left(I - M_{meas}^{-1} \Delta M \right) \vec{T}_B
\end{aligned}$$

So, the difference between the true and the SDR derived TB's is

$$\Delta T_B = \vec{T}_{B,SDR} - \vec{T}_B = -M_{meas}^{-1} \Delta M \vec{T}_B . \quad (6.5)$$

Define the residual cross-polarization matrix as

$$\Delta M_r \equiv -M_{meas}^{-1} \Delta M = -\left(M_{true} + \Delta M \right)^{-1} \Delta M \quad (6.6)$$

so that

$$\Delta T_B = \Delta M_r \vec{T}_B . \quad (6.7)$$

To first order in ΔM,

$$\Delta M_r = -M_{true}^{-1} \Delta M . \quad (6.8)$$

As shown in the SDR algorithm ATBD, the M-matrix differs from the identity matrix by less than 0.02 in any matrix element. Therefore,

$$\Delta M_r \approx -\Delta M \quad (6.9)$$

This approximation says that, if the cross-polarization from polarization q into polarization p is over (under) estimated in the measured M-matrix by $\Delta M_{pq} > 0$ (<0), then the SDR product for polarization p will have a residual component of polarization q approximated by - ΔM_{pq}.

ATBD for CMIS
Ocean EDR Algorithm Suite
Sea Surface Temperature EDR
Sea Surface Wind Speed/Direction EDR
Surface Wind Stress EDR

14-97

This document is intended for non-commercial use only. All other use is strictly forbidden without prior approval of the U.S. Government.

Our simulations of the SDR algorithm show that there is actually an amplification of ΔM by multiplication by the inverse of the measured M-matrix in equation (6.6). The amplification is equal to the inverse of the average diagonal (co-pol) matrix element. Since the co-pol matrix elements are greater than 0.99, the amplification is generally less than 1%, or negligible. In other words, for our purposes, equation (6.9) is accurate to 1%. (But , in general the size of the residual cross-polarization is dependent on the inverse of the polarizations purities.)

There is a symmetry property of the cross-polarization error matrix that we need to proceed. The cross-polarization matrix for the SDR algorithm is written in the basis of the individual polarizations, i.e., where the T's in the above equations are represented by

$$\bar{T} = \begin{pmatrix} T_V \\ T_H \\ T_P \\ T_M \\ T_L \\ T_R \end{pmatrix} \quad (6.10)$$

Let the matrix element which describes the cross-polarization of polarization a into antenna polarization b be expressed as M_{ba}. In SDR algorithm ATBD Appendix B, we show that any valid M-matrix (including the true and measured M-matrices) can always be written in the form

$$M = \begin{pmatrix} M_{vv} & 1-M_{vv} & M_{vp} & -M_{vp} & M_{vl} & -M_{vl} \\ M_{hv} & 1-M_{hv} & M_{hp} & -M_{hp} & M_{hl} & -M_{hl} \\ M_{PV} & -M_{pv} & M_{pp} & 1-M_{pp} & M_{pl} & -M_{pl} \\ M_{mv} & -M_{mv} & M_{mp} & 1-M_{mp} & M_{ml} & -M_{ml} \\ M_{lv} & -M_{lv} & M_{lp} & -M_{lp} & M_{ll} & 1-M_{ll} \\ M_{rv} & -M_{rv} & M_{rp} & -M_{rp} & M_{tl} & 1-M_{rl} \end{pmatrix} \quad (6.11)$$

Therefore, it must be possible to write the cross-polarization error matrix as

$$\Delta M = \begin{pmatrix} \Delta M_{vv} & -\Delta M_{vv} & M_{vp} & -\Delta M_{vp} & \Delta M_{vl} & -\Delta M_{vl} \\ \Delta M_{hv} & -\Delta M_{hv} & M_{hp} & -\Delta M_{hp} & \Delta M_{hl} & -\Delta M_{hl} \\ \Delta M_{pv} & -\Delta M_{pv} & M_{pp} & -\Delta M_{pp} & \Delta M_{pl} & -\Delta M_{pl} \\ \Delta M_{mv} & -\Delta M_{mv} & M_{mp} & -\Delta M_{mp} & \Delta M_{ml} & -\Delta M_{ml} \\ \Delta M_{lv} & -\Delta M_{lv} & M_{lp} & -\Delta M_{lp} & \Delta M_{ll} & -\Delta M_{ll} \\ \Delta M_{rv} & -\Delta M_{rv} & M_{rp} & -\Delta M_{rp} & \Delta M_{rl} & -\Delta M_{rl} \end{pmatrix} (6.12)$$

Our simulations of the SDR algorithm show that the residual cross-polarization matrix ΔM_r takes the same form as equation (6.12). Therefore, the error in the SDR derived TB for polarization "a" is

ATBD for CMIS
Ocean EDR Algorithm Suite
Sea Surface Temperature EDR
Sea Surface Wind Speed/Direction EDR
Surface Wind Stress EDR

14-98

This document is intended for non-commercial use only. All other use is strictly forbidden without prior approval of the U.S. Government.

$$\Delta T_{Ba} = [\Delta\mathbf{M}_r]_{av} T_Q + [\Delta\mathbf{M}_r]_{ap} T_3 + [\Delta\mathbf{M}_r]_{al} T_4 \quad (6.13)$$

That is, the error can be expressed purely in terms of the Stokes parameters

$$T_Q = T_{Bv} - T_{Bh}$$
$$T_3 = T_{Bp} - T_{Bm} \quad (6.14)$$
$$T_4 = T_{Bl} - T_{Br}$$

We now compute the bias and noise error in the SDR derived TBs (before the calibration), over a global ensemble of CMIS observations:

$$\langle \Delta T_{Ba} \rangle = [\Delta\mathbf{M}_r]_{av} \langle T_Q \rangle + [\Delta\mathbf{M}_r]_{ap} \langle T_U \rangle + [\Delta\mathbf{M}_r]_{al} \langle T_4 \rangle \quad (6.15)$$

$$\sigma_{T_{Ba}}^2 = [\Delta\mathbf{M}_r]_{av} \sigma_{T_Q}^2 + [\Delta\mathbf{M}_r]_{ap} \sigma_{T_U}^2 + [\Delta\mathbf{M}_r]_{al} \sigma_{T_4}^2 \quad (6.16)$$

Now, if we assume that wind directions approximately uniformly distributed over the globe, the average of T_3 and T_4 will be near zero. On the other hand, T_Q is always very large for ocean scenes. Table 16 shows the mean and standard deviation of T_Q, T_3, and T_4 for across all test data sets. Plugging in the numbers shows that the TB bias is much larger than the TB noise caused by the M-matrix knowledge bias. It also shows that the TB bias is approximated well by

$$\Delta T_{Ba} \cong [\Delta\mathbf{M}_r]_{av} \langle T_Q \rangle \quad (6.17)$$

The calibration to the RTM will remove this constant bias. Therefore, in the simulation of the calibration to the RTM, we subtract from the SDR derived brightness temperature for each polarization a, the ΔT_{Ba} defined by equation (6.17); that is we subtract the a'th element of the first row in Mr times the <TQ> from the table from the TBs. For this, the terms in ΔM_r are calculated exactly as per equation (6.6). This same set of 18 constants (one for each channel) are subtracted from SDR derived brightness temperatures for all observations.

Table 16: Mean and Standard Deviation of Stokes Parameters for Ocean Scenes. Computed from radiosonde test data sets.

Freq	$\langle T_Q \rangle$	$\langle T_3 \rangle$	$\langle T_4 \rangle$	σ_{TQ}	σ_{T3}	σ_{T4}
6	86	0	0	6	0.7	0.3
10	92	0	0	7	1.1	0.5
18	62	0	0	9	0.9	0.4
23	43	0	0	14	0.7	0.3
36	56	0	0	11	0.8	0.3

ATBD for CMIS
Ocean EDR Algorithm Suite
Sea Surface Temperature EDR
Sea Surface Wind Speed/Direction EDR
Surface Wind Stress EDR

14-99

6.1.2.3.   TB Bias due to CMIS polarization Rotation Knowledge Bias

The bias in the brightness temperatures due to the bias component of the rotation knowledge error is also removed in the simulation of the calibration to the RTM. The analogous equations for the rotation corrections, assuming a rotation knowledge bias of $\Delta\varphi$ are:

$$\bar{T}_{B,SDR} = R(\varphi_{true} + \Delta\varphi)^{-1} R(\varphi_{true})\bar{T}_B = R(-\Delta\varphi)\bar{T}_B \ (6.18)$$

$$\Delta\bar{T}_B = (R(-\Delta\varphi) - I)\bar{T}_B$$
$$\equiv \Delta R_r \bar{T}_B \qquad (6.19)$$

Since the rotation matrix R is defined by

$$R(\varphi) = \begin{pmatrix} \cos^2\varphi & \sin^2\varphi & \sin\varphi\cos\varphi & -\sin\varphi\cos\varphi & 0 & 0 \\ \sin^2\varphi & \cos^2\varphi & -\sin\varphi\cos\varphi & \sin\varphi\cos\varphi & 0 & 0 \\ -\sin\varphi\cos\varphi & \sin\varphi\cos\varphi & \cos^2\varphi & \sin^2\varphi & 0 & 0 \\ \sin\varphi\cos\varphi & -\sin\varphi\cos\varphi & \sin^2\varphi & \cos^2\varphi & 0 & 0 \\ 0 & 0 & 0 & 0 & 1 & 0 \\ 0 & 0 & 0 & 0 & 0 & 1 \end{pmatrix} \qquad (6.20)$$

it is easy to show that ΔR_r has the same anti-symmetry properties as ΔM_r, as in equation (6.12). Therefore the bias and noise errors in the SDR derived TB are

$$\langle\Delta T_{Ba}\rangle = [\Delta R_r]_{av}\langle T_Q\rangle + [\Delta R_r]_{ap}\langle T_U\rangle \ (6.21)$$

and

$$\sigma^2_{T_{Ba}} = [\Delta R_r]_{av}\sigma^2_{T_Q} + [\Delta R_r]_{ap}\sigma^2_{T_U} \ (6.22)$$

As with the M knowledge bias error, we see that the TB bias due to a rotation knowledge bias error is much larger than the TB noise due to the same effect. Also, an excellent approximation to the TB bias in polarization "a" is

$$\langle\Delta T_{Ba}\rangle = [\Delta R_r]_{av}\langle T_Q\rangle \ (6.23)$$

Therefore, in the simulation of the calibration to the RTM we subtract the constant $<\Delta T_{Ba}>$ (as defined by equation (6.23) and Table 16) from the SDR derived TBs for all observations.

6.1.2.4.   TB Bias due to Earth Incidence Angle Knowledge Bias

The Earth incidence angle knowledge error is handled differently. Here, the EDR algorithms use the reported EIA (which includes the EIA knowledge bias) to interpolate the regression

ATBD for CMIS
Ocean EDR Algorithm Suite
Sea Surface Temperature EDR
Sea Surface Wind Speed/Direction EDR
Surface Wind Stress EDR

14-100

coefficients and also in computing the model function in the wind vector search routine. The same is true during calibration to the RTM; the reported EIA will be used in simulating the TBs with the RTM, while the CMIS TBs will be for the true EIA. The calibration to the RTM essentially adds a bias to the SDR derived TBs which essentially corrects them to the reported incidence angle.

In any observation, the difference between the CMIS TBs and those computed using the reported EIA will be.

$$\Delta \bar{T}_B = \bar{T}_B(\theta_i + \Delta\theta_i) - \bar{T}_B(\theta_i) = \frac{\partial \bar{T}_B}{\partial \theta_i} \Delta\theta_i \quad (6.24)$$

Therefore, mean and standard deviation of the TB difference for polarization "a" is

$$\langle \Delta T_{Ba} \rangle = \left\langle \frac{\partial T_{Ba}}{\partial \theta_i} \right\rangle \Delta\theta_i \quad (6.25)$$

$$\sigma_{T_{Ba}} = \sigma_{\frac{\partial T_{Ba}}{\partial \theta_i}} \Delta\theta_i \quad (6.26)$$

Values for these, computed using the radiosonde test data sets, are shown in Table 17. For most channels, the situation is analogous to the situation with cross-polarization and rotation biases; the mean error in the TBs is significantly larger than the standard deviation error. However, for the 18-36 GHz horizontally polarized channels, the opposite is true for the EIA bias; it creates more noise over the data set than bias. This points out the value of the end-to end simulation including the calibration to the RTM in generating realistic EDR performance estimates. Only those portions of sensor bias errors that would actually be removed by the SDR algorithm and the calibration to the RTM are removed from the TBs in our simulation.

Table 17: Mean and Standard Deviation of dTB/dEIA (K/deg) over the Radiosonde Test Data Sets

Freq	v	v	h	h	p,m,l,r	p.m.l.r
	Mean	Std. Dev	Mean	Std. Dev	Mean	Std. Dev
6	2.67	0.12	-1.13	0.07		
10	2.92	0.14	-1.02	0.10	0.955	0.07
18	2.34	0.13	-0.20	0.40	1.074	0.23
23	2.04	0.19	0.59	0.56		
36	2.20	0.18	0.33	0.415	1.263	0.224

In any case, the constant for each channel defined by equation (6.25) and Table 17 are added to the SDR derived TBs in the simulation of the calibration to the RTM.

ATBD for CMIS
Ocean EDR Algorithm Suite
Sea Surface Temperature EDR
Sea Surface Wind Speed/Direction EDR
Surface Wind Stress EDR

14-101

6.2. Performance of the SST Algorithm

6.2.1. Conditions for Algorithm Testing

While the radiosonde training data set with uniform wind speed distribution was used to train the algorithm, the radiosonde data set with a Rayleigh wind speed distribution is used to test it, due to the concerns raised in Section 5.4.6.2. over the necessity to duplicate the natural wind speed distribution as a function of SST as closely as possible.

All sensor errors are simulated at the requirements level using the sensor error model described in section 6.1.1. The NEDTs are the effective NEDTs for a 3dB composite footprint of 86 x 52 km, computed from the single observation NEDT and the effective NRFs of Section 4.3.2.1. A calibration of the TBs to the RTM is assumed, and is simulated using the calibration model of the last section.

6.2.2. Binning of Retrieval Errors

The retrieval error statistics are binned in 2 K increments of the truth SST, with the first bin starting at –2 K, and the last bin ending at 40 K. The measurement accuracy, precision and uncertainty are computed as the mean, standard deviation, and RMS error of the retrievals with respect to the truth SST value for each simulated ocean-atmosphere scene in the test data set.

6.2.3. Performance

The performance of the SST EDR algorithm is shown in Figure 20, and a comparison to the SRD requirements is shown in Table 18. The performance meets all EDR error requirements when compared to the SST truth values used to simulate the brightness temperatures. It is therefore reasonable to assume that the SST EDR meets all SRD EDR error requirements with respect to the uniform average of SST over a 86x52 km rectangle.

But, the Horizontal Cell Size requirement is 50 km, and the question is then, what is the spatial error between SST weighted average over the 86 x 52 km composite and the uniform average of SST over a 50 km square centered at the same location. If there is a constant gradient across the area where the composite is located, there is no spatial error. Spatial error is therefore of concern only where the SST gradient changes abruptly in or near the horizontal cell; this can occur at the edge of the Western Boundary Currents (Gulf Stream, Agulhas, and Kuroshio currents, at the edge of the loop current in the Gulf of Mexico, an the edge of the tropical instability waves during La Nina). In total, these areas constitute a very low fraction of the ocean surface. (To be continued.) (See also EN #8 and #100 responses.)

SST EDR Performance over Measurement Range
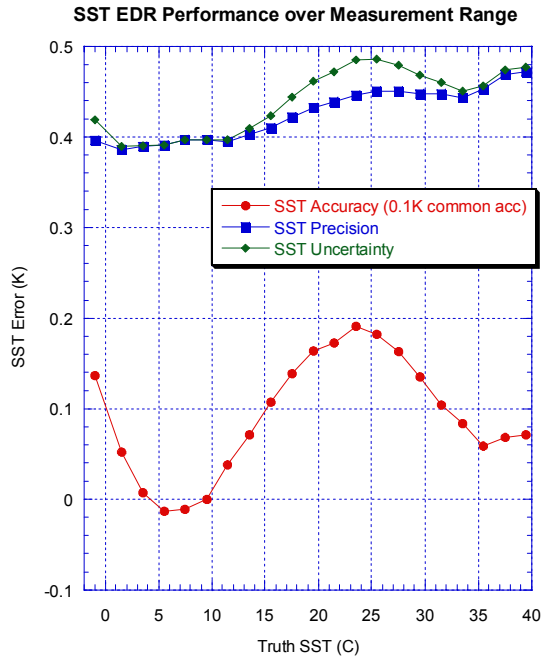
Figure 20: SST EDR Algorithm Performance with all Sensor Errors at Requirements Level

The departure of the uncertainty from the precision curve at intermediate values of the SST is caused by the rise of the accuracy error in that range. Previous illustrations of the performance did not include the 0.1K TB accuracy error common to all channels (requirement for the calibration to the RTM). Without this error, the accuracy curve has the same shape, but the overall accuracy error (unbinned) is zero, and the uncertainty curve departs very little from the precision curve (for example see the accuracy curve in PDSR slide 3e-15, although note that a Rayleigh wind speed distribution with $<W>=7.5$ m/s across all SSTs was used there, giving larger SST precision errors).

A common TB accuracy error with value x Kelvin shifts the entire accuracy curve by x Kelvin (the ratio of the shift to the TB common accuracy error is 1.0). Thus, the overall SST accuracy error here is 0.1K. It is the shifting of the accuracy error curve due to the common accuracy error that results in the hump in the SST uncertainty curve at intermediate SST values.

In the performance column of the table, we give minimum and maximum EDR errors, a typical value across the measurement range, and overall value (unbinned, all SSTs).

Table 18: Comparison of SST EDR Performance to SRD Requirements

Paragraph Number	Description	Threshold	Objective	Performance
C40.2.4-1	a. Horizontal Cell	50 km	25 km (TBR)	50 km

ATBD for CMIS
Ocean EDR Algorithm Suite
Sea Surface Temperature EDR
Sea Surface Wind Speed/Direction EDR
Surface Wind Stress EDR

14-103

This document is intended for non-commercial use only. All other use is strictly forbidden without prior approval of the U.S. Government.

	Size			
C40.2.4-5	b. Horizontal Reporting Interval	(TBD)	(TBD)	50 km
C40.2.4-6	c. Horizontal Coverage	Oceans	Oceans	Oceans
C40.2.4-8	d. Measurement Range	271 – 313 K	271 – 313 K	271 – 313 K (-2 to 40 C)
C40.2.4-9	e. Measurement Uncertainty (TBR)	0.5K (TBR)	0.1K	0.39 K- 0.49 K 0.49 K maximum <0.47 K typical 0.44 K overall
C40.2.4-10	f. Measurement Accuracy	(TBD)	0.1K	0.01 - 0.19 K 0.19 K maximum <0.16 K typical 0.10 K overall
C40.2.4-11	g. Measurement Precision	(TBD)	0.1K	0.37- 0.47 K 0.47 K maximum <0.45 K typical 0.43 K overall
C40.2.4-12	h. Mapping Uncertainty	5 km	1 km (TBR)	
C40.2.4-16	i. Swath Width	1700 km (TBR)	3000 km (TBR)	>1700 km

6.2.4. Stratification with Respect to Geophysical Parameters

Figure 21 shows the stratification of SST retrieval errors over the ranges of SST (-2 to 40 C), wind speed (0-25 m/s), columnar water vapor (0-70 mm), cloud liquid water (0-0.3 mm), and relative wind direction contained in the test data set. Here, we use the radiosonde test data set with uniform wind speeds so that enough high wind speed retrievals are included to give accurate error statistics, but this has the effect of artificially increasing the SST errors due to wind direction cross-talk, as discussed in Section 5.4.6.2. However, the purpose of the stratification is to show that the EDR errors do not vary appreciably over the range of the stratification variables, and so the error values in the figure should be considered in a relative sense.

Each plot in the figure shows the mean bias error (accuracy, solid line), plus and minus one standard deviation error (precision, dashed lines) for each bin of each stratification variable. The stratification bins are 2 m/s in wind speed, 5mm in water vapor, 0.03 mm in cloud water, and 18 degrees in wind direction.

It should be noted that each bin of the stratification by one geophysical parameter contains retrievals from the entire distribution of all other geophysical parameters. That is, errors for each wind speed bin include the entire range of SST, and each wind direction bin contains all wind speeds, etc.   Therefore, one is examining the unbinned SST performance over the range of the other geophysical parameters. Questions such as "what is the difference between the performance of the algorithm at high and low SST for high wind speeds" cannot be answered by such plots.

ATBD for CMIS
Ocean EDR Algorithm Suite
Sea Surface Temperature EDR
Sea Surface Wind Speed/Direction EDR
Surface Wind Stress EDR

14-104

This document is intended for non-commercial use only. All other use is strictly forbidden without prior approval of the U.S. Government.
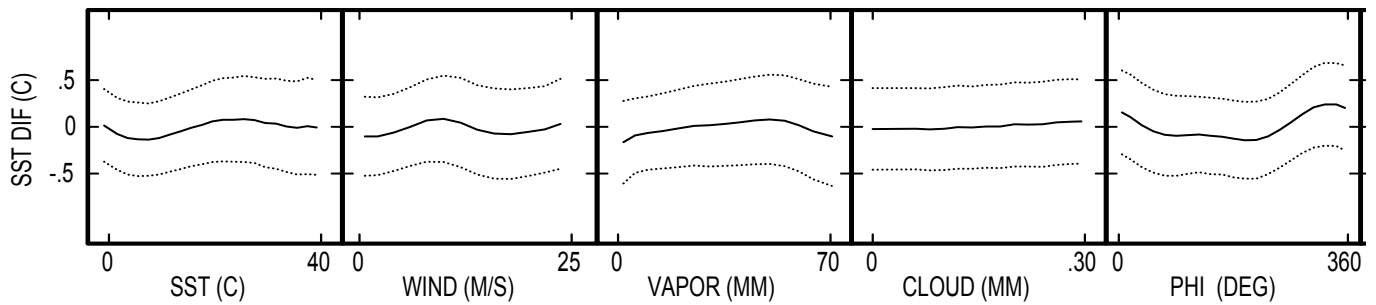
Figure 21: Stratification of SST EDR Accuracy and Precision Errors.

We refer to these plots as "cross-talk plots." Cross-talk between the EDR retrieval and another geophysical parameter occurs when there is some overlap between the signatures of the EDR and the geophysical parameter, i.e. when a change in the geophysical parameter results in change to the TBs over frequency and polarization that cannot be completely distinguished from a change in the EDR value. (When this occurs, we say that the signatures are not orthogonal). In this case, a given value of the non-orthogonal geophysical parameter will add bias the TBs that cannot be distinguished from a change in the EDR value. At a different value of the geophysical parameter, the biases will be different. For a given value of the GPP, the constant biases in the TBs of this form over all the retrievals will lead to a non-zero EDR retrieval bias. The retrieval bias depends on the value of the GPP. In summary, we expect cross-talk to show up as a non-zero retrieval bias error that varies over the stratification range of a GPP whose signature is not orthogonal to the EDR signature.

It is clear from the stratification plots that there is no significant cross-talk from the other geophysical parameters except wind direction. This indicates that the retrieval algorithm is performing as expected, as little cross-talk was expected from wind speed, water vapor or cloud water, all of whose signatures are nearly orthogonal to the SST signature.

The wind direction signal is not completely separable from the SST signal because of different harmonic dependence across polarization and frequency, and therefore some cross-talk from wind direction is expected. The cross-talk is periodic in 360 degrees, but is not symmetric about 180 degrees. It also accurately mirrors the cross-talk seen in the Wentz TMI SST retrievals, although here the amplitude of the cross-talk is exaggerated by the over-weighting toward large wind speeds from using a uniform wind speed distribution in the test data set.

The amount of wind direction cross-talk depends on the size of the wind direction signal, especially at 6 GHz. If the wind direction signal is smaller at 6 GHz than we have assumed (c.f. Section 3.7.4), the cross-talk will be smaller as well.

6.2.5. Stratification with Respect to Faraday Rotation

The SST EDR algorithm is most dependent on the 6V channel. Faraday rotation that is larger than twice the tilt angle of the polarization ellipse at 6 GHz will lower the 6V brightness temperature, and correspondingly, the SST. Across the test dataset, the polarization ellipse at 6

GHz is tiled by typically less than 0.2 degrees. Faraday rotation is inverse frequency dependent, and therefore 2.6 times larger at 6.6 GHz than at 10.7 GHz. Therefore, we expect that Faraday rotation will begin to affect the SST accuracy at somewhat less 0.2 degrees at 10.7 GHz. (Hereinafter, all references to Faraday rotation will be at 10.7 GHz)

The SST retrieval errors are stratified by Faraday rotation in Figure 22. This is an IDR era analysis, in which we used the uniform wind speed radiosonde test data set for the retrievals (again, artificially increasing the SST precision error). No sensor errors other than NEDTs were included. However, this analysis is fine for determining at what point Faraday rotation begins to affect the performance.

The figure corroborates the above analysis on the appearance of a bias error in the SST retrievals. The bias appears at about 0.1 deg, and becomes large enough to make the uncertainty curve pull away from the precision curve at 0.2 deg. In conjunction with similar analyses for the other ocean EDRs, the requirement on Faraday rotation knowledge error (in the SDR cross-polarization correction) was set at 0.2 deg. However, it appears that the SST bias is significant enough to raise the uncertainty curve appreciably only for Faraday rotation above 0.3 deg. We therefore expect the SST EDR errors to meet threshold over all SST bins for residual Faraday rotation less than 0.3 deg.
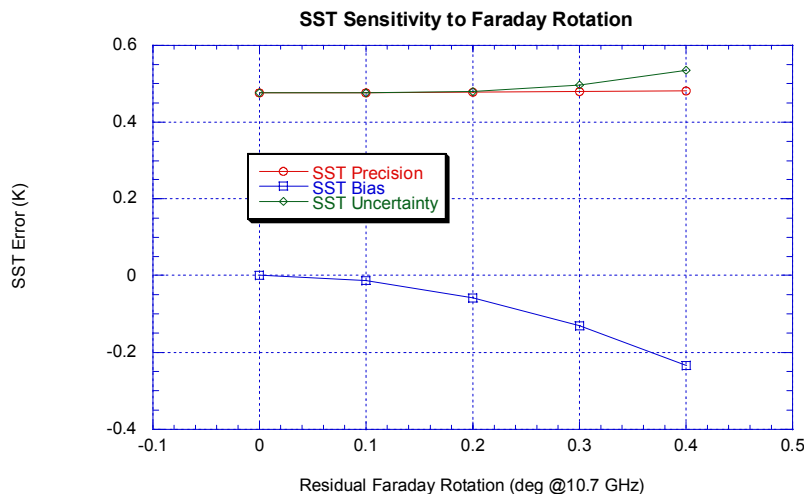
Figure 22: Stratification of SST Performance by Faraday Rotation

6.3. Performance of the 20 km Wind Speed Algorithm

6.3.1. Conditions for Algorithm Testing

The algorithm is trained and tested with uniform wind speed radiosonde data sets. Because performance estimates to be compared with the SRD requirements are binned according to wind speed, the distribution of wind speeds does not affect the results. However, in each bin of the

ATBD for CMIS   14-106   This document is intended for non-commercial
Ocean EDR Algorithm Suite   use only. All other use is strictly forbidden without
Sea Surface Temperature EDR   prior approval of the U.S. Government.
Sea Surface Wind Speed/Direction EDR
Surface Wind Stress EDR

stratification plots, the higher wind speeds will be over-weighted compared to the natural distribution.

All sensor errors are simulated at the requirements level, and a calibration of the TBs to the RTM has been assumed, both as described in Section 0. The NEDTs are the effective NEDTs for a 3 dB composite footprint of 20 x 20 km, average values of which are shown in Table 10 of Section 4.4.2.1.

6.3.2. Binning and Retrieval Errors

For the performance statistics to be compared with the SRD requirements, the wind speed errors are broken into 13 bins, with the first bin for wind speeds of 0-1 m/s, and subsequent bin having a width of 2 m/s. The maximum value included in the last bin is 25 m/s.

6.3.3. Performance

The performance of the 20 km wind speed algorithm is shown in Figure 23, and comparison of the performance with the SRD requirements appears in the Table 19.
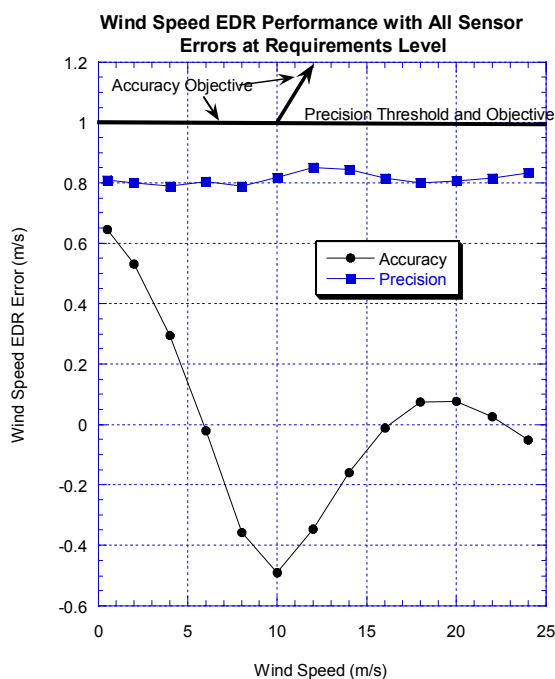
Figure 23: Wind Speed EDR Performance with All Sensor Errors at Requirements Levels

The table and figure make it clear that the EDR algorithm performance meets all EDR error objective requirements, when compared to the truth values used to simulate the TBs in the test data set; this is true whether or not the accuracy and precision requirements are switched or not.

ATBD for CMIS
Ocean EDR Algorithm Suite
Sea Surface Temperature EDR
Sea Surface Wind Speed/Direction EDR
Surface Wind Stress EDR

14-107

This document is intended for non-commercial use only. All other use is strictly forbidden without prior approval of the U.S. Government.

Given that the 3dB composite footprint for retrieval is 20 x 20 km, it is reasonable to assume that the wind speed EDR will meet or exceed those objective requirements when compared to the uniform average of wind speed over a 20 x 20 km square. That is the EDR error objectives will be met with respect to the Horizontal Cell Size threshold.

Table 19: Comparison of 20 km Wind Speed EDR to SRD Requirements

Paragraph Number	Description	Threshold	Objective	Performance
C40.2.5-1	a. Horizontal Cell Size	20 km	1 km	20 km
C40.2.5-2	b. Horizontal Reporting Interval	(TBD)	(TBD)	<20 km
C40.2.5-3	c. Horizontal Coverage	Oceans	Oceans	Oceans
C40.2.5-4	d. Measurement Range	3-25 m/s	1-50 m/s	0-25 m/s
C40.2.5-6	f. Measurement Accuracy	2 m/s or 20% of true value, whichever is greater	1 m/s or 10% of true value, whichever is greater	-0.49 to 0.65 m/s 0.65 m/s maximum <0.40 m/s typical 0.01 m/s overall
C40.2.5-8	g. Measurement Precision	1 m/s	1 m/s	0.79 – 0.85 m/s 0.85 m/s maximum <0.82 m/s typical 0.87 m/s overall
C40.2.5-10	h. Mapping Uncertainty	5 km	1 km (TBR)	
C40.2.5-11	i. Swath Width	1700 km (TBR)	3000 km (TBR)	>1700 km

Of all the ocean EDR algorithms, the 20 km wind speed algorithm is least sensitive to sensor errors. In fact, the curves in the figure differ very little from those that would be found for no sensor errors other than NEDTs. Furthermore, the TB common accuracy error does not shift the accuracy curve away from zero as it did with the SST results. This is one of the simplest algorithms to write, yet the most difficult to degrade the performance with sensor errors (or Faraday rotation).

It may seem strange that the overall precision error is larger than the maximum precision error in any of the wind speed bins. This is not a mistake. This occurs because the overall precision error includes the bias in the bins. One way to see this is to consider the overall uncertainty, i.e. RMS error over the entire dataset. This obviously includes the accuracy error in each bin. Since the overall precision is the square root of the difference of the squares of the overall uncertainty and accuracy, and the overall accuracy error is very close to zero, this means that the precision error includes the effect of the accuracy error in each bin.

The shape of the accuracy curve in Figure 23 deserves some explanation. Regression algorithms that include quadratic terms in the TBs, like the wind speed algorithm, operate well under conditions where the EDR signature is quadratic in the brightness temperatures, but fair less well when the quadratic coefficients are changing rapidly. The latter is the case over the onset (7 m/s) and dominance (12 m/s) of foam over diffraction in the isotropic wind speed signal, as can be seen from equations (3.57) through (3.59) and the discussion that follows. We believe

ATBD for CMIS   14-108   This document is intended for non-commercial
Ocean EDR Algorithm Suite   use only. All other use is strictly forbidden without
Sea Surface Temperature EDR   prior approval of the U.S. Government.
Sea Surface Wind Speed/Direction EDR
Surface Wind Stress EDR

that the kink in the accuracy curve that includes these wind speeds is a result of the algorithm's imperfect accommodation of the change in the wind direction signature this regime.

6.3.4. Stratification by Other Geophysical Parameters

The following figure shows the stratification of the 20 km wind speed retrieval errors over the range of SST (-2 to 40 C), columnar water vapor (0-70 mm), cloud liquid water (0-0.3 mm) and wind direction (0-360 deg) contained in the radiosonde test data set. As with the SST stratification the plots are the accuracy error (solid line) plus and minus the precision error (dashed lines) for each bin in the stratification. The bin sizes are discussed in Section 6.2.4. As always, we have used the uniform wind speed radiosonde test data set for the stratification. This is the same data set used to determine the EDR errors in Figure 23 and Table 19.

No significant cross-talk occurs from SST or cloud liquid water. The drop in the wind speed bias at high SST is probably a result of the distribution of SST tailing off in the training and test data sets (Figure 16).   The precision error does increase somewhat at large cloud water values, but this is a natural result of the wind speed signature in the TBs being attenuated by cloud absorption. Even at 0.3mm, the wind speed precision meets the objectives.

The cross-talk at very low water vapor probably results from the fact that the water vapor absorption is near linear (flat) at low vapor, while the training data contains mostly intermediate water vapor values, where exponential dependence of the absorption is in effect. The accuracy plus precision curve is cut off by the plot at low vapor, but the numerical results indicate that the accuracy error is 1.2 m/s for V<2 mm, and the precision error is 1.1 to 1.6 m/s for V<6 mm. We therefore believe, that neither the accuracy objectives nor precision thresholds will be met under conditions of such low vapor. However the occurrence of such low columnar water vapor over the oceans is rare (less than 5 % of the observations, according to Figure 17, Figure 18, and by Wentz's estimate).
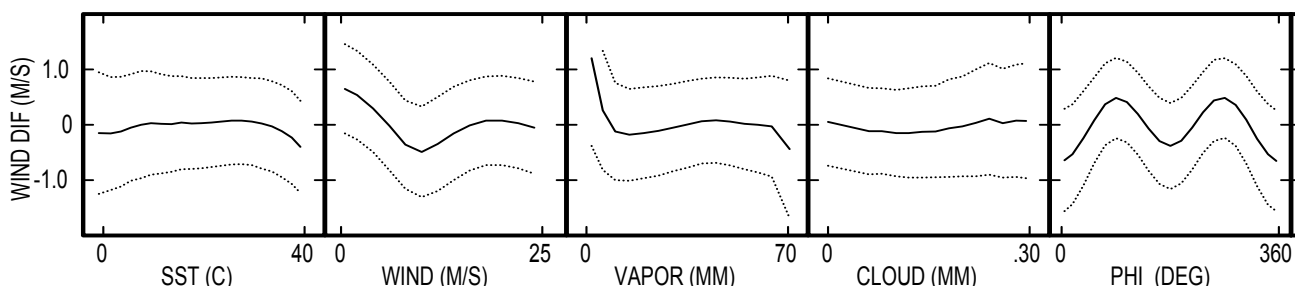
Figure 24: 20 km Wind Speed EDR Error Stratification

The cross-talk from wind direction is another matter entirely. Due to the differing harmonic dependence of the wind direction signal at different frequencies and polarizations, one can find a range of relative wind directions for which the signature is not orthogonal in the 6-36 GHz range to that for any chosen geophysical parameter. This makes wind direction cross-talk ubiquitous across all EDR algorithms that depend heavily on these frequencies.

Here we see that the wind direction cross-talk is periodic in 360 degrees, and shows even symmetry about 180 degrees. The amplitude (0.5 m/s) is exaggerated by using a uniform distribution in wind speeds to test the algorithm, because higher wind speeds are over represented

ATBD for CMIS   14-109   This document is intended for non-commercial
Ocean EDR Algorithm Suite   use only. All other use is strictly forbidden without
Sea Surface Temperature EDR   prior approval of the U.S. Government.
Sea Surface Wind Speed/Direction EDR
Surface Wind Stress EDR

relative to the natural (Rayleigh distribution), and the wind direction signal is larger at larger wind speeds. It is important to note that, because each wind speed bin contains a uniform distribution of relative wind directions, the precision curve in Figure 23 contains the cross-talk from all wind directions. Given that the wind speed signature is steeper at higher wind speed, one might expect the precision error in Figure 23 to drop at high wind speeds, but the increasing wind direction signal and cross-talk there probably moderates this effect.

6.3.5. Stratification by Faraday Rotation

The 20 km wind speed EDR algorithm uses only 18-36 GHz channels. Because Faraday rotation has an inverse-square frequency dependence, it is 32%, 20%, and 9% of the 10.7 GHz value at 18.7, 23.8, and 36.5 GHz, respectively. Therefore, one should not be surprised to find that residual Faraday rotation is not a problem for the wind speed EDR. The following figure (TO BE ADDED) shows the wind speed precision stratification by Faraday rotation. Sensitivity of the accuracy error to Faraday rotation (not shown) is just as flat. We expect the wind speed errors to meet the EDR error thresholds even under conditions of magnetic storms, where the Faraday rotation value used in the SDR cross-polarization correction will not be accurate.

6.4. Performance of the Wind Vector Algorithm

6.4.1. Description of Results

In this section, we describe the performance of the wind vector algorithm by itself—that is without the median filter, which will be described in Section 6.5. This means that the wind vector results can only be shown for the first rank wind direction ambiguity (the ambiguity that best fits the input TBs), and the closest ambiguity to the true wind direction.

The wind vector ambiguities consist of an associated pair of wind speed and wind direction values. It is important to report the wind speed with the direction, so that vector interpolation can properly be used in remapping the retrieval results to other grids. Despite the fact that we have a wind speed EDR algorithm that meets all of the SRD requirements (the 20 km wind speed EDR), the wind speed reported with the wind direction de facto becomes part of the wind vector—we insist on reporting it for all wind direction ambiguities, even though, due to the 56 x 35 km composite cell size, it is unlikely to meet the wind speed horizontal cell size requirement. Do differentiate it from the 20 km wind speed, we often refer to this wind speed at the low resolution wind speed ("LR wind speed").

Therefore, LR wind speed as well as wind direction performance will be assessed in this section. But do not confuse the performance of LR wind speed with that for the 20 km wind speed in the previous section! The LR wind speed that will be reported here is for the first rank wind direction ambiguity. However, there is no significant difference between the performance of the LR wind speed for the first ranked and the closest ambiguities.

ATBD for CMIS
Ocean EDR Algorithm Suite
Sea Surface Temperature EDR
Sea Surface Wind Speed/Direction EDR
Surface Wind Stress EDR

14-110

This document is intended for non-commercial use only. All other use is strictly forbidden without prior approval of the U.S. Government.

6.4.2. Conditions of Algorithm Testing

The uniform wind speed radiosonde test data set is used to assess performance, so as to provide enough high wind speed ocean scenes to collect accurate statistics there.   All sensor errors are included at requirements level using the sensor error model described above. The effective NEDTs are those for a 56 x 35 km composite cell size, average values of which are shown in Table 12. A calibration of the TBs to the RTM is assumed, and it simulated using the calibration model described in 6.1.2.

6.4.3. Binning of Retrieval Errors

Retrieval errors are binned in 2 m/s intervals in wind speed. However, the first bin contains just 0-1 m/s. No performance results are shown for the wind direction when the truth wind speed less than 3 m/s. However, in the case of low winds, the LR wind speed reported with the wind direction ambiguities does not depart significantly from the regression result used to seed the ambiguity search, and therefore its error statistics are reported for all wind speeds.

6.4.4. Performance

6.4.4.1.   Wind Direction

The performance of the wind direction component of the algorithm is shown in Figure 25, for both the first ranked ambiguity and the closest ambiguity to the true wind direction. The closest ambiguity results are the theoretical limit to how well any ambiguity removal algorithm (including our median filter) can perform when coupled with this particular wind direction algorithm.

The high wind direction precision error at low wind speeds and the rapid drop toward larger wind speeds is simply a result of the dependence of the wind direction signal on wind speed (Figure 4 through Figure 7). At low wind speeds, the NEDTs and the noise component of the sensor errors combine to yield an effective TB noise that is a considerable fraction of the peak to peak amplitude of the wind direction signal in any given channel. If one looks at the minima for each term in the χ^2 (equation (4.19)), one finds that the minima for different channels do not "line up" well with respect to the first ranked ambiguity; the minima of the χ^2 are wide and flat, and changing the NEDT added to any one channel can perturb the location of the χ^2 minima in a significant way. As wind speed and consequently the wind direction signal grow, the TB noise has less of an impact on the minima in the individual terms in the χ^2, and the minima that correspond to the first ranked ambiguity begin to line up well; thus, the ambiguities are defined by deep, narrow wells in the χ^2, and changing the NEDT added to any one channel has a minimal effect on the locations of the minima of the χ^2.

Clearly, if we increased the composite footprint size for the wind direction retrieval, we would reduce the effective NEDTs by averaging more measurements together; we would obtain better performance with respect to the truth wind direction used to simulate the TBs. But, in practice, this would increase the chance that the wind direction signal will change significantly over the footprint; in effect, one is then averaging (smoothing) equations (3.71) over a wider range of wind directions, and reducing the peak to peak amplitude of the wind direction signal in

the measurements relative to that in the model function. As a practical matter, increasing the composite footprint size also increases the spatial error between the measurements and ocean buoy or scatterometer wind directions to be used during the Cal/Val period.

Therefore the composite footprint size was chosen as the minimum size which results in the closest ambiguity precision meeting a 20 degree requirement with a margin of a couple of degrees. (We felt that eventually, the accuracy and precision requirements would be switched so that the precision requirement would be 20 degrees).

Given this footprint size, the first rank wind direction precision is 41 degrees in the 3-5 m/s bin, crosses 20 degrees at about 8 m/s, and thereafter reaches a minimum of about 13 degrees for wind speeds above 15 m/s. One does not see a further decrease in wind direction precision errors, because the amplitude of the wind direction signals in our model have flattened as a function of wind speed at or below 15 m/s.
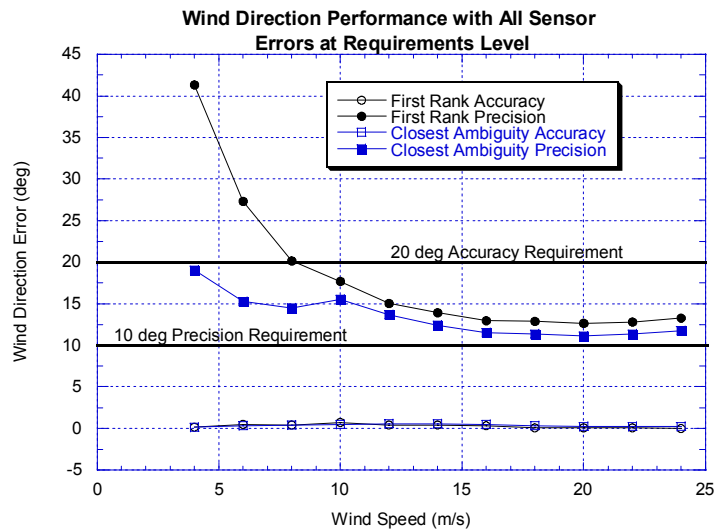
Figure 25: Performance of the wind direction component retrieved by the wind vector algorithm.

As we expect, the wind direction accuracy error is extremely small. Both TB biases and noise have the effect of pushing the ambiguities toward small relative wind directions over half of the range, and toward larger relative wind directions over the other half. (To see this, plot a 2-term harmonic series of your choosing (the wind direction signal) and draw a horizontal line that intersects the plot (TBs measurement). The intersections of the line with the plot give the ambiguities. Draw another horizontal line not too far from the first, and notice how the ambiguities shift.) Since each wind speed bin contains retrievals from all wind directions, the net effect of the biases and noise is zero. It is only when one plots the wind direction retrieval bias vs truth wind direction that one sees the effect of TB biases on the wind direction retrieval. We show these plots in the next section.

The kink in the closest ambiguity precision at 10 m/s remains unexplained. It may be a result of modeling error in the atmospheric parameter regressions as they attempt to handle the

flattening of the h-pol wind direction signal there. On the other hand, we find that if we scale down the polarimetric wind direction signal alone, the kink becomes larger, and eventually appears in the first rank wind direction precision as well.

Notice that the precision curves for the first rank and closest ambiguity move close together toward higher wind speeds. This is a result of the closest ambiguities that would be obtained from each channel moving closer together as the wind direction signal steepens. The "skill" of the algorithm is defined as the percentage of observations for which the first rank ambiguity is the closest ambiguity to the wind direction. The explanation of the precision curves moving close together is then that the skill is higher at higher wind speeds. We do not collect skill statistics for every wind speed bin in the radiosonde data sets. However, the algorithm does report skill in the 3-5 m/s bin (76 %) and in a 5-25 m/s bin (85%). Skill statistics for the NCEP-orbit data sets are shown for each 2m/s bin in the next section.

6.4.4.2.   Low Resolution Wind Speed

The performance of the low resolution wind speed that corresponds to the first rank ambiguity appears in Figure 26. The results for the wind speed that corresponds to the closest ambiguity to the true wind direction differs insignificantly (less than 0.02 m/s) from the results in the figure. The wind speed accuracy curve has the same general shape as that for the 20 km wind speed. The first guess wind speed, W_{est}, has a precision of about 0.75 m/s at all wind speeds, about the same as the precision shown in the figure for wind speeds less than 3 m/s. However, for wind speeds above 3 m/s, the χ^2 minimization improves on the first guess wind speed by allowing it to vary until the best fit to the TBs is found. That is, allowing the wind speed to be defined simultaneously by the isotropic and the wind direction signal improves the result. The precision continues to drop until the wind direction signal has flattened out as a function of wind speed; when this happens the wind direction signal is of no more use in defining the wind speed, and the algorithm is again depending mainly on the isotropic signal.

It is clear that the low resolution wind speed meets the accuracy and precision objectives when compared to the truth value of the wind speed in the test datasets. It is therefore likely that it will also meet those requirements with respect to the uniform average of wind speed over a 56 x35 km square (size of the 3 dB composite footprint). But, when fronts or other disturbances can make the characteristic length for wind speed variation considerably smaller than these dimensions, and therefore we do not claim that the low resolution wind speed will meet the accuracy and precision requirements with respect to the 20 km Horizontal cell size requirement. It is, however, a necessary component of the wind vector when interpolation of retrieved wind vectors from the scan geometry to another cell geometry is to be performed.
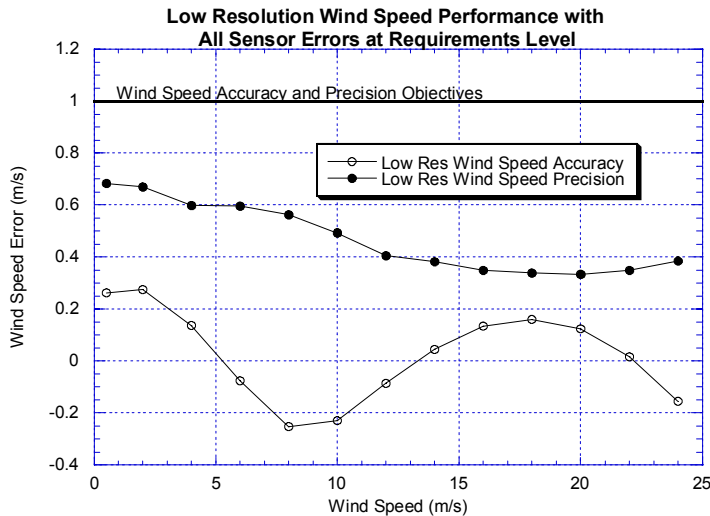
Figure 26: Performance of the Low Resolution Wind Speed

A comparison of both the wind speed and wind direction ambiguity performance to the SRD requirements is shown in Table yy. Note that, because the accuracy and precision requirements have not been switched, neither the first ranked nor the closest ambiguity wind direction precision meet the SRD requirements, while the accuracy requirement is met with 95% margin with respect to wind speed bins. As will be shown in the stratification of the next section, the maximum accuracy error with respect to the 18 degree wind direction bins is 9 degrees.

Table 20: Comparison of Wind Vector EDR Performance to SRD Requirements

Paragraph Number	Description	Threshold	Objective	Performance
C40.2.5-1	a. Horizontal Cell Size	20 km	1 km	56 x 35 km
C40.2.5-2	b. Horizontal Reporting Interval	(TBD)	(TBD)	
C40.2.5-3	c. Horizontal Coverage	Oceans	Oceans	Oceans
	d. Measurement Range			
C40.2.5-4	1. Speed	3-25 m/s	1-50 m/s	0-25 m/s for wind speed 3-25 m/s for wind direction
C40.2.5-5	2. Direction	0-360 deg	0-360 deg	0-360 deg
	f. Measurement Accuracy			
C40.2.5-6	1. Speed	2 m/s or 20% of true value, whichever is greater	1 m/s or 10% of true value, whichever is greater	-0.25 to 0.28 m/s 0.28 m/s maximum <0.20 m/s typical 0.02 m/s overall
C40.2.5-6	2. Direction	20 deg for wind speeds greater than	10 deg	-0.7 to 0.1 deg 0.7 deg maximum

ATBD for CMIS
Ocean EDR Algorithm Suite
Sea Surface Temperature EDR
Sea Surface Wind Speed/Direction EDR
Surface Wind Stress EDR

14-114

This document is intended for non-commercial use only. All other use is strictly forbidden without prior approval of the U.S. Government.

		5 m/s. 20 deg (TBR) for wind speeds from 3-5 m/s.		<0.4 typical 0.3 deg overall
	g. Measurement Precision			
C40.2.5-8	1. Speed	1 m/s	1 m/s	0.33 to 0.68 m/s 0.68 m/s maximum <0.60 m/s typical 0.02 m/s overall
C40.2.5-9	2. Direction	10 deg	10 deg	First Rank: 41 deg (3-5 m/s) 27 deg (5-7 m/s) 20 deg (7-9 m/s) 13 deg (high W) Closest Ambiguity 19 deg (3-5 m/s) 15 deg (5-7 m/s) 14 deg (7-9 m/s) 12 deg (high W)
C40.2.5-10	h. Mapping Uncertainty	5 km	1 km (TBR)	
C40.2.5-11	i. Swath Width	1700 km (TBR)	3000 km (TBR)	>1700 km

If the accuracy and precision requirements were switched, then we would meet both requirements with respect to the closest ambiguity wind direction; we would also meet the precision requirement for the first ranked ambiguity for wind speeds greater than 8 m/s, and the accuracy requirement everywhere.

One expects that when the first data from a radiometer is taken, the biases in the TBs with respect to the RTM will cause large biases in the EDRs. But the purpose of the calibration to the RTM, which we consider a necessary step in obtaining optimal performance, removes the large biases in the TBs, and therefore also in the retrievals. On the other hand, one can do nothing to decrease the noise in the TBs. In this way, the bias errors in the EDRs are made to be much smaller than the standard deviation error. Therefore, we have difficulty in understanding why the accuracy requirement has been set quite loose, but the precision requirement set below what can be obtained with state-of the-art NEDTs and a reasonable composite footprint size.

6.4.5. Stratification with Respect to Other Geophysical Parameters

Figure 27 shows the stratification of the low resolution wind speed "Wind LR" and the first rank "PHI(1)" and closest ambiguity "PHI(C)" wind directions for the test data set. These are the standard "cross-talk plots" shown previously for other ocean EDRs. The wind speed stratification is qualitatively the same as for the 20 km wind speed EDR, and the explanation of the features found in this stratification can be found in the 20 km wind speed stratification section. The one difference between the low resolution wind speed and the 20 km wind speed is that the wind direction cross-talk has become smaller. The main difference between the two algorithms being the use of the 10 GHz channels, and the ability of the low resolution wind speed

ATBD for CMIS
Ocean EDR Algorithm Suite
Sea Surface Temperature EDR
Sea Surface Wind Speed/Direction EDR
Surface Wind Stress EDR

14-115

This document is intended for non-commercial use only. All other use is strictly forbidden without prior approval of the U.S. Government.

to be defined by the wind direction signal as well, we feel that these two effects give rise to the lowered cross-talk.

The wind direction vs wind speed plots are just a repetition of the plots shown in the last section. Remember that each bin in every other cross-talk plot contains all wind speeds, and thus the overall precision is about 30 degrees (for this uniform distribution in wind speeds). In terms of the bias error, there seems to be very little cross-talk from SST, water vapor, or cloud liquid water. However, we expect the wind direction precision to rise as a function of water vapor, due to the attenuation of the wind direction signal by the decreasing atmospheric transmission at all frequencies as water vapor increases. The same is true of the cloud liquid water response, but to a lesser degree, because it mainly changes the transmission for the 36 GHz channels.
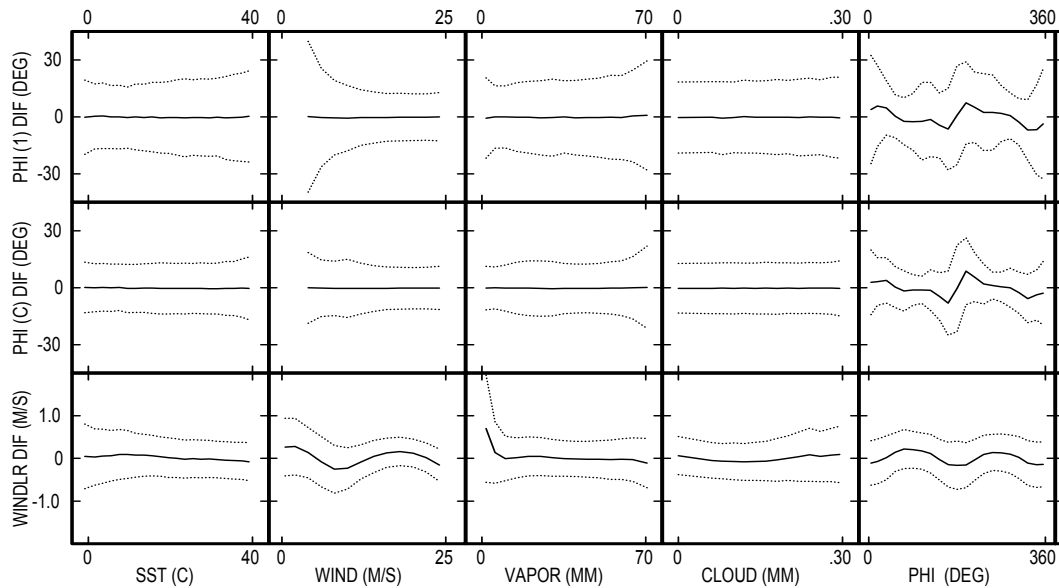
Figure 27: Wind Vector EDR Error Stratification

The wind direction accuracy vs wind direction plots are anti-symmetric about 180 degrees. (A negative bias indicates the true wind direction is larger than the retrieved wind direction while a positive bias indicates the opposite). The precision plots are symmetric about 180 degrees. Re-plotting to show the accuracy and precision errors individually as in Figure 28 shows these symmetries clearly. The symmetry properties reflect the symmetry of the harmonic terms in the expression for the wind direction emissivity signal.
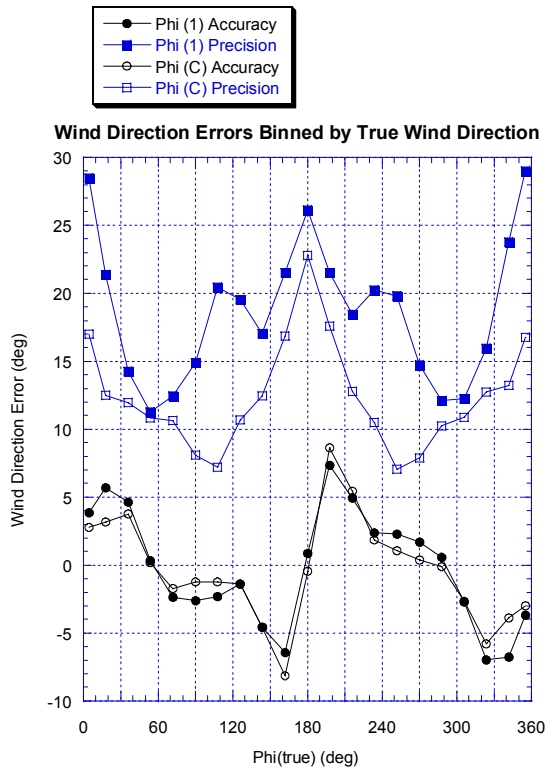
Figure 28: Symmetry Properties of the Wind Direction Errors

As in scatterometry, certain wind directions are more difficult to retrieve than others. Here, the precision plots show that relative wind directions of 0 and 180 (upwind and downwind) are the most difficult to retrieve. Why this is the case becomes clear when one plots the wind direction emissivity signal as a function of wind speeds, as in Figure Z. Note the small oscillations in the xx polarizations near 180 degrees and the flatness in the yy polarizations near 0 degrees, and consider the ambiguities that would be retrieved using the one of the v,h,U, or 4 polarizations. If the true wind direction is 180 degrees, then any perturbation to the TBs for the xx polarized TBs will cause the TBs to be out of the range of brightness temperatures in the center oscillations, and throw the ambiguities to much larger and smaller wind directions. For the yy polarizations and true wind directions around zero degrees, the flatness of the signal causes a small perturbation to the TBs to cause a large change in the ambiguities; at zero degrees, a single ambiguity then bifurcates into two.

When selecting the closest ambiguity to the true wind direction, the problem around 180 degrees is worst, because of the distance of any ambiguity from the true wind direction. When selecting the first rank ambiguity, the problem around zero degrees is most potent, because the flatness of the curve combined with the NEDTs lower the ability of the algorithm to select as the first rank ambiguity the closest ambiguity to the true wind direction (i.e. lowers the skill, as shown in figure zz.

The explanation for the anti-symmetry in the first ranked ambiguity bias is as follows. For a given true wind direction jtrue between about 115 and 245 degrees, the set of retrieved ambiguities usually contains one ambiguity that is fairly close to jtrue (call it ja), and another ambiguity that is reflection symmetric about 180 degrees to ja (call it jb). This is clearly seen in

Figure 7, and results from the deep V-shaped groove symmetric about 180 degrees in the c2 contours. These two ambiguities are often very close in their c2 values. That is the noise in the TBs can cause jb to be selected as the first rank ambiguity. When jtrue is less than 180 degrees, jb is greater than 180 degrees, and the bias is positive.

6.5. Performance of the Median Filter Algorithm

6.5.1. Conditions for Algorithm Testing and Limitations on Performance Assessment

6.5.1.1. Test Data Sets

The MF is tested using the NCEP test orbits 1-4 from Table 14 and the cloud water profiles created from SSM/I retrievals as per Section 5.5.5. That means we are limited to the regions were SSM/I cloud retrievals are available. We also filter the NCEP-orbit test data for cases where the SSM/I columnar cloud water exceeds 0.3mm. No median filtering is performed for wind speeds below 3 m/s. As explained in section 5.5.2, we run the MF on a scan based grid. For the MF we are using every 4th observation from every 2nd scan, i.e. we use 75 observations per scan and a total of 1600 scans per orbit. This corresponds to a grid spacing of about 25 km along track and along scan. A smaller grid spacing would result in an unnaturally smooth wind field. After excluding pixels with low wind speeds and high liquid cloud water, the number of wind vector retrievals used in the MF is therefore roughly 50,000 per orbit.

6.5.1.2. Sensor Errors and Wind Direction Retrieval

Before the median filter is run, the wind direction ambiguities must be retrieved for each gird point in the NCEP-orbit test data. For the retrievals, NEDTs are added to the TBs for the NCEP-orbit test data, as discussed in section 4.5.2.2 and shown in Table 12.

We use the same algorithm to retrieve wind direction for the NCEP-orbit and radiosonde test data. But, the actual code has departed somewhat from the code used with the radiosonde test data sets. First, there are differences due to the necessity of handling wind fields and geographical data from the orbit simulator, and supplying the necessary data to the median filter. Second this code has been used for algorithm development, since we want to see the effect of algorithm changes on the median filter results. Changes which improve performance are then added to the copy that performs retrievals on the radiosonde data. In the meantime, the code that that performs retrievals on the radiosonde data was adapted for use with the sensor error model code, and used to derive the sensor error requirements.

In summary, NCEP-orbit retrieval code is the experimental code. Successful experiments are transferred to the radiosonde data retrieval code. However, the NCEP-orbit retrieval code has not been adapted for use with code for the sensor error model; the TBs for NCEP-orbit wind direction retrievals do not contain the polarization rotation nor cross polarization control or knowledge errors, no SDR algorithm is applied, and no calibration to the RTM is simulated.

ATBD for CMIS   14-118   This document is intended for non-commercial
Ocean EDR Algorithm Suite   use only. All other use is strictly forbidden without
Sea Surface Temperature EDR   prior approval of the U.S. Government.
Sea Surface Wind Speed/Direction EDR
Surface Wind Stress EDR

Besides the NEDTs, there is one sensor error that is relatively easy to model in the NCEP-Orbit wind direction retrievals. The earth incidence angle variation is included automatically in the orbit simulator, which uses an oblate earth model. We do add an EIA knowledge error to the EIA reported by the orbit simulator.

Essentially, we attempt to model the effect of all sensor errors on the NCEP-orbit wind direction retrievals by raising the EIA knowledge error noise to the point where the first rank wind direction precision is identical to that for wind direction retrievals using the radiosonde data and with the sensor error model. In this way we insure that we are not feeding the median filter wind direction ambiguities with an overly optimistic retrieval errors.

6.5.1.3.   Regressions and Wind Direction Retrieval

There is one other difference in the wind direction retrieval for the NCEP-orbit data that affects the performance of the algorithm. The SST, wind speed, and atmospheric parameter regressions necessary for the retrieval were trained using the NCEP-orbit training data. This training data does not span the required range of the geophysical parameters (Figure 17), the Rayleigh wind speed distribution emphasizes the low wind speeds, and the correlation between the SST and water vapor is strong. The paucity of high wind speeds in the training data means that that the regressions begin to show bias at the larger wind speeds, resulting in a bias in the first rank wind direction retrieval for high wind speeds that is not seen in the radiosonde test data set retrievals. We will see this bias in the performance figures.

The original reason we decided to train the regressions this way was to see how the wind direction retrievals and median filter performed when the regressions were trained using data with the same geophysical distributions as the test data. We will update the regression coeficients to those trained from the radiosonde data as soon as possible.

6.5.2. Convergence of the MF

It takes about 8-10 iterations of the MF to reach the termination condition (4.22). During the first pass about 3000 out of approximately 50,000 wind vectors per orbit are changed (6%). The number of changed fields decreases in each step. During the last step before termination, only about 50 wind vectors are changed (0.1%).

6.5.3. Experiment with Nudging

Scatterometry frequently uses a technique known as *nudging*. Here a median filter is not initialized with the first ranked ambiguity, i.e. the ambiguity with the lowest χ^2 , but with the ambiguity that is closest to a wind field obtained from a numerical weather prediction (NWP) model. The hope in doing so is that highly erroneous areas, which might be present in the first ranked ambiguity, do not spread out during the median filtering process. In scatterometry, the two leading ambiguities are approximately 180 deg apart and therefore the precision error of the first ranked ambiguity can be very poor.

We have investigated the use of nudging with our median filter. It is important to take a different GCM for nudging than the one that has been used for the brightness temperature simulation. Otherwise, one would initialize the median filter with the true wind field getting as output basically the closest ambiguity: an unrealistically good result. In our experiment, we performed the nudging with a wind field from the NCEP/NCAR reanalysis, which is run 4 times daily at a 2.5 deg grid resolution.

We found that when nudging is used, fewer wind vectors are changed during MF procedure. Only about 500 vectors change during the first step in a nudging run, whereas 3000 changed without nudging. The reason is obviously that the initial wind field is already very smooth if nudging is used, so that the MF smoothing has little further influence.

However, the global wind direction errors for the nudged median filtered wind fields were no better than those where the median filter was applied without nudging, and in fact were a little worse. We hypothesize that this was due to the resolution of the nudging field (2.5 times larger than the NCEP-Orbit wind fields); the nudging created a very smooth wind field, which the median filter found little reason to change. We would expect the same to be true with operational data; the composite footprint size and the horizontal reporting interval of the retrievals is much smaller than the resolution of the GCM wind fields that could be used in nudging.

Given the poor performance and the additional external data that would be required, we decided <u>not</u> to use nudging in the wind vector post processing for CMIS.

6.5.4. Binning of Retrieval Errors

The wind direction errors for the MF are binned with respect to 2m/s increments in wind speed. Table 21 shows the wind speed bins and their populations.

Table 21: Number of valid pixels in wind speed bins (Orbit 1 through 4 test data).

W Bin $\left[\frac{m}{s}\right]$	(3,5)	(5,7)	(7,9)	(9,11)	(11,13)	(13,15)	(15,17)	(17,19)	(19,21)	(21,23)	(23,25)
#	32,315	53,527	50,558	25,208	16,685	8,938	3,014	1,333	569	246	143

Table 21 shows that the population of the wind speed bins above 19 m/s is very low. This happens despite the fact that we had applied the scaling transformation (5.6) to the NCEP Orbit wind speeds. This will result in certain biases for the retrieved wind vector in these higher wind speed bins.

6.5.5. Performance

6.5.5.1.   Retrieval Errors

ATBD for CMIS
Ocean EDR Algorithm Suite
Sea Surface Temperature EDR
Sea Surface Wind Speed/Direction EDR
Surface Wind Stress EDR

14-120

This document is intended for non-commercial use only. All other use is strictly forbidden without prior approval of the U.S. Government.

Table 22 shows wind speed and wind direction performance for retrievals on the NCEP-Orbit wind fields. We include the first rank and closest ambiguity performance, but only so that they can be compared to the performance on the radiosonde test data sets in section 6.4.4. Except for the median filter performance ("selected ambiguity"), none of the data in Table 22 should be considered the performance for wind direction or wind speed. The wind direction and wind speed performance for the first ranked and closest ambiguities is contained in Table 20 of section 6.4.4.

Table 22: Comparison of Wind Vector EDR Performance including the MF to SRD Requirements

Paragraph Number	Description	Threshold	Objective	Performance or Comment
C40.2.5-1	a. Horizontal Cell Size	20 km	1 km	56 x 35 km
C40.2.5-2	b. Horizontal Reporting Interval	(TBD)	(TBD)	Every 4th observation, every other scan to give 25 km interval (see section 4.5.2.6)
	d. Measurement Range			
C40.2.5-4	1. Speed	3-25 m/s	1-50 m/s	NCEP retrievals for the MF use only 3-25 m/s observations
C40.2.5-5	2. Direction	0-360 deg	0-360 deg	0-360 deg
	f. Measurement Accuracy			
C40.2.5-6	1. Speed	2 m/s or 20% of true value, whichever is greater	1 m/s or 10% of true value, whichever is greater	Selected Ambiguity 0.8 m/s max (high wind speeds—see section 6.5.1.3) <0.2 m/s at lower wind speeds -0.06 m/s overall
C40.2.5-6	2. Direction	20 deg for wind speeds greater than 5 m/s. 20 deg (TBR) for wind speeds from 3-5 m/s.	10 deg	First Rank: -3.5 to 1.7 deg 0.8 deg overall Closest Ambiguity -2.2 to 1.2 deg 0.4 deg overall Selected Ambiguity: -2.2 to 1.4 deg 0.6 deg overall
	g. Measurement Precision			

C40.2.5-8	1. Speed	1 m/s	1 m/s	0.50 maximum 0.37 m/s overall for selected ambiguity
C40.2.5-9	2. Direction	10 deg	10 deg	<u>First Rank:</u> 36 deg (3-5 m/s) 22 deg (5-7 m/s) 17 deg (7-9 m/s) < 9 deg (high W) <u>Closest Ambiguity</u> 14 deg (3-5 m/s) 11 deg (5-7 m/s) 10 deg (7-9 m/s) < 9 deg (high W) <u>Selected Ambiguity:</u> 17 deg (3-5 m/s) 13 deg (5-7 m/s) 11 deg (7-9 m/s) < 9 deg (high W)
C40.2.5-11	i. Swath Width	1700 km (TBR)	3000 km (TBR)	We use the entire 1700 km swath in the orbit simulator

The results for the biases and standard deviations as function of wind speed are displayed in Figure 29 for the wind direction and in Figure 30 for the wind speed. The corresponding skill rates are shown in Figure 31.
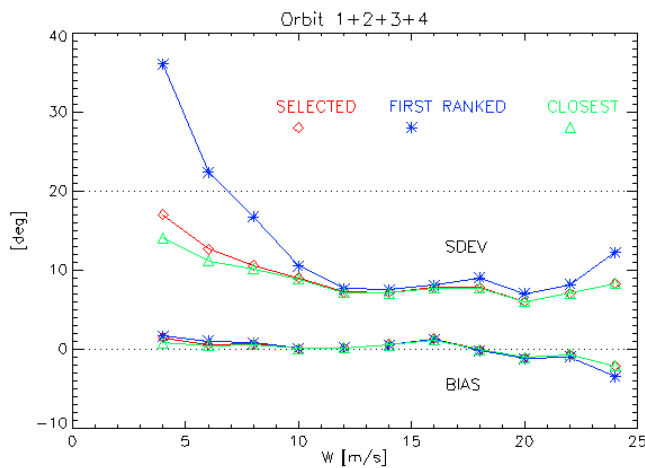
Figure 29: Wind direction retrieval statistics (Orbit 1-4).

ATBD for CMIS
Ocean EDR Algorithm Suite
Sea Surface Temperature EDR
Sea Surface Wind Speed/Direction EDR
Surface Wind Stress EDR

14-122

This document is intended for non-commercial use only. All other use is strictly forbidden without prior approval of the U.S. Government.
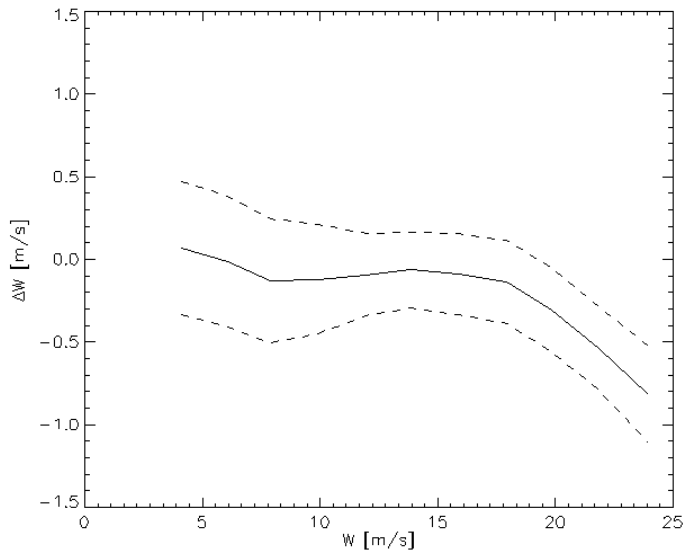
Figure 30: Statistics for the wind speed selected by the MF (Orbit 1-4).
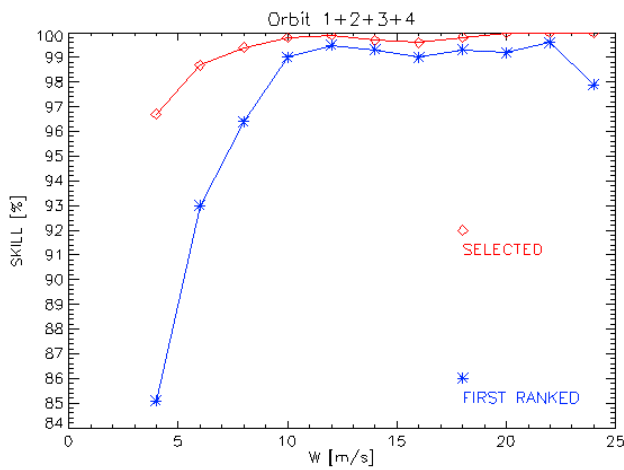
Figure 31: Skill statistics (Orbit 1+2+3+4).

Table 23 shows the occurrence rate for each individual ambiguity $k = 1, 2, 3$. The 4th ambiguity is never either closest or selected.

Table 23: Occurrence rates for closest and selected ambiguity (Orbit 1-4). k denotes the ranking of the ambiguities.

Closest k	Selected k	Occurrence (%)
1	1	93.8
1	2	0.49
1	3	0.01

2	1	0.58
2	2	4.71
2	3	0.01
3	1	0.02
3	2	0.01
3	3	0.30

6.5.5.2.   Selected Cases of Retrieved Wind Fields

Figure 32, Figure 33 and Figure 34 display 3 typical cases how the median filter mechanism works, or, in certain cases fails. In each case we display the true wind field, the closest ambiguity, the 1st ranked + closest ambiguity and the selected + closest ambiguity. The grid contains 75 = 300/4 cells and 1600 = 3200/2 scans. Missing arrows in the figures correspond to pixels that are either over land or ice or contain a liquid cloud water larger than 0.3mm or contain an wind speed less than 3 m/s. The skill improvement that is achieved by the MF is evident in the figures by the decrease in the number of red arrows between the 3rd (1st ranked + closest) and 4th (selected + closest) panels. It demonstrates how much better the selected wind field (after MF) matches the closest wind field than the first ranked wind field (before MF) did.

Case 1 displays a cluster of wrongly selected first ranked wind fields (centered at around cell 72 and scan 488), which are all pointing in a similar direction. The MF is not able to break up this cluster. Actually, the size of the cluster even increases slightly after it is passed through the MF. The value of the wind speeds W in and near the cluster is approximately constant and it is obviously not possible that areas with larger wind speed (i.e. larger skill) can penetrate into the cluster. In contrast, Cases 2 and 3 demonstrate nicely how areas with large wind speeds and good skill can improve adjacent pixels with lower wind speeds and bad skill. This happens even in cases where the wind direction exhibits strong variations, such as near cyclones (Case 2) or frontal boundaries (Case 3).

ATBD for CMIS
Ocean EDR Algorithm Suite
Sea Surface Temperature EDR
Sea Surface Wind Speed/Direction EDR
Surface Wind Stress EDR

14-124

This document is intended for non-commercial use only. All other use is strictly forbidden without prior approval of the U.S. Government.
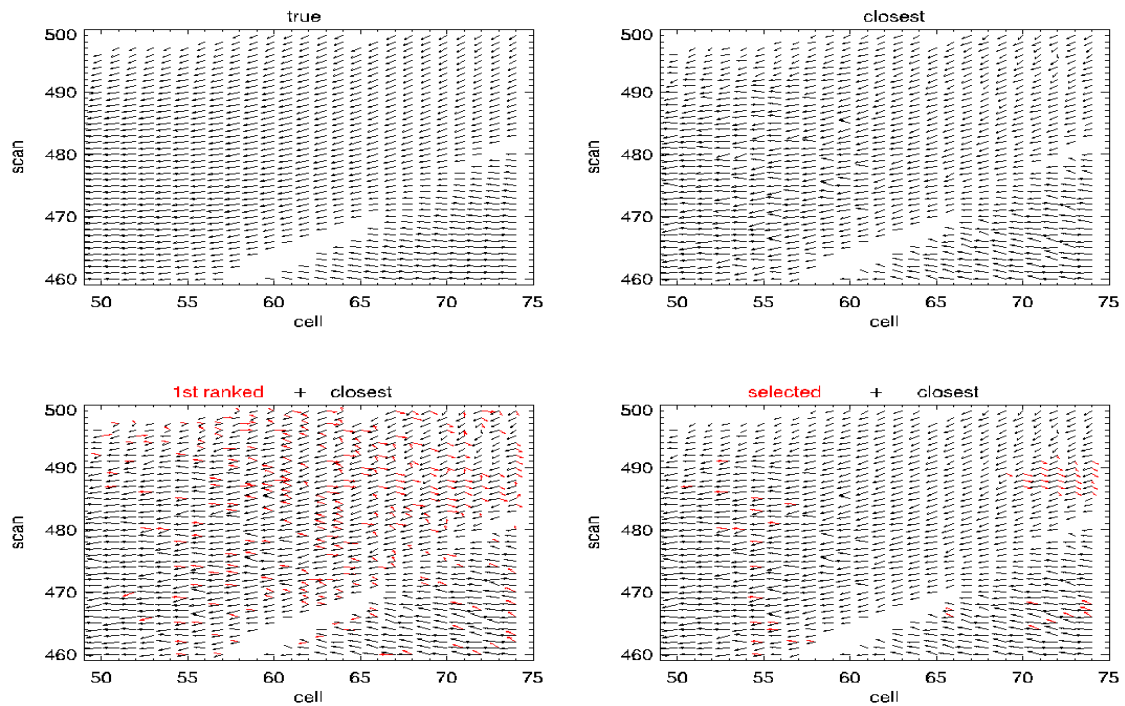
Figure 32: Case 1: True field, closest ambiguity, 1st ranked ambiguity, and field that is selected by the median filter (taken from Orbit 1).
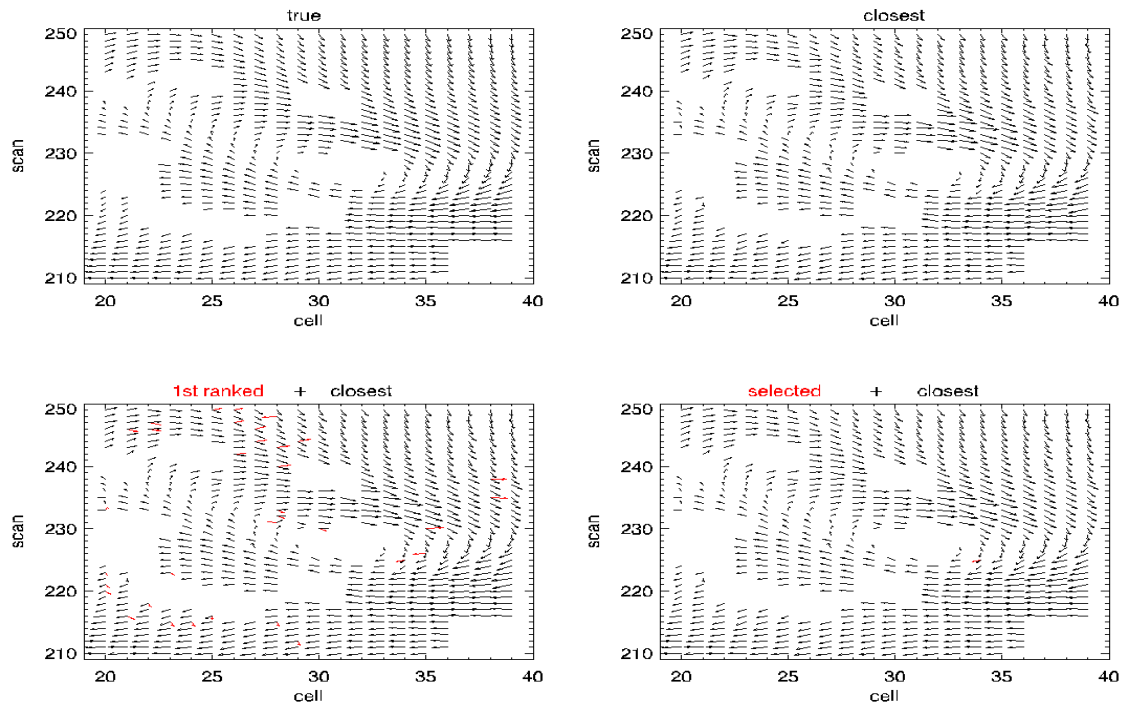
Figure 33: Case 2: (taken from Orbit 1).
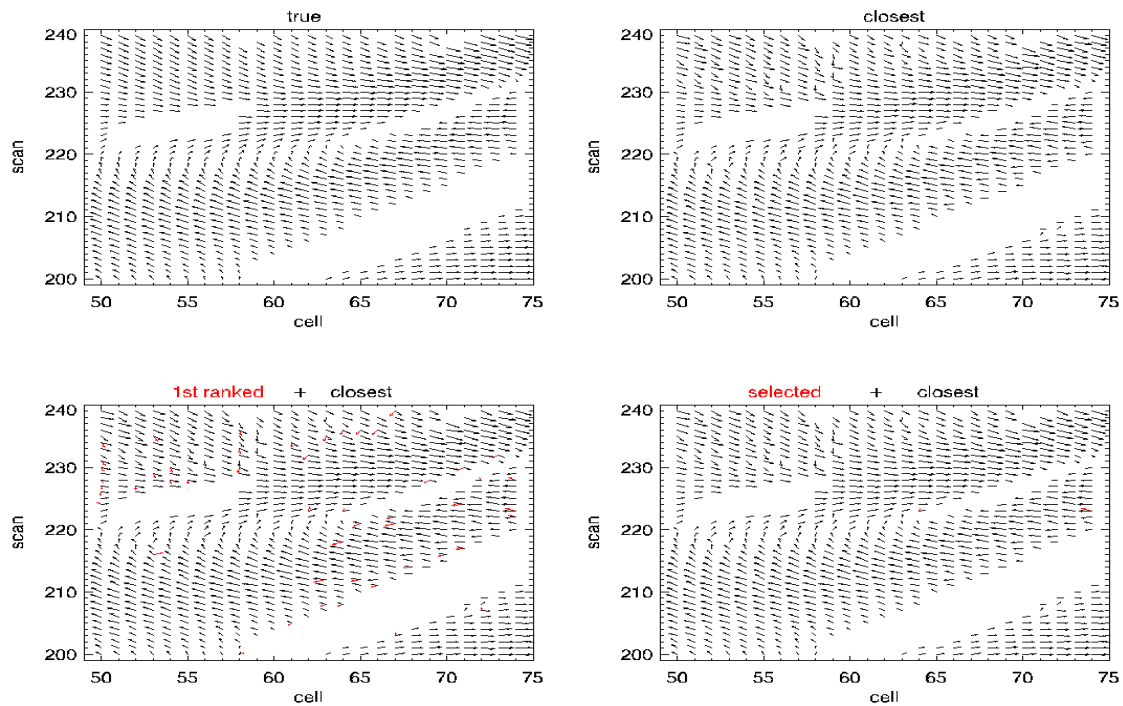
Figure 34: Case 3: (taken from Orbit 2).

6.5.6. Stratification by Other Geophysical Parameters
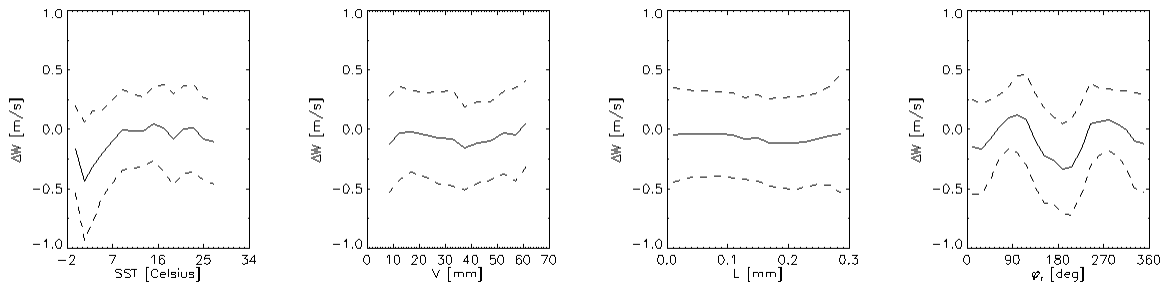
Figure 35: Error Stratification for Selected Wind Speed After Median Filtering.
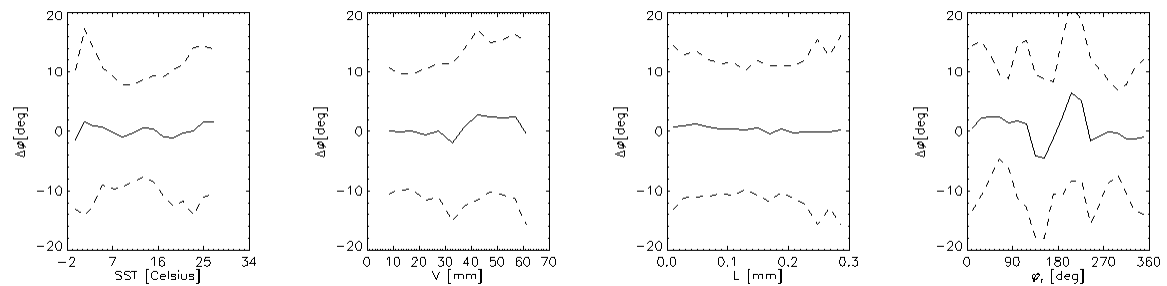
Figure 36: Error Stratification for Selected Wind Direction After Median Filtering.

The stratified errors with respect to SST, V, L and φ_r for the retrieved wind vector after MF are shown in   Figure 35 (for wind speed) and Figure 36 (for wind direction). If we compare with

ATBD for CMIS
Ocean EDR Algorithm Suite
Sea Surface Temperature EDR
Sea Surface Wind Speed/Direction EDR
Surface Wind Stress EDR

14-126

This document is intended for non-commercial use only. All other use is strictly forbidden without prior approval of the U.S. Government.

Figure 27, we recognize biases in the SST crosstalk plots at low values for SST both in Figure 35 and Figure 36. These biases can be regarded as artificial. They arise as a consequence of the small numbers of events in the training orbit data set (NCEP Orbit 0), as one can see in Figure 17. In case of the V crosstalk the bins with V < 5mm in the training set are so little populated that we have not computed any crosstalk statistics for these values of V.

Figure 37 shows the first ranked and selected skill of the retrieved wind direction with respect to φ_r. We notice that the first ranked skill is smallest for downwind observations. This is also consistent with the φ_r crosstalk of the retrieved wind direction in Figure 36 showing that the standard deviation of the error is largest for downwind observations. We attribute this to the wind direction of the 3rd Stokes parameter (Figure 4). Near downwind (φ_r = 180 deg) the curves are relatively flat. This means that small errors in T_B can cause large uncertainties in φ_r .
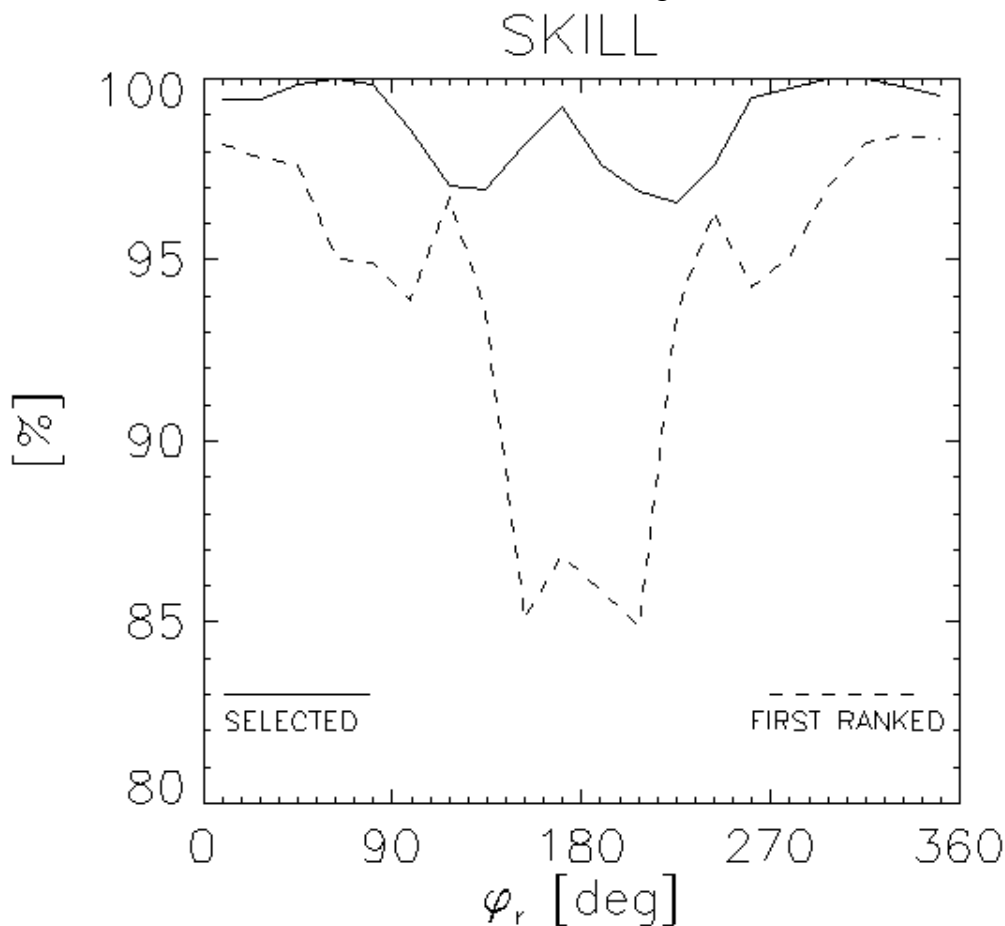
Figure 37: Stratification of First Ranked and Selected Skill With Respect to Relative Wind Direction.

6.6. Concerns With Regards to Wind Vector Retrieval

So far, the performance statistics for the wind vector retrieval has been evaluated with the wind direction corresponding to the full lines in Figure 5 - Figure 7. In the following, we refer to this signal as OLD signal. In section 3.7.6 we have already indicated that this signal is based on

ATBD for CMIS
Ocean EDR Algorithm Suite
Sea Surface Temperature EDR
Sea Surface Wind Speed/Direction EDR
Surface Wind Stress EDR

14-127

This document is intended for non-commercial use only. All other use is strictly forbidden without prior approval of the U.S. Government.

outdated data analyses. The most recent analyses have been performed by (Meissner and Wentz 2000) for V and H (long dashed lines in Figure 5 and Figure 6) and by (Yueh and Wilson 1999) for the 3rd and 4th Stokes parameters (short dashed lines in Figure 5 and Figure 6). Moreover, the analysis of (Meissner and Wentz 2000) suggests that both the V and H signals at 11 GHz have approximately 60% of their value at 19 GHz. We have applied the same scaling for 3rd and 4th Stokes parameter at 11 GHz. In the following, we refer to this signal as NEW SIGNAL.

In order to assess how the performance is affected if the NEW signal is used instead of the old, we have processed Orbit 1 for both cases for 4 m/s< W < 20 m/s and used a binsize of 1 m/s. Figure 38 shows the statistics (standard deviation) and Figure 39 the skill for both signals.
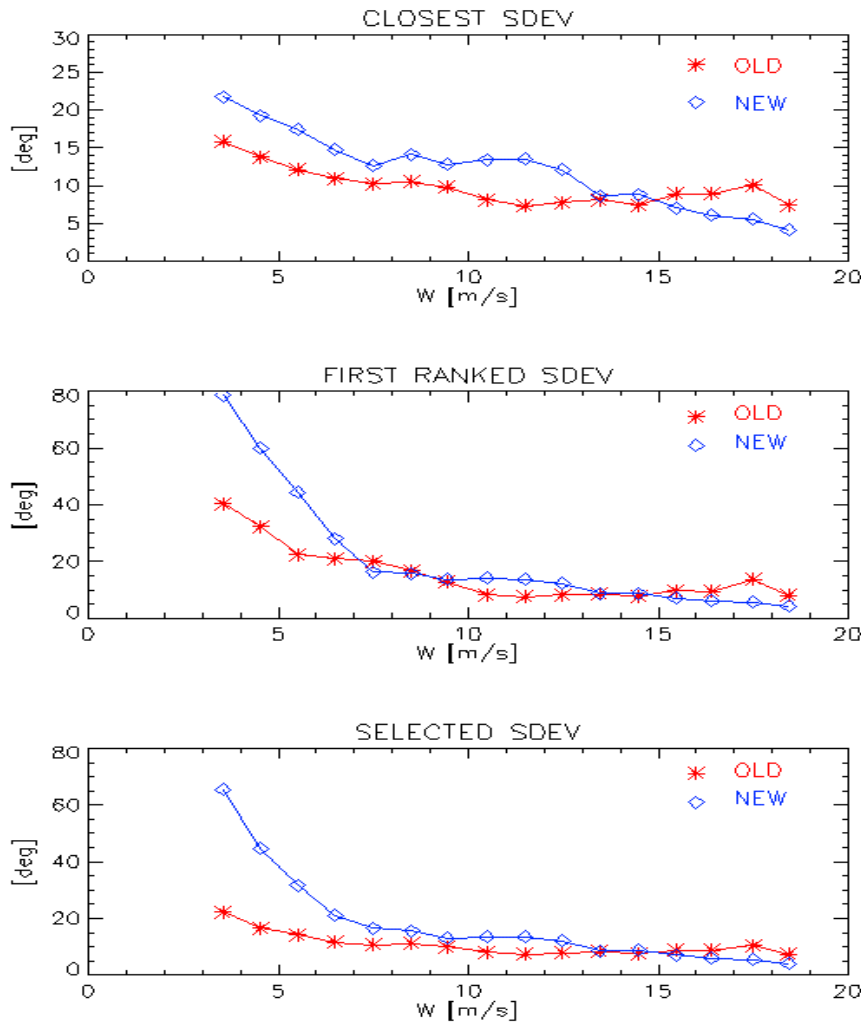
Figure 38: Retrieval statistics using old and new wind direction signal (Orbit 1).
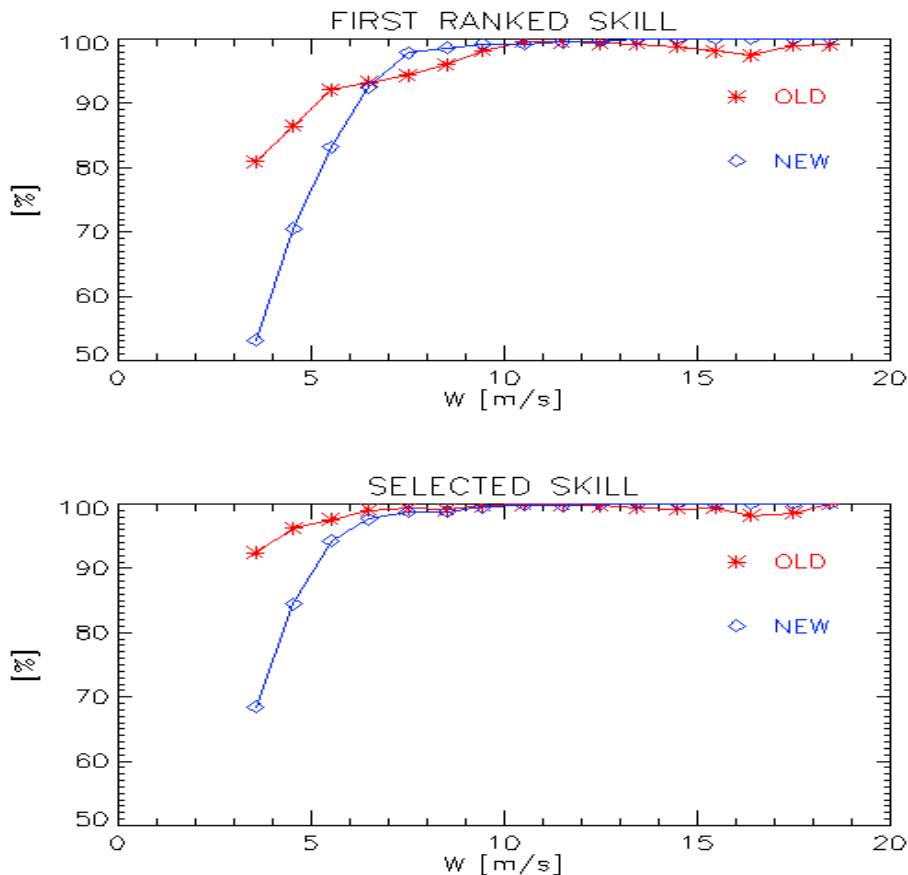
Figure 39: Skill statistics using old and new wind direction signal (Orbit 1).

We see that the performance is strongly degraded for wind speeds below 7 m/s. In these wind speed bins the retrieval error for the selected ambiguity is larger than 20 deg and the skill is corresponding low. This is no surprise, because the NEW is indeed much smaller than the OLD signal for low and intermediate wind speeds and is therefore getting swamped by radiometer noise. It should be noted that we have not yet optimized the MF for the NEW signal. Doing this optimization will likely improve the results somewhat. However, one needs to be aware that a CMIS wind direction retrieval will be probably very difficult for low and intermediate wind speeds with the NEW signal.

6.7. Performance of the Wind Stress Algorithm

6.7.1. Conditions for Algorithm Testing

ATBD for CMIS
Ocean EDR Algorithm Suite
Sea Surface Temperature EDR
Sea Surface Wind Speed/Direction EDR
Surface Wind Stress EDR

14-129

This document is intended for non-commercial use only. All other use is strictly forbidden without prior approval of the U.S. Government.

The wind stress algorithm uses the output of the 20 km wind speed EDR to produce a bulk estimate of wind stress. Therefore, the conditions for testing are the same as those for the 20 km wind speed EDR performance in Section 6.3.1.

6.7.2. Binning and Retrieval Errors

The wind stress retrieval errors are binned as a function of truth wind stress and truth wind speed. The wind speed bins are 2 m/s, except that the first bin contains only wind speeds from 0-1 m/s. The wind stress bins are 0.1 N/m2 wide. For the EDR error calculations, the true wind stress is determined by using iteration formulae of section 4.6.2 on the true wind speed. This allows us to include the wind stress error that results from interpolation of the coefficient of drag in the EDR error statistics.

6.7.3. Requirements Interpretation

The wind stress measurement range, accuracy, and precision requirements of the SRD say "consistent with sea surface wind speed." We interpret these to mean that the wind stress measurement range is sufficient to accommodate the wind speed range requirement, and that the wind stress accuracy and precision requirements are to be computed from the bulk formula for wind stress:

$$\tau = \rho_{air} C_{DN10} W_{N10}^2 \quad (6.27)$$

Defining the wind speed and stress accuracy requirements as ΔW_{req} and $\Delta \tau_{req}$, and the precision requirements as $\sigma_{W,req}$ and $\sigma_{\tau,req}$, we interpret the wind stress requirements as:

$$\Delta \tau_{req} = \rho_{air} \left(\frac{\partial C_D}{\partial W} W^2 + 2 C_D W \right) \Bigg|_{W_{true}} \quad \Delta W_{req} = \tau_{true} \left(\frac{\partial C_D / \partial W}{C_D} + \frac{2}{W} \right) \Bigg|_{W_{true}} \Delta W_{req} \quad (6.28)$$

and

$$\sigma_{\tau,req} = \rho_{air} \left\| \frac{\partial C_D}{\partial W} W^2 + 2 C_D W \right\|_{W_{true}} \quad \sigma_{W,req} = \tau_{true} \left\| \frac{\partial C_D / \partial W}{C_D} + \frac{2}{W} \right\|_{W_{true}} \sigma_{W,req} \quad (6.29)$$

Therefore, the SRD wind stress requirements imply requirements that are a function of wind speed or wind stress. The wind stress requirements are also a function of the assumed coefficient of drag. We use the C_D from the iterative computation of section 4.6.2 in order to define these requirements for each wind speed and wind stress bin; the results are plotted with the performance in the next section.

6.7.4. Performance

The performance of the wind stress EDR algorithm is shown in Figure 40 and Figure 41. The wind stress objective requirements, determined from equations (6.28) and (6.29), the wind speed requirements, and our model for CD, are also shown in the figures. Of course, the wind stress EDR meets the accuracy and precision objectives precisely because the 20 km wind speed meets the wind speed accuracy and precision objectives. Also wind stress exceeds the measurement range threshold because the 20 km wind speed exceeds the wind speed measurement range threshold.
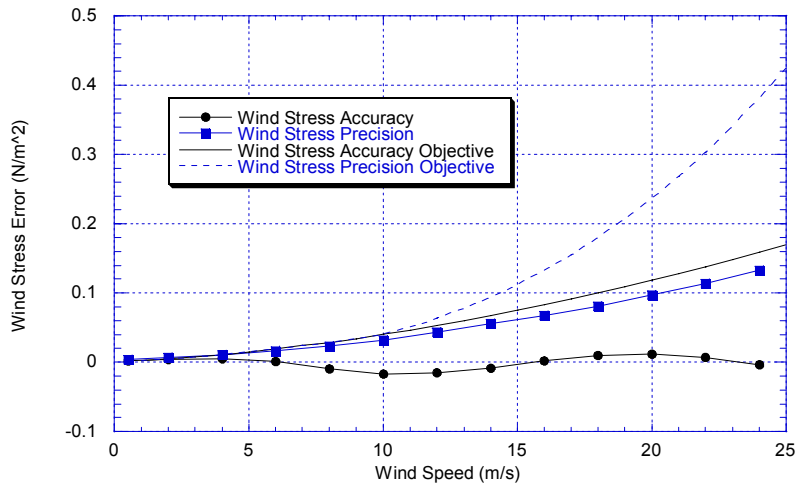
Figure 40: Wind Stress Performance as a Function of Wind Speed

ATBD for CMIS   14-131   This document is intended for non-commercial
Ocean EDR Algorithm Suite   use only. All other use is strictly forbidden without
Sea Surface Temperature EDR   prior approval of the U.S. Government.
Sea Surface Wind Speed/Direction EDR
Surface Wind Stress EDR

20 km Wind Stress Performance with All Sensor Errors at Requirements Level
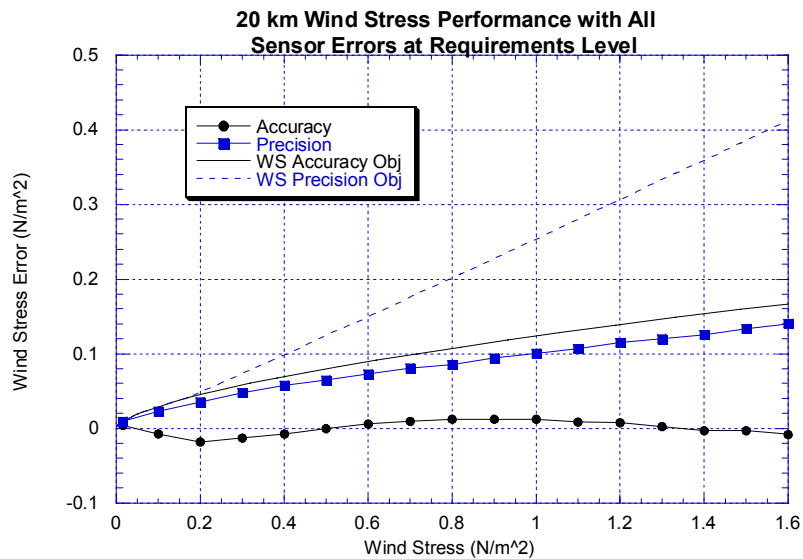
Figure 41: Wind Stress Performance as a Function of Wind Stress

The performance is compared to the SRD requirements in Table B. Because the 20 km wind speed is expected to meet the 20 km horizontal cell size threshold, we expect the wind stress to meet the 20 km horizontal cell size objective. In summary, the wind stress meets all EDR horizontal cell size and measurement objective requirements.

Table 24: Comparison of Wind Stress EDR Errors to SRD Requirements

Paragraph Number	Description	Threshold	Objective	Performance
C40.7.10-1	a. Horizontal Cell Size	50 km	20 km	20 km
C40.7.10-2	b. Horizontal Reporting Interval	(TBD)	(TBD)	
C40.7.10-3	c. Horizontal Coverage	Oceans	Oceans	Oceans
C40.7.10-4	d. Measurement Range	Consistent with Sea Surface Wind (SSW)	Consistent with SSW	0-1.6 N/m^2 (Exceeds SSW threshold)
C40.7.10-5	f. Measurement Accuracy	Consistent with SSW	Consistent with SSW	0-0.03 N/m^2 (Exceeds SSW objective)
C40.7.10-6	g. Measurement Precision	Consistent with SSW	Consistent with SSW	0.02-0.14 N/m^2 (Exceeds SSW objective)
C40.7.10-7	h. Mapping Uncertainty	7 km	1 km (TBR)	
C40.7.10-8	i. Swath Width	1700 km (TBR)	3000 km (TBR)	>1700 km

ATBD for CMIS
Ocean EDR Algorithm Suite
Sea Surface Temperature EDR
Sea Surface Wind Speed/Direction EDR
Surface Wind Stress EDR

14-132

6.7.5. Stratification by other Geophysical Parameters

Our standard cross-talk plots are shown in Figure L. Not surprisingly, the plots show the same behavior as the 20 km wind speed for the SST, vapor, cloud and wind direction cross-talk. Since the 20 km wind speed meets the accuracy threshold but not objectives for columnar vapor less than 5 mm, the same is true of the wind stress EDR.
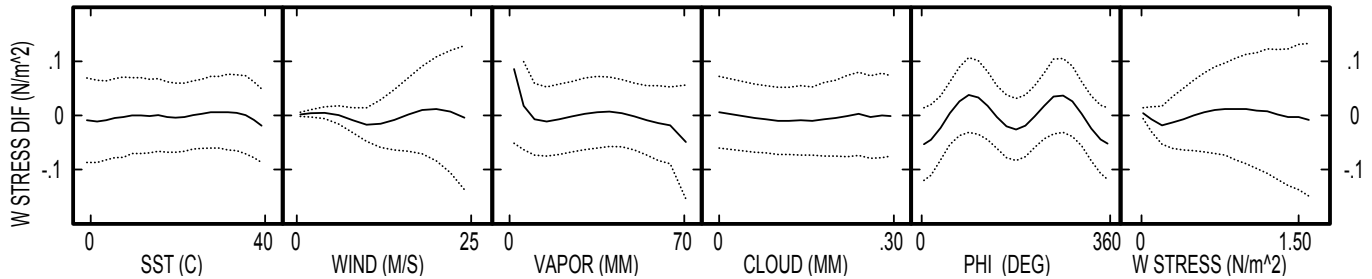
Figure 42: Wind Stress EDR Error Stratification

6.7.6. Stratification by Faraday Rotation

Since the 20 km wind speed accuracy and precision are not significantly affected by Faraday rotation up to 0.4 deg @ 10.7 GHz, neither is the wind stress. That is, the Wind Stress EDR will remain within the accuracy and precision objectives over the range of residual Faraday rotation that is expected for "gentle" magnetic storms.

6.7.7. Conditions Under which Performance may be Degraded

The conditions under which performance may be degraded are exactly the same as those for the 20 km wind speed in Section 6.3.

6.7.8. Exclusions

The exclusions under which we do not expect to meet the accuracy and precision thresholds are exactly the same as those for the 20 km wind speed in Section 6.3.

ATBD for CMIS
Ocean EDR Algorithm Suite
Sea Surface Temperature EDR
Sea Surface Wind Speed/Direction EDR
Surface Wind Stress EDR

14-133

7. Calibration and Validation

7.1. Calibration of the Radiative Transfer Model

The final, prelaunch ocean algorithm for CMIS will have benefited from several separate calibration and validation activities: SSM/I, TMI, AMSR and WindSat. The specification of the 6.625 GHz emissivity will need to be done when AMSR is flying. After specifying the 6.625 GHz emissivity, we expect that AMSR will be able to retrieve both the SST and the ocean surface wind speed very accurately.

Furthermore, AMSR will allow us to further pin down the size of the wind direction signal for V and H pol (section 3.7). Especially the ADEOS-2 AMSR will be helpful in this context, because there is a scatterometer (SeaWinds) attached on the same platform. This allows to measure simultaneously the brightness temperature T_B and atmospheric transmittance τ with the AMSR radiometer at all relevant frequencies and independently the wind vector with the SeaWinds scatterometer.

Even more important for the final calibration of the wind direction signal in the RTM will be the polarimetric radiometer WindSat, which also supposed to take measurements within the next couple of years. It will provide us with consistent data for all the 4 Stokes parameters. Moreover, the WindSat instrument will take simultaneous observations of one locations from different looking direction. This will allow to eliminate atmospheric effects, which constitute a large uncertainty in the determination of the wind direction effect (Wentz 1992; Meissner and Wentz 2000).

To summarize, we expect to have a well-calibrated pre-launch RTM available for all relevant CMIS channels that are used for our algorithm, including the polarimetric channels.

However, there are two caveats that need to be considered. First, it is not possible to absolutely calibrate satellite microwave radiometers to better than 1 to 2 K. In other words, there will probably be a constant T_B bias of 1 to 2 K between the various radiometers (CMIS, AMSTR, TMI, SSM/I). Fortunately, this bias is easily modeled in terms of either an additive or multiplicative offset for each channel. Thus the first caveat is that T_B offsets need to be derived after launch before accurate retrievals can be realized. The second caveat is that some fine-tuning of the model coefficients will probably be required in order to maximize the retrieval accuracy.

Given these caveats, we have developed a post-launch calibration/validation (cal/val) plan. The objective of the 3-month cal/val is to quickly implement the emissivity and T_B offsets so that reasonably accurate ocean products can be delivered to the scientific community soon after launch. Also, the quick-look calibration may identify other obvious problems in the algorithm that can be corrected. A more thorough 1-year investigation will then be conducted, a precision calibration will be done, and the algorithm will be updated.

The calibration and validation of the ocean products (T_S, W, φ_W and τ_0) will be based on intercomparisons with *in situ* observations from buoys, wind vector measurements from

scatterometers, results from General Circulation models (NCEP, ECMWF) and on T_S retrievals coming from IR satellite sensors. The details of the cal/val activity for each ocean parameter will now be discussed.

7.2. Cal/Val of the SST Algorithm

The CMIS T_S will be validated by comparisons with buoy measurements and IR SST products coming from the AVHRR series of instruments onboard the NOAA polar-orbiting satellite series. The IR SST products rely on several AVHRR channels, primarily channel 3 (3.6 to 3.9 μm), channel 4 (10.3-11.3 μm), and channel 5 (11.5 to 12.5 μm). The use of multiple channels allows for cloud detection in the retrieval process. Several algorithms to retrieve SST from AVHRR and other IR sensors have been developed, including the multi-channel (MC SST) (McClain, Pichel et al. 1985), and the non-linear (NL SST), used to produce the AVHRR Pathfinder dataset (Vazquez, Sumagaysay et al. 1999), as well as experimental algorithms that include measurements of columnar water vapor from SSM/I. These algorithms are used to generate some of the data products summarized in Table 25. A review of the various algorithms is given by (Barton 1995). The major drawback to the IR SST retrievals is interference due to spatial and temporal fluctuations in the atmosphere. Clouds, aerosols, and water vapor (Emery, Yu et al. 1994) all interfere with the measurement of SST, since emittance from these typically cooler layers reduce the inferred brightness temperature (but warm clouds over a boundary layer inversion can have the opposite effect). Thus in doing comparisons with CMIS, care will be taken to avoid cloudy areas.

Table 25: Some of the available SST products

SST Data Set	Acronym	Temporal Res.	Spatial Res.
Reynolds Optimum Interpolation SST	Reynolds SST	Weekly	100km
AVHRR Multi-Channel SST	MC SST	Weekly, Monthly	18 km
AVHRR Pathfinder v4.1 SST	PF SST	Daily, Monthly	9, 18, 54km
NESDIS SST Analyses	NESDIS SST	Daily	8 km
GOES SST	GOES SST	Hourly	4 km
TMI SST	TMI SST	Daily	50 km

The CMIS SST retrievals will also be validated by direct comparisons with ocean buoys. A rather extensive ocean buoy network is currently deployed in the Atlantic and Pacific Oceans. The Tropical Atmosphere Ocean (TAO) buoy array, concieved in the early 1980s and completed in 1994, consists of approximately 70 buoys located in the tropical Pacific between 8 deg N and 8 deg S. The new Pilot Research Moored Array in the Tropical Atlantic (PIRATA) is currently being implemented between 10 south and 15 north latitude. This array of 12 buoys is being opearted and managed by the Climate Variability (CLIVAR) group within the World Climate Research Program using multi-national cooperation. A third buoy dataset consists of a variety of buoy platforms and C-MAN stations located along US coastlines operated by the National Data Buoy Center (NDBC). In comparing the satellite and buoy measurements, two important effects need to be considered. First is the spatial-temporal mismatch between the buoy point observation and the satellite 50-km footprint. Second is the difference between the ocean skin temperature at 1 mm depth and the temperature at 1 m depth measured by the buoy. Both of these effects will

contribute to the observed difference between these two different types of observations. A list of the NDBC buoys is given in Table 26 and the location of the TAO array and the NDBC buoys are shown in Figure 43.

Table 26: NDBC Moored Buoy Open Water Locations as of July 1996

WMO Number	Latitude	East Longitude	General Location
41001	34.7	287.4	E. Hatteras
41002	32.3	284.8	S. Hatteras
41004	32.5	280.9	E. Charleston
41006	29.3	282.7	E. Daytona
41009	28.5	279.8	Canaveral
41010	28.9	281.5	E. Canaveral
41015	35.4	284.9	Cape Hatteras E
41016	24.6	283.5	Eleuthera
41018	15.0	285.0	Central Caribbean
41019	29.0	289.0	American Basin
42001	25.9	270.3	Mid Gulf of Mexico
42002	25.9	266.4	W. Gulf of Mexico
42003	25.9	274.1	E. Gulf of Mexico
42019	27.9	265.0	Lanelle
42020	27.0	263.5	Eileen
42035	29.2	265.6	Galveston
42036	28.5	275.5	S. Apalachicola
42037	24.5	278.6	Univ. of Miami
42039	28.8	274.0	NE Gulf of Mexico
42040	29.2	271.7	E. Miss River Delta
44004	38.5	289.3	Hotel
44005	42.9	291.1	Gulf of Maine
44006	36.3	284.5	Sandy Duck
44008	40.5	290.6	Nantucket
44009	38.5	285.3	Delaware Bay
44010	36.0	285.0	Sandy Duck
44011	41.1	293.4	Georges Bank
44014	36.6	285.2	Virginia Beach
44019	36.4	284.8	Sandy Duck
44025	40.3	286.8	Long Island
46001	56.3	211.8	Gulf of Alaska
46002	42.5	229.7	Oregon
46003	51.9	204.1	S. Aleutians
46005	46.1	229.0	Washington
46006	40.9	222.5	S.E. Papa
46025	33.7	240.9	Catalina Rdg
46028	35.8	238.1	C San Martin
46035	57.0	182.3	Bering Sea
46050	44.6	235.5	Stonewall Bank
46059	38.0	230.0	Boutelle Seamount
46061	60.2	213.2	Hinchinbrook
46147	51.8	228.8	S. Cape St. James
51001	23.4	197.7	N.W. Hawaii
51002	17.2	202.2	S.W. Hawaii
51003	19.1	199.2	W. Hawaii
51004	17.4	207.5	S.E. Hawaii
51026	21.4	203.1	N. Molokai
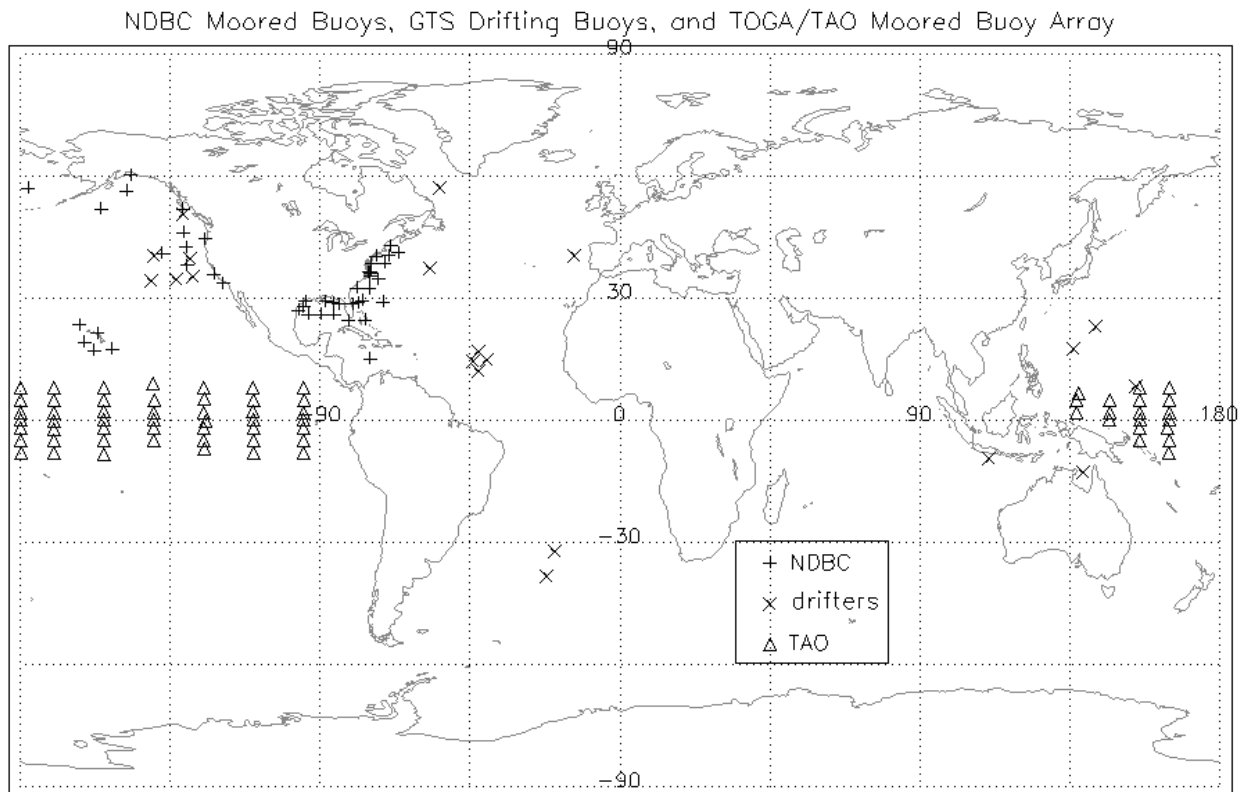
Figure 43: Locations of data buoys

7.3. Cal/Val of the Wind Vector Algorithm

One method of validation for the CMIS wind speed product is by intercomparisons with wind observations of moored buoys deployed in the open ocean discussed above. The NDBC buoys measure barometric pressure, wind direction, wind speed, wind gust, air and sea temperature, and wave energy spectra (i.e., significant wave height, dominant wave period, and average wave period). Wind speed and direction is measured during an 8 minute period prior to the hour of report. Exactly when the data is collected prior to report and the height of the anemometer depends on the type of payload on the moored buoy. These buoys are located primarily in the coastal and offshore waters of the continental United States, the Pacific Ocean around Hawaii, and from the Bering Sea to the South Pacific. In addition, there are about 50 coastal C-man stations that report hourly winds averaged over 2 minutes. The quality checked hourly buoy and C-man measurements are available by anonymous ftp from NOAA computers. Table 26 outlines the location of the NDBC moored buoys in service as of July 1996. These locations are mapped in Figure 43.

The 70 moored-buoy TOGA/TAO array covers the tropical Pacific ocean. These buoys are placed at approximately 10 to 15 deg longitude intervals and 2 deg to 3 deg latitude intervals. They measure air temperature, relative humidity, surface winds, T_S, and subsurface temperature to 500 meters. Wind vector measurements are made at a height of 4 m for 6 minutes centered on the hour and are vector averaged to derive the hourly value reported. To conserve battery power, hourly data is transmitted only 8 hours each day, 0600 to 1000 and 1200 to 1600 buoy local time.

ATBD for CMIS
Ocean EDR Algorithm Suite
Sea Surface Temperature EDR
Sea Surface Wind Speed/Direction EDR
Surface Wind Stress EDR

14-137

This document is intended for non-commercial use only. All other use is strictly forbidden without prior approval of the U.S. Government.

Three to four hours of T_S and wind data are available in near-real time from the GTS. These data are considered preliminary until the buoy is serviced and the stored hourly data is processed. This occurs approximately once each year. Figure 43 includes the TAO buoy network.

The anemometer heights z for the buoys and C-man stations vary. The NDBC moored buoys in general have z equaling 5 or 10 m, but some of the C-man stations have anemometers as high as 60 m. The PMEL anemometers are at 3.8 m above the sea surface. All buoy winds W_B will be normalized to an equivalent anemometer height of 10 m (1000 cm) assuming a logarithmic wind profile.

$$W_{B.10m} = \frac{\ln(1000cm/z_0)}{\ln(h/z_0)} \, W_{B,Z} \tag{7.1}$$

where z is the surface roughness length, which equals 1.52×10^{-2} cm assuming a drag coefficient of 1.3×10^{-3} (Peixoto and Oort 1992).

The buoy data sets will undergo quality check procedures, including checks for missing data, repeated data, blank fields, and out-of-bounds data. A time interpretive collocation program will calculate the wind speed at the time of the nearest satellite overpass, as is described in (Wentz 1997).

LIST OF ACRONYMS

AER	Atmospheric and Environmental Research, Inc., Lexington, MA
AMSR	Advanced Microwave Scanning Radiometer
ATBD	Algorithm Theoretical Basis Document
AVHRR	Advanced Very High Resolution Radiometer
BAPTA	Bearing and Power Transfer Assembly
BESEX	US-USSR Bering Sea Experiment
BPF	Band Pass Filter
CA	Calibration Amplification
CD	Coefficient of Drag
Cal/Val	Calibration and Validation of the Algorithm
CFOV	Composite Field of View
CLIVAR	Climate Variability
CMIS	Conical Microwave Imaging Scanner
EDR	Environmental Data Record
EFOV	Effective Field of View
EIA	Earth Incidence Angle
ERS	European Remote Sensing Satellite
ESMR	Electrically Scanned Microwave Radiometer
Fnn	SSM/I Satellites
GCM	General Circulation Model
GDAS	General Data Assimilation System
FNL	Final Analysis
IR	Infrared
JPL	Jet Propulsion Laboratory, Pasadena, CA.
LNA	Low Noise Amplifier
LR	Low Resolution
MC	Multi-Channel
MF	Median Filter
MLE	Maximum Likelihood Estimate
NASA	National Aeronautics and Space Administration
NDBC	National Data Buoy Center
NCAR	National Center of Atmospheric Research, Boulder, Co.
NCEP	National Centers for Environmental Prediction, Washington D.C.
NEDT	Noise Equivalent Delta TBs
NEMS	Nimbus-E Microwave Spectrometer
NIMBUS	NASA Satellite
NL	Non-Linear
NOAA	National Oceanic and Atmospheric Administration
NPOESS	National Polar-orbiting Operational Environmental Satellite System
NRF	Noise Reduction Factor
NSCAT	NASA Scatterometer
OMT	Ortho-mode Transducers
QUIKSCAT	NASA Scatterometer
PDF	Probability Density Function
PIRATE	Pilot Research Moored Array in the Tropical Atlantic
PPT	Parts per Thousand

ATBD for CMIS
Ocean EDR Algorithm Suite
Sea Surface Temperature EDR
Sea Surface Wind Speed/Direction EDR
Surface Wind Stress EDR

14-139

This document is intended for non-commercial use only. All other use is strictly forbidden without prior approval of the U.S. Government.

RDR	Raw Data Record
RF	Radio Frequency
RFI	Radio Frequency Interference
RMS	Root Mean Square
RSS	Remote Sensing Systems, Inc., Santa Rosa, CA
RTM	Radiative Transfer Model
SASS	SeaSat Scatterometer
SDR	Sensor Data Record
SEASAT	NASA Satellite
SMMR	Scanning Multichannel Microwave Radiometer
SOS	Sum of Squares
SRD	Sensor Requirements Document
SSM/I	Special Sensor Microwave Imager
SST	Sea Surface Temperature
SSW	Sea Surface Wind
TAO	Tropical Atmospheric Ocean
TB	Brightness Temperature
TBD	To be determined
TBR	To be reviewed
TDR	Temperature Data Record
TOGA	Tropical Ocean and Global Atmosphere
TMI	TRMM Microwave Imager
TRMM	Tropical Rainfall Measurement Mission
W	Ocean Surface Wind Speed (10m above surface)
WD	Wind Direction
WINDRAD	JPL polarimetric aircraft radiometer
WINDSAT	Polarimetric Radiometer
WOA	World Ocean Atlas

LIST OF FREQUENTLY USED SYMBOLS

Symbol	Definition	Units
$\vec{A}_{ij}^{k}$	ambiguity (wind vector) of rank k at grid point (i,j)	m/s
A_O	vertically integrated oxygen absorption	naper
A_V	vertically integrated water vapor absorption	naper
A_L	vertically integrated cloud liquid water absorption	naper
a_i, b_i, c_i, d_i	regression coefficients	varies
c	speed of light	cm/s
C	chlorinity of sea water	parts/thousand
C_D	coefficient of drag	none
E	sea-surface emissivity	none
E_p	emissivity of polarization state p=V,H,L,R,P,M,3,4	none
E	sea-surface emissivity (Stokes vector)	none
E_{ij}	median filter cost function at grid point (i,j)	m/s
f	fractional foam coverage	none
f	skill guidance weight function for median filter	none
F	foam+diffraction factor for sea-surface reflectivity	none
F	forward model function for brightness temperatures	Kelvin
h	Planck's constant in eq. (2)	erg-s
h	height above Earth surface, elsewhere	cm
h	window size for median filter	none
h_0	surface roughness length	cm
h_i, h_s	h-pol vectors for incident and scattered radiation	none
H	rain columnar height	km
I_λ	specific intensity	erg/s-cm^3-ster
j	$\sqrt{-1}$	none
k	Boltzmann's constant	erg/K
k_i	upward unit propagation vector	none
k_s	downward unit propagation vector	none
L	vertically integrated cloud liquid water	mm
m_1, m_2	coefficients for foam+diffraction factor	s/m
n	unit normal vector for tilted surface facet	none
P	column vector of geophysical parameters	varies
$P(S_u, S_c)$	probability density function of surface slope	none
P_λ	specific power	erg/s
p	unit polarization vector	none
r_0 to r_3	coefficients for geometric optics	see
R	rain rate	mm/h
R	total sea-surface reflectivity	none
R_p	reflectivity of polarization state p=V,H,L,R,P,M,3,4	none
R	total sea-surface reflectivity (Stokes vector)	none
R_0	specular reflectivity	none
R_{clear}	foam-free sea-surface reflectivity	none
R_{geo}	geometric optics sea-surface reflectivity	none
$R_\times$	reflectivity of secondary intersection	none

ATBD for CMIS
Ocean EDR Algorithm Suite
Sea Surface Temperature EDR
Sea Surface Wind Speed/Direction EDR
Surface Wind Stress EDR

14-141

s	path length in Section 3.2	cm
s	salinity, elsewhere	parts/thousand
s	scaling factor for wind speed	none
S	total path length through atmosphere	cm
S_c	crosswind slope for tilted surface facet	none
S_u	upwind slope for tilted surface facet	none
t_i	regression input for channel i	varies
t_S	sea-surface temperature	Celsius
T_B	brightness temperature	Kelvin
$\mathbf{T_B}$	brightness temperature (Stokes vector)	Kelvin
T_{BU}	upwelling atmospheric brightness temperature	Kelvin
T_{BD}	downwelling atmospheric brightness temperature	Kelvin
$T_{B\Omega}$	sky radiation scattered upward by Earth surface	Kelvin
$T_{B\uparrow}$	upwelling surface brightness temperature	Kelvin
$T_{B\downarrow}$	downwelling cold space brightness temperature	Kelvin
T_C	cold space brightness temperature	Kelvin
T_D	effective temperature for downwelling radiation	Kelvin
T_{eff}	effective temperature of surface+atmosphere	Kelvin
T_H	horizontally polarized brightness temperature	Kelvin
T_L	left circular polarized brightness temperature	Kelvin
T_M	- 45 deg polarized brightness temperature	Kelvin
T_P	+ 45 deg polarized brightness temperature	Kelvin
T_R	right circular polarized brightness temperature	Kelvin
T_S	sea-surface temperature	Kelvin
T_U	effective temperature for upwelling radiation	Kelvin
T_V	vertically polarized brightness temperature	Kelvin
T_3	3rd Stokes Parameter	Kelvin
T_4	4th Stokes Parameter	Kelvin
$\vec{U}_{ij}$	median filter wind vector at grid point (i,j)	m/s
$\mathbf{v_i, v_s}$	v-pol vectors for incident and scattered radiation	none
V	vertically integrated water vapor	mm
W	wind speed 10 m above sea surface	m/s
z_0	surface roughness length	m

Symbol	Definition	Units
α	total absorption coefficient	naper/cm
α_O	oxygen absorption coefficient	naper/cm
α_V	water vapor absorption coefficient	naper/cm
α_L	cloud liquid water absorption coefficient	naper/cm
β	diffraction factor for sea-surface reflectivity	none
γ	coefficients for wind direction variation of E	none
ΔE	wind direction signal of E	none
ΔR	wind direction signal of r	none
ΔT_B	wind direction signal of T_B	Kelvin
ΔS^2	total slope variance of sea surface	none
ε	T_B measurement error in Section 3	K
ε	complex dielectric constant of water, elsewhere	none

ϵ_∞	dielectric constant at infinite frequency	none
ϵ_S	static dielectric constant of sea water	none
ϵ_{S0}	static dielectric constant of distilled water	none
θ_i	incidence angle	degree
θ_n	nadir angle	degree
θ_s	zenith angle	degree
κ	reduction in sea-surface reflectivity due to foam	none
ϕ_i	azimuth angle for k_i	degree
ϕ_s	azimuth angle for k_s	degree
ϕ_W	wind direction (relative to N)	degree
ϕ_r	wind direction relative to azimuth look direction	degree
λ	radiation wavelength	cm
λ_R	relaxation wavelength of sea water	cm
λ_{R0}	relaxation wavelength of distilled water	cm
η	spread factor for relaxation wavelengths	none
Ω	fit parameter for sea surface scattering integral	none
Ω_p	Ω of polarization state p=V,H,L,R,P,M,3,4	none
ρ_h	h-pol Frensel reflection coefficient	none
ρ_v	v-pol Frensel reflection coefficient	none
ρ_{air}	air density	kg/m^3
ρ_L	liquid cloud water density	g/cm^3
ρ_V	water vapor density	g/cm^3
ρ_0	water density	g/cm^3
σ	ionic conductivity of sea water	s^{-1}
$\sigma_{o,c}$	co-pol. normalized radar cross section	none
$\sigma_{o,\times}$	cross-pol. normalized radar cross section	none
τ	atmospheric transmission	none
τ	ocean surface wind stress	kg m^{-1} s^{-2}
ν	radiation frequency	GHz
χ	shadowing function	none
χ^2	SOS function for MLE	none

REFERENCES

AER (2001). ATBD Vol. 1, Part 2: Footprint Matching and Interpolation. Lexington, Mass, AER, Inc.

Alishouse, J. C. (1983). "Total precipitable water and rainfall determinations from the SEASAT Scanning Multichannel Microwave Radiometer." J. Geophys. Res **88**: 1929-1935.

Alishouse, J. C., S. Synder, et al. (1990). "Determination of oceanic total precipitable water from the SSM/I." IEEE Trans. Geoscience and Remote Sensing **28**: 811-816.

ATBD for CMIS
Ocean EDR Algorithm Suite
Sea Surface Temperature EDR
Sea Surface Wind Speed/Direction EDR
Surface Wind Stress EDR

14-143

This document is intended for non-commercial use only. All other use is strictly forbidden without prior approval of the U.S. Government.

Archer, D. G. and P. Wang (1990). "The dielectric constant of water and Debye-Huckel limiting law slopes." J. Phys. Chem. Ref. Data **19**: 371.

Barrett, A. H. and V. K. Chung (1962). "A method for the determination of high-altitude water-vapor abundance from ground-based microwave observations." J. Geophys. Res **67**: 4259-4266.

Barton, I. J. (1995). "Satellite-derived sea surface temperatures: current status." J. Geophys. Res. **100**: 8777-8790.

Becker, G. E. and S. H. Autler (1946). "Water vapor absorption of electromagnetic radiation in the centimeter wave-length range." Phys. Rev., **70**(5/6): 303-307.

Chang, A. T. C. and T. T. Wilheit (1979). "Remote Sensing of atmospheric water vapor, liquid water and wind speed at the ocean surface by passive microwave techniques from the Nimbus-5 satellite." Radio Science **14**: 793-802.

Chang, H. D., P. H. Hwang, et al. (1984). "Monthly distributions of precipitable water from the NIMBUS 7 SMMR data." J. Geophys. Res. **86**: 5328-5334.

Chi, C.-Y. and F. K. Li (1988). "A comparative study of several wind estimation algorithms for spacebprne scatterometers." IEEE Trans. Geosc. Rem. Sens. **26**(2): 115 - 121.

Cole, K. S. and R. H. Cole (1941). "Dispersion and absorption in dielectrics." J. Chemical Physics **9**: 341-351.

Cox, C. S. (1958). "Measurements of Slopes of High Frequency Wind Waves." J. Mar. Res. **16**: 199-225.

Cox, C. S. and W. H. Munk (1954). "Measurement of the roughness of the sea surface from photographs of the sun's glitter." J. Opt. Soc. Am. **44**: 838-850.

Debye, P. (1929). Polar Molecule. New York.

Emery, W. J., Y. Yu, et al. (1994). "Correcting infrared satellite estimates of sea surface temperature for atmospheric water vapor attenuation." J. Geophys. Res. **99**: 5219-5236.

Gloersen, P., D. J. Cavalieri, et al. (1984). "Summary of results from the first NIMBUS 7 SMMR observations." J. Geophys. Res **89**: 5335-5344.

Goldstein, H. (1951). Attenuation by condensed water. Propagation of Short Radio Waves, MIT Rad. Lab. Ser. New York, McGraw-Hill. **13**.

Goodberlet, M. A., C. T. Swift, et al. (1989). "Remote sensing of ocean surface winds with the SSM/I." J. Geophys. Res **94**: 14547-14555.

Grant, E., T. Buchanan, et al. (1957). "Dielectric behavior of water at microwave frequencies." J. Chem. Phys **26**: 156-161.

ATBD for CMIS
Ocean EDR Algorithm Suite
Sea Surface Temperature EDR
Sea Surface Wind Speed/Direction EDR
Surface Wind Stress EDR

14-144

This document is intended for non-commercial use only. All other use is strictly forbidden without prior approval of the U.S. Government.

Grody, N. C. (1976). "Remote sensing of atmospheric water content from satellites using microwave radiometry." IEEE Trans. Antennas Propagat. **AP-24**: 155-162.

Hasted, J. B. and G. Roderick (1958). "Dielectric properties of aqueous and alcoholic electrolytic solutions." J. Chem. Phys. **29**: 17-26.

Hasted, J. B. and S. E. Sabeh (1953). "The dielectric properties of water in solutions." Trans. Faraday Soc. **49**: 1003-1011.

Ho, W. and W. F. Hall (1973). "Measurements of the dielectric properties of sea water and NaCl solutions at 2.65 GHz,." J. Geophys. Res. **78**: 6301-6315.

Ho, W. W., A. W. Love, et al. (1974). Measurements of the dielectric properties of sea water at 1.43 GHz.

Hollinger, J. P. (1971). "Passive microwave measurements of sea surface roughness." IEEE Trans. Geosci. Electron. **GE-9**: 165-169.

IPO (2000). CMIS Sensor Requirements Document. Silver Spring MD, NPOESS Integrated Program Office.

Jackson, J. D. (1975). Classical Electrodynamics. New York, Wiley.

Jones, W. L., P. G. Black, et al. (1979). "Seasat scatterometer: Results of the Gulf of Alaska workshop." Science **204**: 1413-1415.

Kalnay, E., M. Kanamitsu, et al. (1996). "The NCEP/NCAR 40-Year Reanalysis Project." Bulletin of the American Meteorological Society **77**(3): 437-471.

Keller, W. C. and J. W. Wright (1975). "Microwave scattering and the straining of wind-generated waves." Radio Sci **10**: 139-147.

Klein, L. A. and C. T. Swift (1977). "An improved model for the dielectric constant of sea water at microwave frequencies." IEEE J. Oceanic Eng. **OE-2**: 104-111.

Lane, J. A. and J. A. Saxton (1952). "Dielectric dispersion in pure polar liquids at very high frequencies, III:
The effect of electrolytes in solution." Proc. Roy. Soc **A213**: 531-545.

Lide, D. R. (1993). Handbook of Chemistry and Physics. Ann Arbor, CRC Press.

Liebe, H. J. (1985). "An updated model for millimeter wave propagation in moist air." Radio Sci. **20**: 1069-1089.

Liu, W. and W. Tang (1996). Equivalent Neutral Wind. Pasadena, JPL.

ATBD for CMIS
Ocean EDR Algorithm Suite
Sea Surface Temperature EDR
Sea Surface Wind Speed/Direction EDR
Surface Wind Stress EDR

14-145

This document is intended for non-commercial use only. All other use is strictly forbidden without prior approval of the U.S. Government.

Malmberg, C. and A. Maryott (1956). "Dielectric constant of water from 0° to 100°C." J. Res. Nat. Bureau of Standards **56**: 1-8.

McClain, E. P., W. G. Pichel, et al. (1985). "Theory and validation of the multiple window sea surface temperature technique." J. Geophys. Res **90**: 11587-11601.

Meissner, T., D. Smith, et al. (2001). "A 10-Year Intercomparison betwen Collocated SSM/I Oceanic Surface Wind Speed Retrievals and Global Analysis." J. Geophys. Res. **In Press**.

Meissner, T. and F. Wentz (2000). An updated analysis of the wind direction signal in passive polarimetric brightness temperatures and its effect on wind vector retrieva. Santa Rosa, Remote Sensing Systems.

Milman, A. S. and T. T. Wilheit (1985). "Sea surface temperatures form the Scanning Multichannel Microwave Radiometer on Nimbus_7." . Geophys Res **90**: 11587-11601.

Mitsuyasu, H. and T. Honda (1982). "Wind-induced growth of water waves." J. Fluid Mech. **123**: 425-442.

Monahan, E. C. and I. O'Muircheartaigh (1980). "Optimal power-law description of oceanic whitecap coverage dependence on wind speed." J. Phys. Oceanogr. **10**: 2094-2099.

Naderi, F. M., M. H. Freilich, et al. (1991). Spaceborn Radar Measurement of Wind Velocity Over the Ocean - An Overview of the NSCAT Scatterometer System. IEEE.

Njoku, E. G. and L. Swanson (1983). "Global measurements of sea surface temperature, wind speed." Monthly Weather Review **111**: 1977-1987.

Nordberg, W., J. Conaway, et al. (1971). "Measurement of microwave emission from a foam covered wind driven sea." J. Atmos. Sci. **38**: 429-433.

Peake, W. H. (1959). "Interaction of electromagnetic waves with some natural surfaces." IEEE Trans. Antennas Propagat. **AP-7**: S324-S329.

Peixoto, J. P. and A. H. Oort (1992). Physics of Climate. New York, American Institute of Physics.

Poe, G. and K. St. Germain (1998). Polarimetric Emission Model of the Sea at Microwave Frequencies, Part I: Theory. Washington, D.C., Naval Research Laboratory.

Press, W. H., S. A. Teukolsky, et al. (1992). Numerical Recipes in Fortran 77. Cambridge, Cambridge University Press.

Reif, F. (1965). Fundamentals of Statistical and Thermal Physics. San Francisco, McGraw-Hill, Inc.

Rice, S. O. (1951). "Reflection of electromagnetic waves from slightly rough surfaces." Commun. Pure Appl. Math **4**: 351-378.

ATBD for CMIS
Ocean EDR Algorithm Suite
Sea Surface Temperature EDR
Sea Surface Wind Speed/Direction EDR
Surface Wind Stress EDR

14-146

This document is intended for non-commercial use only. All other use is strictly forbidden without prior approval of the U.S. Government.

Rosenkranz, P. W. (1975). "Shape of the 5 mm oxygen band in the atmosphere." <u>IEEE Tran. Antennas Propag</u> **AP-23**(4): 498-506.

Schluessel, P. and H. Luthardt (1991). "surface wind speeds over the North Sea from Special Sensor Microwave/Imager observations." <u>J. Geophys. Res.</u> **96**: 4845-4853.

Schultz, H. (1990). "A Circular Median Filter Approach for Resolving Directional Ambiguities in Wind Fields Retrieved From Spaceborne Scatterometer Data." <u>Journal of Geophysical Research</u> **95**(C4): 5291-5303.

Shaffer, S., S. Dunbar, et al. (1991). "A Median Filter Based Ambiguity Removal Algorithm For NSCAT." <u>IEEE TRansactions on Geoscience and Remote Sensing</u> **29**(1): 167 -1 74.

Smith, P. M. (1988). "The emissivity of sea foam at 19 and 37 GHz." <u>IEEE Trans. Geosci. Remote Sensing</u> **GE-26**: 541-547.

Smith, S. D. (1988). "Coefficients for Sea Surface Wind Stress, Heat-Flux, and Wind Profiles as a Function of Wind Speed and Temperature." <u>J, Geophys. Res.</u> **93**: 15,467-15472.

St. Germain, K. and G. Poe (1998). <u>Modeling of Polarimetric Microwave Signal due to Ocean Surface Wind Vector</u>. International Geoscience and Remote Sensing Symposium, Seattle.

St. Germain, K. and G. Poe (1998). Polarimetric Emission Model of the Sea at Microwave Frequencies, Part II: Comparison with Measurements. Washington, D.C., Naval Research Laboratory.

St. Germain, K. and G. Poe (1999). <u>Modeling of Polarimetric Microwave Signal due to Ocean Surface Wind Vector</u>. 6th Specialist Meeting on Microwave Radiometry and Remote Sensing of the Environment, Florence, Italy.

Staelin, D. H. (1966). "Measurements and interpretation of the microwave spectrum of the terrestrial atmosphere near 1-cm wavelengths." <u>J. Geophys Res.</u> **71**: 2875-2881.

Staelin, D. H., K. F. Kunzi, et al. (1976). "Remote sensing of atmospheric water vapor and liquid water with the Nimbus-5 microwave spectrometer." <u>J. Appl. Meteor.</u> **15**: 1204-1214.

Stoffelen, A. (1998). Scatterometry, Utrecht, NL.

Stoffelen, A. and D. Anderson (1995). The ECMWF contribution to the characterization, interpretation, calibration and validation of ERS-1 scatterometer backscatter measurements and their use in numerical weather prediction models. Reading, England, ECMWF.

Stoffelen, A. and D. Anderson (1997). "Ambiguity Removal and Assimilation of Scatterometer Data." <u>Q.J.R.Meteorol.Soc.</u> **123**: 491 - 518.

Stogryn, A. (1967). "The apparent temperature of the sea at microwave frequencies." <u>IEEE Trans. Antennas Propagat.</u> **AP-15**: 278-2.

ATBD for CMIS
Ocean EDR Algorithm Suite
Sea Surface Temperature EDR
Sea Surface Wind Speed/Direction EDR
Surface Wind Stress EDR

14-147

This document is intended for non-commercial use only. All other use is strictly forbidden without prior approval of the U.S. Government.

Stogryn, A. (1971). "Equations for calculating the dielectric constant of saline water." IEEE Trans. Microwave Theory Tech. **MTT-19**: 733-736.

Stogryn, A. (1972). "The emissivity of sea foam at microwave frequencies." J. Geophys. Res. **77**: 1650-1666.

Vazquez, J., R. M. Sumagaysay, et al. (1999). NOAA/NASA AVHRR Oceans Pathfinder, Sea Surface Temperature Data Set. Pasadena, CA, Jet Propulsion Laboratory.

Waters, J. R. (1976). Absorption and emission by atmospheric gases. Methods of Experimental Physics. M. L. Meeks. Orlando, Florida. **12B:** Chapter 2,3.

Wentz, F. (1975). "A two-scale scattering model for foam-free sea microwave brightness temperatures." Journal of Geophysical Research **80**: 3441-3446.

Wentz, F. (1983). "A model function for ocean microwave brightness temperatures." Journal of Geophysical Research **88**(C3): 1892-1908.

Wentz, F. (1990). SBIR phase II report: West coast storm forecasting with SSM/I. Santa Rosa, CA, Remote Sensing System.

Wentz, F. (1991). User's Manual: SSM/I Antenna Temparature Tapes (Revision 1). Santa Rosa, CA, Remote Sensing Systems.

Wentz, F. (1992). "Measurement of Oceanic Wind Vector Using Satellite Microwave Radiometers." IEEE Transactions on Geoscience and Remote Sensing **30**(5): 960 - 972.

Wentz, F. (1997). Specifying the NSCAT MLE Expected Variance Using the After-the-Fit Sigma0 Residual. Santa Rosa, Remote Sensing Systems.

Wentz, F., C. Gentemann, et al. (2000). "Satellite measurements of sea surface temperature through clouds." Science **288**(5467): 847-850.

Wentz, F., A. Mattox, et al. (1986). "New algorithms for microwave measurements of ocean winds: Applications to SeaSat and the Special Sensor Microwave Imager." Journal of Geophysical Research **91**: 2289-2307.

Wentz, F. and T. Meissner (1999). AMSR Ocean Algorithm (Version 2). Santa Rosa, CA, Remote Sensing Systems.

Wentz, F. and R. Spencer (1998). "SSM/I rain retrievals within a unified all-weather ocean algorithm." Journal of the Atmospheric Sciences **55**(9): 1613-1627.

Wentz, F. J. (1997). "A Well Calibrated Ocean Algorithm for Special Sensor Microwave/Imager." Journal of Geophysical Research **102**(C4): 8703-8718.

ATBD for CMIS
Ocean EDR Algorithm Suite
Sea Surface Temperature EDR
Sea Surface Wind Speed/Direction EDR
Surface Wind Stress EDR

14-148

This document is intended for non-commercial use only. All other use is strictly forbidden without prior approval of the U.S. Government.

Weyl, P. K. (1964). "On the change in electrical conductance of sea water with temperature." Limnol. Oceanogr., **9**: 75-78.

Wilheit, T. T. (1979). "The effect of wind on the microwave emission from the ocean's surface at 37 GHz." J. Geophys. Res. **84**: 4921-4926.

Wilheit, T. T. (1979). "A model for the microwave emissivity of the ocean's surface as a function of wind speed." IEEE Trans. Gesoci. Electronics **GE-17**: 244-249.

Wilheit, T. T. and A. T. C. Chang (1980). "An algorithm for retrieval of ocean surface and atmospheric parameters from the observations of the Scanning Multichannel Microwave Radiometer (SMMR)." Radio Sci. **15**: 525-544.

Wilheit, T. T. and M. G. Fowler (1977). "Microwave radiometric determination of wind speed at the surface of the ocean during BESEX." IEEE Trans. Antennas Propagat. **AP-25**: 111-120.

Wilson, W. and S. Yueh (1996). Ocean Wind Direction Measurements Using Passive Polarimetric Radiometers. Pasadena, JPL.

Wu, S. T. and A. K. Fung (1972). "A non-coherent model for microwave emission and backscattering from the sea surface." J. Geophys. Res. **77**: 5917-5929.

Yueh, S. and W. Wilson (1999). Validation of Wind Radiometer Technique Using Aircraft Radiometer and Radar Measurements for High Ocean Winds. Pasadena, JPL.

Yueh, S., W. Wilson, et al. (1999). "Polarimetric Microwave Brightness Signatures of Ocean Wind Directions." IEEE Transactions on Geoscience and Remote Sensing **37**(2): 949 - 959.

Yueh, S. H. (1997). "Modeling of wind direction signals in polarimetric sea surface brightness temperatures." IEEE Transactions on Geoscience and Remote Sensing **35**(6): 1400-1418.

Yueh, S. K., S. V. Nghiem, et al. (1994). "Polarimetric thermal emission from periodic water surfaces." Radio Sci. **29**(1): 87-96.

ATBD for CMIS
Ocean EDR Algorithm Suite
Sea Surface Temperature EDR
Sea Surface Wind Speed/Direction EDR
Surface Wind Stress EDR

14-149

This document is intended for non-commercial use only. All other use is strictly forbidden without prior approval of the U.S. Government.